UNIVERSITY OF SASSARI

PH.D. SCHOOL IN NATURAL SCIENCE

A Dissertation for the Degree of Doctor of Philosophy in Science and technology of mineral and rocks of industrial interest presented at Sassari University in 2011

XXIV cycle

Radiometric methods in geological reconstruction, in the prospecting of georesources and evaluation of hazard

DIRECTOR:
Prof. Marco Apollonio

TUTOR:
Prof. Giacomo Oggiano

PH.D. STUDENT:
Dr. Puccini Antonio

INDEX

Appendix

Introduction

Radiations are a natural part of the earth's environment. They are found naturally in air, water, soil and rock, as well as in organic matter. Natural radioactivity on Earth is caused by: 1) radiation from outer space (actually, its interaction with atmosphere); 2) presence of several radioactive nuclides in lithosphere. Natural source of radiation derive from radio-isotope synthesized during the creation of the solar system. Because of their long half-lives, they still exist today. Among these, potassium (^{40}K), uranium (^{238}U and ^{235}U and their daughters), and thorium (^{232}Th and their daughters) are the only radio-isotopes that produce high-energy gamma rays of sufficient intensity to be used for gamma ray spectrometry.

Gamma ray spectrometry is an excellent tool in evaluating the environmental radioactivity.

The present research project started with the development of a portable detector consisting of 1 liter NaI(Tl) crystal for in-situ measurements of rocks or soil.

The main advantages of this instruments compared to laboratory spectrometers are: limited costs, and possibility of getting results in real-time.

The instrument was developed, according to our purposes, and calibrated at the National Lab of Legnaro (PD) in accordance with international guidelines of the IAEA and of the ANSI.

The potentiality of the portable detector, was tested by comparing in-situ measures with analysis performed in laboratory, with both high-resolution gamma-ray spectrometer (HPGe detector) and ICP-MS.

After the development of the analytical methodology we carried out our research project focusing the content of natural radioactivity in granite lithotypes used as building materials. The knowledge of natural radioactivity in building materials (^{40}K, ^{232}Th and ^{238}U with its decay series) is important to determining the amount of exposure for people who spend much of their time indoor (Stoulos *et al.*, 2003). Radiation exposure due to building material can be divided into external and internal exposure. The external exposure is caused by direct gamma radiation. According to the radiological protection of the European Commission (RP No. 112, 1999), an inhabitant living in an apartment block made of concrete with average activity concentrations (40 Bq kg^{-1}, 30 Bq kg^{-1} and 400 Bq kg^{-1} for radium, thorium and potassium, respectively) receives an annual effective dose of about 0,25 mSv. Instead radon inhalation is responsible for the internal exposure, caused by deposition of its decay products in the respiratory tract. Many governmental and international organizations (e.g. UNSCEAR, European Commission), recently, payed particular attention trying to minimizing the health risks associated with the exposure to these indoor radiation. All type of building material contain various amounts of natural radioactive nuclides. Scott & Dickson (1990) analyzed a large number and wide variety of rocks by laboratory gamma-ray spectrometry, concluded that the radionuclides concentration show an increase with an increase of SiO_2. So acid rocks such as granites could contain large amount of radionuclides. This conclusion has been one of the reasons that led us to analyze some granitic rocks present in Sardinia. Where different granite lithotypes are quarried and commercialized overseas. During the last few years, granites was very popular and its global production was comparable to that of marble (Tsirambides, 1996). For the risk assessment the Activity Concentration Index (I) was taken into account, according to the European Commission (RP No. 112, 1999). The (I) shall not exceed the limits fixed by the EC, which depend on the dose criterion (doses must not exceed 1 mSv y^{-1}) and the amount and the way materials are employed (tiles, boards, concrete, masonries, e.g.).

The excellent response that the portable spectrometer gave on granitoid lithotypes encouraged us to develop the second part of our project which deals with:

- Employment, in an innovative way, a portable gamma ray spectrometer as a useful tool for mapping various intrusive complexes and resolve some problems that may arise in the field survey of the different plutons;
- Estimate the heat derived from radioactive decay of K, eU and eTh in rocks that formed the Variscan crust with the goal of assess the thermal budget of the Variscan crust (at 350 and 300 Ma).

The Sardinia-Corsica Batholith (S-CB) is the most largest batholiths of Variscan Age. It was emplaced during Carboniferous and Permian times (340-280 Ma, Paquette *et al.*, 2003). In Sardinia, the S-CB have a calc-alkaline affinity and it is related with the Variscan syn- to late collision stages of the South Variscan belt (Paquette *et al.*, 2003). The granitoid rocks, in Sardinia, covers about 6000 km^2 (Ghezzo & Orsini, 1982); this suggests to us how the cartography of these rocks are very important for understanding the structure of the Variscan crust. Unfortunately, due to its large size the S-CB in Sardinia, is still poorly known and no detailed maps of discriminate the different intrusion exists. The only 1:100000 map imposed a purely petrographic approach. So different intrusions with different age and accessory mineral content are not discriminated.

To discriminate among different intrusions, generated from different magmatic pulse within a composite batoliths, is not a easy task, particularly if different intrusion with similar petrofacies come in contact. Moreover, the exposure of contacts between different plutons is not frequent. However, if textural and modal features converge, the only effective way able to discriminate such intrusions are some laboratory analysis (Radiometric Dating, Chemical Analysis e.g), the cost of which, is not sustainable when the aim of the survey is the production of a geological or thematic (dimension stone) map. So testing the portable spectrometer as a smart tool for a “real time” geochemical discrimination of single intrusion was a worthy task. The S-CB is an ideal testing area, consisting of several coalescent intrusions which often are very similar from textural and compositional point of view. After, focuse our tests on the Buddusò pluton and its neighbour intrusions for the following reason:

- Relatively small intrusion (about 70 km^2);
- A pluton previously studied (Bruneton & Orsini, 1977; Orsini & Fernandez, 1987; Barbey *et al.*, 2008);

This intrusive complex is surrounded by the Concas, Sos Canales, Benetutti, Monte Lerno, and Alà dei Sardi-Tepilora plutons which vary from tonalitic-granodiorites to leucomonzogranites, which were in turn compared with the Buddusò pluton. Given the excellent results obtained in the Buddusò pluton area, we have expanded our horizons by taking into account to apply the methodology to other intrusive complexes that were much less studied (Arzachena pluton and its adjacent intrusion).

The thermal structure of the continental crust is, undoubtedly, the main parameters that controls all geological processes occurring inside the crust as metamorphism, magmatism and defomation.

Three main sources would have contributed to the thermal budget:

- Radiogenic heat production;
- Moho heat flow;
- Viscous shear heating (poorly developed in literature).

The heat production in the crust is the result for 98% of the decay series ^{238}U and ^{232}Th and the single-step decay ^{40}K (Slagstad, 2008). These elements are concentrated in large quantities in the crust (especially in the upper and middle crust) and therefore contribute significantly to the thermal budget (Jaupart & Mareschal, 2004); various studies lead to a range of 0,7-1,3 μW m^{-3} for the average rate of crustal heat production (Wedepohl, 1991; Rudnick & Fountain, 1995; Taylor & McLennan, 1995). Another important parameter for characterize the thermal structure of the crust is quantify the heat conducted though the crust from the underlying mantle, for example in Corsica Verdoya *et al.* (1998) took a value equal to 30 mW m^{-2}. Another form of internal heat production is viscous shear heating; several studies have quantitatively demonstrate that shear heating can produce, at orogen-scale, a surplus of heat of 0,1 μW m^{-3} to < 1 μW m^{-3} (Burg & Gerya, 2005). The thermal structure of two model crust constraints at 350 Ma and 300 Ma was calculated by changing Moho heat flow and Viscous shear heating, within the range of geologically reasonable values. From the references has been collected a large number of thermo-barometric constraints, at 350 Ma and 300 Ma, to verify if the geotherm built with our data fitted with the P-T-t path. Then, the aim of this part was to evaluate the thermal budget of the Variscan crust by comparing one-dimensional numerical model (Casini, 2011 *in press*) with a literature database on PT conditions recorded at ca. 350 Ma and ca. 300 Ma. In the latter part of this work we have assessed the geodynamic implications arising from our geotherm.

Section 1: Principles of radioactivity

1.1 Radioactive decay

The rate at which a particular radioactive material disintegrates, with some exceptions, is independent on physical and chemical conditions. In general, we can not predict which atoms will disintegrate at a particular time. Instead, we can predict the average number of atoms that will disintegrates in a certain time interval. The radioactive decay law is (Fig. 1.1):

$$N(t) = N_0 e^{-\lambda t}$$

Where N_0 represents the number of atoms at initial time $t = 0$, $N(t)$ is the number remaining at time t and λ is the decay constant.

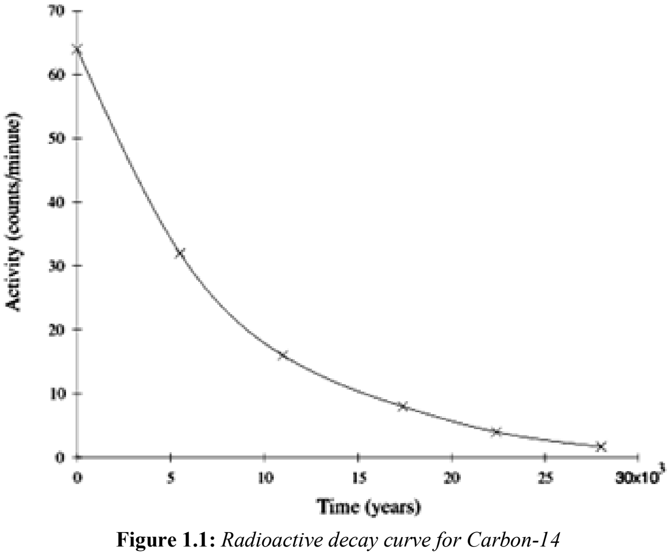

Figure 1.1: *Radioactive decay curve for Carbon-14*

Activity is proportional to the number of decays per unit time (its unit is Becquerel that is equal to one decay per second), as shown in the following expression:

$$A(t) = -dN(t)/dt = \lambda N(t) = \lambda N_0 e^{-\lambda t}$$

The Specific activity is equal to activity per unit mass and is expressed in Bq/Kg.

It's very important to point out that the number of decays in a certain time interval t, is proportional to the initial number of atoms; hence, the number of daughter atoms is linked via a linear relationship to the number of parent atoms at time t_0 (Fig. 1.2).

The decay constant λ is related to mean lifetime (τ) and half-life ($T_{1/2}$) of a radioisotope.

The mean lifetime is defined as:

$$\tau = 1/\lambda$$

The half-life is expresses as:

$$T_{1/2} = \ln 2/\lambda = 0.693\tau$$

At the end of one half–life period of time, one half of the original material remains in the sample; at the end of two half-lives, one quarter of the original material will still exist, and so on.

The time trend of the number of parent atoms of a radioactive sample is an exponential decreasing, while the number of daughter atoms is exponentially increase (Fig. 1.2).

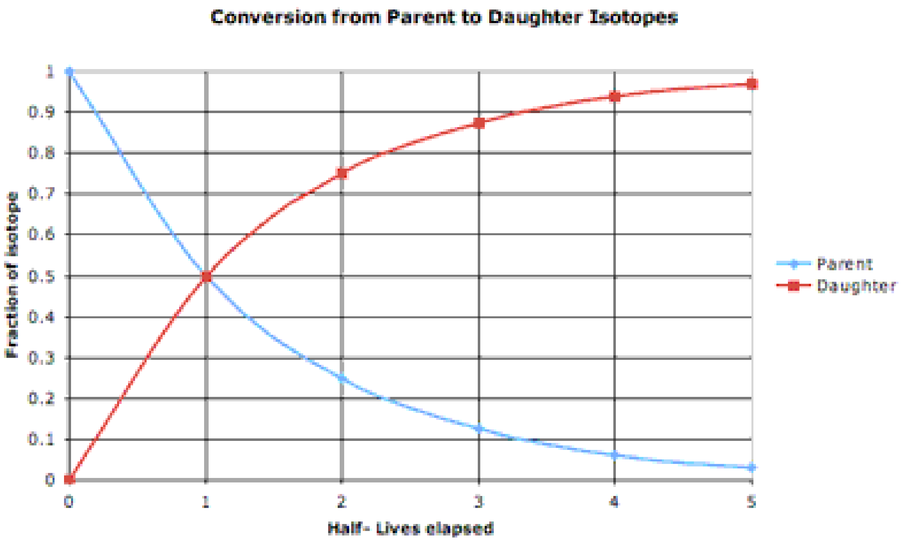

Figure 1.2: *Parent atoms and daughter atoms time trend*

Some radionuclides may have more than one channel of decay and decay of each branch is associated with a well-defined probability, so-called branching ratio. It is the ratio of the number of particles that decay in a certain way to the total number of particles of the radioactive sample. The branching ratio is crucial in the reconstruction of the overall energy spectrum, since each transition release a certain amount of energy character to specific channel. All decays are characterized by a decay costant (λ) related to the probability that this process occurs in a period of time. In the case of chain decay process the whole system has a decay probability linked to the constant λ_t equal to the sum of the different decay constant, that is:

$$\lambda_t = \lambda_1 + \lambda_2 + \lambda_3 + \ldots\ldots + \lambda_n$$

In a closed system, starting with a specified amount of a parent element, the number of atoms of daughter elements and their activity grows gradually, until is reaches the secular equilibrium. At that time, the activities of each chain elements are identical. Thus the concentration measurements of any daughter element can be used to estimate the concentration of any other element in the decay series (Fig 1.3). Under equilibrium conditions, this relationship can be expressed as follows:

$$\lambda_1 N_1 = \lambda_2 N_2 = \ldots\ldots\ldots = \lambda_n N_n$$

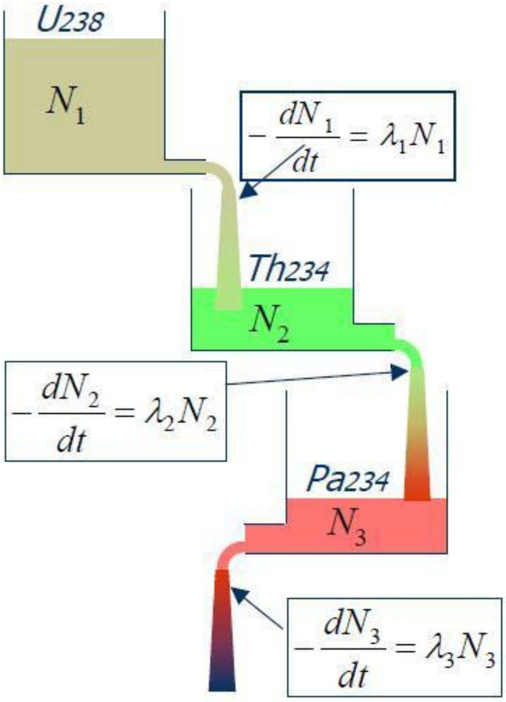

Figure 1.3: *Secular equilibrium representation. In the case of secular equilibrium incoming and outgoing flow into the vessel of the* ^{234}*Th are equal, which means that the incoming and outgoing flow of each element will be equals for each component chain*

1.2 Environmental radioactivity

This section briefly describes the radioactivity sources that can be found on Earth. Environmental radioactivity can be either natural or man-made.

1.2.1 Natural radioactivity

The natural radioactivity is divided into two categories:

- cosmogenic radionuclides that are continuosly produced in the upper atmosphere by the action of the cosmic rays.
- primordial radionuclides that have been present since origin of the Earth.

1.2.1.1 Cosmogenic radionuclides

Cosmic rays originate outside of the Earth's atmosphere. They produce a range of radionuclides in the atmosphere, biosphere and lithosphere by various nuclear reactions; these radionuclides are called the cosmogenic radionuclides. The four most important cosmogenic radionuclides for human exposure are tritium, ^{7}Be, ^{14}C and ^{22}Na, although a much wider range is produced. The most significant of these radionuclides is ^{14}C. The constant generation of ^{14}C by cosmic rays is used in radiocarbon dating.

1.2.1.2 Primordial radionuclides

Primordial radionuclides are producing in decay chains of three nuclear isotopes (^{238}U, ^{235}U and ^{232}Th), also there is a number of radioisotopes that decay directly into a stable isotope. Among these, the most abundant in nature are ^{40}K, ^{238}U and ^{232}Th.

There are three potassium isotopes, which were found in nature: ^{39}K (93,3%), ^{40}K (0,012%) and ^{41}K (6,7%). ^{40}K is the only isotope that emits gamma rays (Fig. 1.4). The ratio between the total abundance of potassium and abundance of ^{40}K is known. The gamma ray detection of ^{40}K can be used to estimate the total amount of potassium.

The half-life of ^{40}K is $1{,}3 \times 10^{9}$ years.

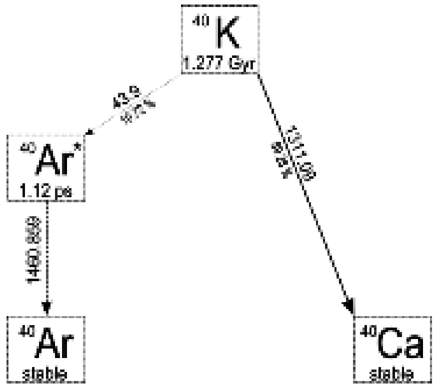

Figure 1.4: Decay scheme of ^{40}K. The decay of ^{40}K can happen in two ways: 1) a β decay to ^{40}Ca, with branching ratio 89,.28%; 2) an electron capture to excited state of ^{40}Ar, which have very short half-life (1,12 ps), and then decay to the ground state with emission of a gamma ray with energy equal to 1460,859 keV.

Uranium occurs naturally in three different isotopes with mass numbers equal to 234, 235 and 238. The most abundant isotope is the ^{238}U, it represents the 99,28% of the natural uranium. ^{238}U, unlike the ^{40}K, do not achieve stability with a single decay, but is characterized by a decay chain through which it reaches the stable isotope ^{208}Pb (Fig. 1.5). Not all nuclides from the decay chain produce gamma rays, and, those which were used for detection have energy equal to 610 keV, 1120 keV, 1740 keV originated from the transition of ^{214}Bi. The half-life of ^{238}U is 4,47 × 10^9 years.

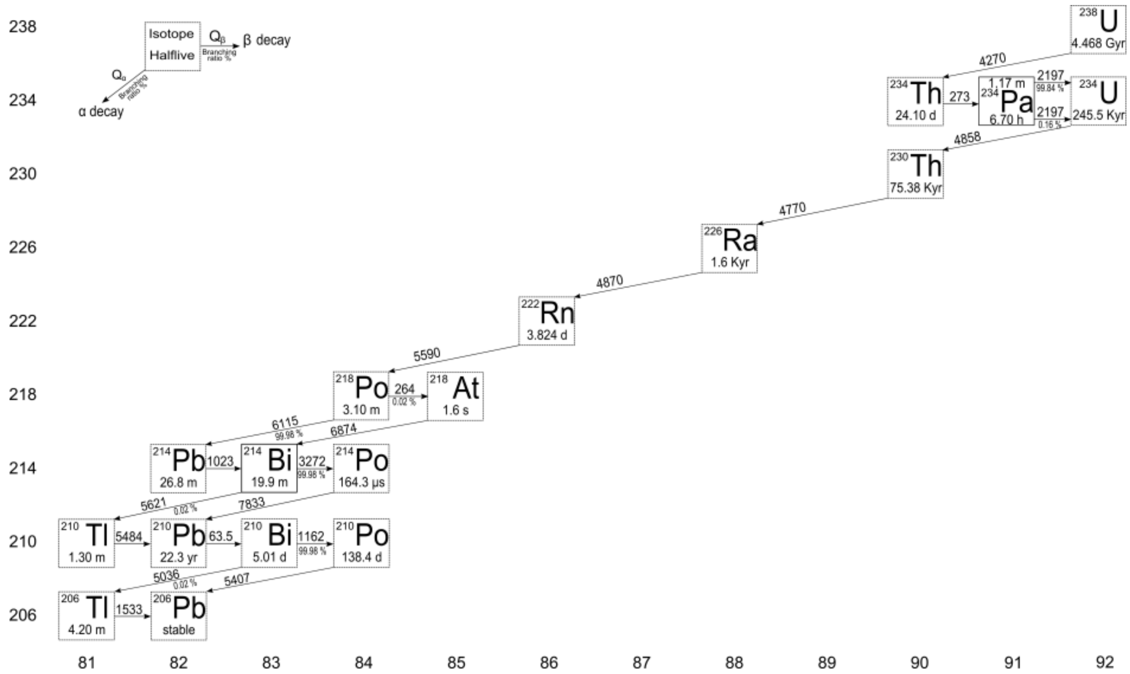

Figure 1.5: *Decay chain of ^{238}U*

Natural thorium consists of only one isotope ^{232}Th, which has a half-life 1,39 × 10^{10} years. ^{232}Th, like ^{238}U, has a decay chain. The gamma emission which were used for detection are those of the ^{208}Tl with energy equal to 580 keV and 2614 keV. The final stable isotope of this decay chain is ^{208}Pb (Fig. 1.6).

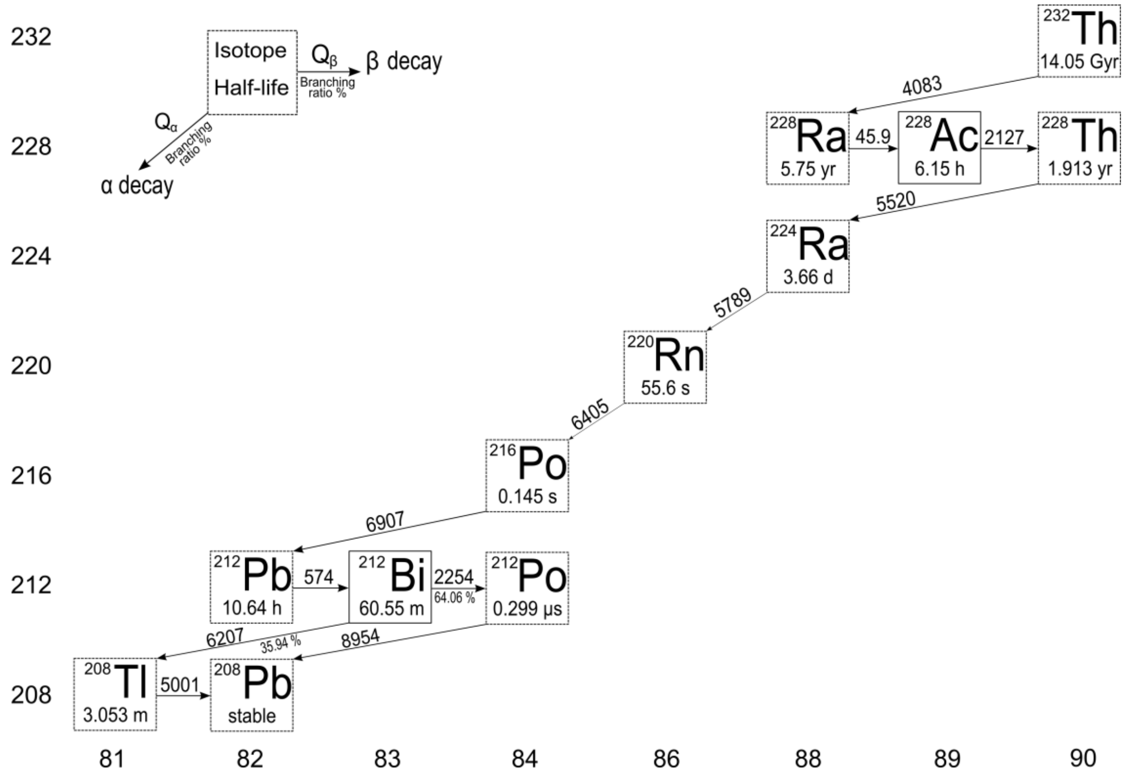

Figure 1.6: *Decay chain of ^{232}Th*

Generally, all isotopes in uranium and thorium decay chains have mean lifetime shorter than their parents, and the secular equilibrium can be reached if the system is isolated (Fig. 1.3). Disequilibrium occurs when one or more decay products are completely or partially removed or added to the system. In nature, thorium rarely does not reach secular equilibrium, and potassium has no disequilibrium problems. However, disequilibrium in the uranium decay chain is common, and can occur in several transitions of the ^{238}U decay chain: ^{238}U can be selectively leached relative to ^{234}U; ^{234}U can be selectively leached relative to ^{238}U; ^{230}Th and ^{226}Ra can be selectively removed from the decay chain; and finally ^{222}Rn (radon gas) is a volatile element and can escape from soil and rocks into the atmosphere. Equilibrium can be restored in days, weeks or even millions of years, according to the half-lives of the radioisotopes involved. Disequilibrium is a serious source of error in gamma ray spectrometry. Uranium concentration estimates are based on the measurement of ^{214}Bi abundance. ^{214}Bi occur far down in the radioactive decay chain and may not be in equilibrium with uranium. Uranium concentration is reported as “equivalent uranium” (eU) because it is based on the assumption of the secular equilibrium. Also, thorium is usually reported as “equivalent thorium” (eTh), although the thorium decay series is almost always in the secular equilibrium condition.

1.2.2 The man-made source of radionuclides

Human activities contribute to increase the levels of radionuclides in the environment. Some activities result in the release of naturally occurring radionuclides to the accessible environment (e.g. producing phosphoric acid from phosphate rocks). Other activities produce novel radionuclides, it includes generating electricity with nuclear power plants and nuclear weapons testing.

The main radioisotopes of anthropogenic origin are: ^{134}Cs, ^{131}I, ^{137}Cs, ^{239}Pu, ^{90}Sr and ^{60}Co.

In this Phd thesis the onliest man-made isotope, which was analyzed but not considered in results, is ^{137}Cs.

^{137}Cs is a radioactive isotope of cesium and is mainly generated as a product of nuclear fission. It has a half-life of 30,07 years and in 94.4% cases it β^- decay in a metastabile isotope ^{137}Ba, the remaining 5,6% are direct β decays in ^{137}Ba. It’s very toxic and highly soluble in water; its presence in soils and rocks is mainly due to the Chernobyl nuclear accident in 1986.

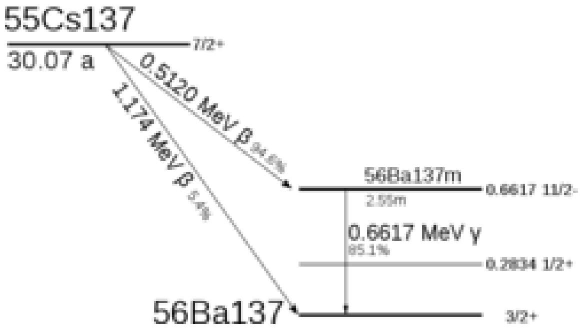

Figure 1.7: *Decay scheme of ^{137}Cs*

Section 2 - Gamma radiation measurements: theoretical basis

In this section we consider the main processes that occur when gamma-rays pass through matter. Gamma-rays interact with atoms of matter through three principal processes:

- **photoelectric effect**
- **compton scattering**
- **pair production**

These processes are fundamental for understanding mechanisms that underlie the generation of a gamma-ray spectrum. Second part of the section is dedicated to the basic properties of gamma-ray spectrum.

2.1 Photoelectric effect

The photoelectric effect is important mechanism of low-energy photons interaction with matter. In this process, photon is absorbed by atom. If the energy of photon is more than the electron binding energy of the material, electron is ejected. For gamma rays of sufficient energy the most probable source of the photoelectrons is the most tightly bound or K shell of the atom, as shown in Fig. 2.1.

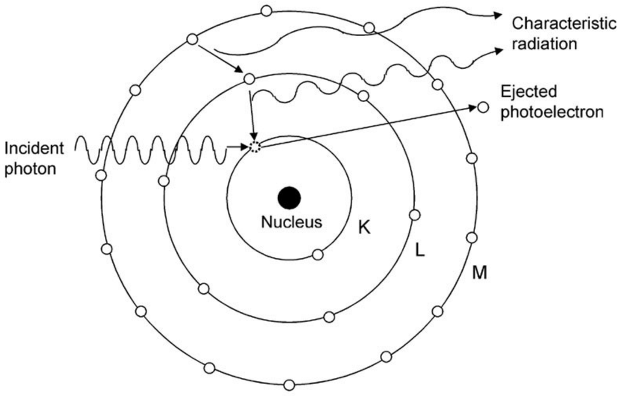

Figure 2.1: *Illustration of the photoelectric absorption process where a gamma ray photon is absorbed and a characteristic X-ray is emitted*

The vacancy created during this ionizing process is filled by an electron from higher shells, thus leading to the possible emission of X-rays. These X-rays are characteristic of the absorber material. Thus, if a photon with energy E ejects an electron from the K shell with a binding energy E_B, then the energy of the ejected electron (E_e) will be given by the following:

$$E_e = E - E_B$$

The recoil energy of the atom is nearly zero and thus can be ignored. In competition to X-ray production, there is a finite probability that the process will result in the emission of an Auger electron from the outer shells, rather than X-rays from the inner shells. This process cannot occur unless the energy of the incident photon, E, is greater than the binding energy of the inner shell, that is:

$$E > E_B$$

As the incoming photon is removed or absorbed from the incident beam, the mass attenuation coefficient is referred to the mass absorption coefficient (τ/ρ), where τ is the photoelectric linear absorption coefficient. The rapid decrease in τ/ρ with increasing E is illustrated in Fig. 2.2.

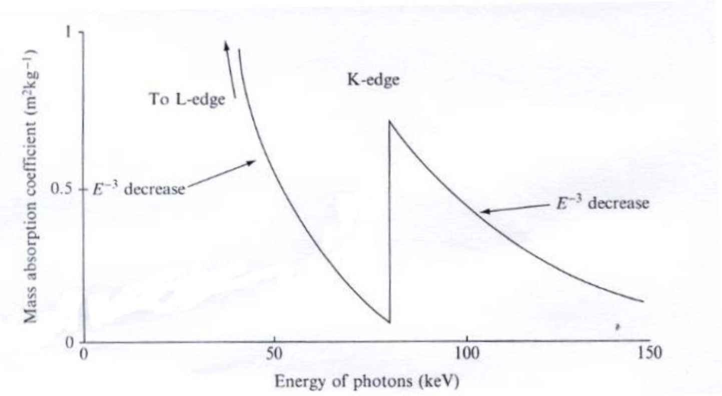

Figure 2.2: *Variation of the mass absorption coefficient with photon energy for the photoelectric process (Modified from Cooper et al., 2003)*

As the photon energy increases, the absorption due to the individual electronic shells becomes important, but as soon as the energy exceeds a particular shell binding energy then the mass absorption coefficient, which gives a measure of the probability of interaction, falls rapidly. In Figure 2.2, the edges refer to the sudden rise in τ/ρ as the energy of the photon approaches the binding energy of a shell. Beyond the edges, τ/ρ decreases rapidly, approximately as $1/E^3$, and increases with atomic number of the absorber Z^3, and thus:

$$\tau / \rho \approx Z^3 / E^3$$

This proportionality is approximately valid for photon energies up to about 200 keV, but at higher energies, τ/ρ varies less strongly and decreases as $1/E^2$, and eventually as $1/E$. This effect is the dominant interaction mechanism for photons of intermediate and low energies (0,5 to 200 keV). The absorption increases rapidly with the atomic number of the absorber and this is the main reason why high-Z materials, such as lead, are used for shielding against γ-rays.

2.2 Compton scattering

Compton scattering can be represented as a collision between a photon and an electron can be considered "free".

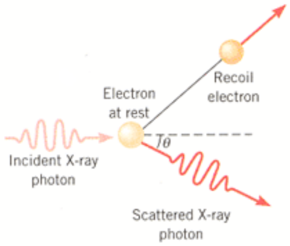

Figure 2.3: *Illustration of the Compton scattering process*

In the collision photon transfers part of its energy to the electron, according with the following equation:

$$E_e = E_\gamma - E'_\gamma = E_\gamma \left(1 - \frac{1}{1 + \frac{E_\gamma}{m_e c^2}(1 - \cos\theta)} \right)$$

where m_e is the electron mass and θ is the scattering angle.

The energy acquired by electron, therefore, depends on the direction in which the incident photon is diverted: if θ = 0°, then E_e is equal to 0, and so is not transferred energy to the detector. If θ = 180°, then the energy acquired by the electron is the maximum possible, but less energy carried by the incident photon. For each possible scattering angle the percentage of energy transferred to the electron is always less than 100%. Compton scattering is particularly important at intermediate γ-ray energies and increases linearly with the atomic number of the absorbing material. This process has particular significance in γ-ray spectroscopy where it leads to the so-called Compton edge and is a major source of background. The mass attenuation coefficient for Compton scattering (σ/ρ) (where σ is the linear attenuation coefficient and ρ is the density of the scattering medium) is proportional to the ratio of the electron density of the scattering medium and the energy of the incoming photon. The mass attenuation coefficient, therefore, decreases with increasing photon energy.

2.3 Pair Production

Pair production is another major process by which photons can interact with matter. During this process, if a high-energy γ-ray interacts with electric field of an atomic nucleus it can create an electron and its antiparticle, the positron. As a consequence of this process the photon completely disappears through the following reaction:

$$E_\gamma = 2m_e c^2 + T_1 + T_2$$

Where E_γ is the gamma-ray photon energy, $T_{1,2}$ are the kinetic energies of the electron and the positron, respectively, and $m_e c^2$ is the rest-mass energy for each of the electron and positron (m is the mass of the electron or the positron and c is the speed of light). In terms of the energy units MeV, the rest mass of an electron or a positron is 0,511 MeV.

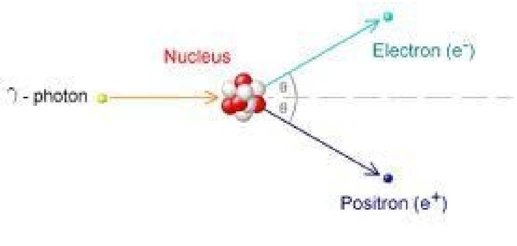

Figure 2.4: *Illustration of the Pair Production process*

As each of these particle have a rest-mass equivalent of 0,511 MeV in terms of energy, equation can be written as follows:

$$E_\gamma (MeV) = 1.02 + T_1 + T_2$$

and thus at least 1,02 MeV energy is required for pair production. Any excess energy appears as kinetic energies of the electron/positron pair, as described by previously equation. In practice, this process for absorbing γ-rays is only important if their energies are greater than about 1,.5 MeV and becomes dominant for γ-ray energies greater than 5 MeV. Since environmentally important radionuclides do not emit γ-rays of these energies, this process is not very significant. The mass attenuation coefficient for pair production, κ/ρ, where κ is the linear attenuation coefficient and ρ is the density of the medium, is given by:

$$\kappa / \rho \approx Z(E - 1.02)$$

This equation shows clearly that unlike the other attenuation processes, pair production increases with increasing of photon energies. It also increases linearly with the atomic number of the attenuating substances.

2.4 Probability of interaction and attenuation of gamma-ray with matter

Probability that a photon will interact with matter, expressed by the cross-section σ (cm^2), depends on the photon energy, E_γ, and on the composition of matter. Figure 2.5 illustrates relationship between scattering, absorption, energy of the incident photon and atomic number of the absorbing medium. Compton scattering is the dominant process for gamma rays from natural sources (*E* up to 2,615 MeV) (Fig. 2.5).

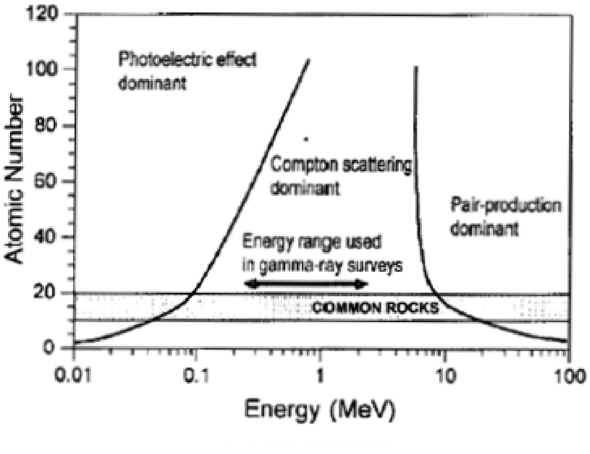

Figure 2.5: *Interaction of gamma rays with matter*

Typically, gamma ray photons lose their energy through successive Compton scattering events until, eventually, the remained low-energy photon is absorbed through photoelectric effect. Under the interaction of gamma rays with matter, the intensity of radiation decreases with distance from source, following the equation:

$$I = I_0 e^{-\mu t}$$

Where I is the beam intensity transmitted through the thickness t, I_0 is the initial beam intensity, t is the thickness of the matter (m) and μ is the attenuation coefficient that represented the probability of interaction per unit length (m^{-1}).

Gamma ray are, typically, the most penetrating radiation, because it consists of photons without mass and electrically neutral (Fig. 2.6). The penetrating depth of gamma rays is about 700 m in air, up to 0,5 m in rocks and few cm in lead and depend on the energy. Gamma rays have a discrete energy specific for each particular radionuclide. As gamma rays are the most penetrating component of natural and man-made radiation, they are widely used in the studies of environmental radioactivity.

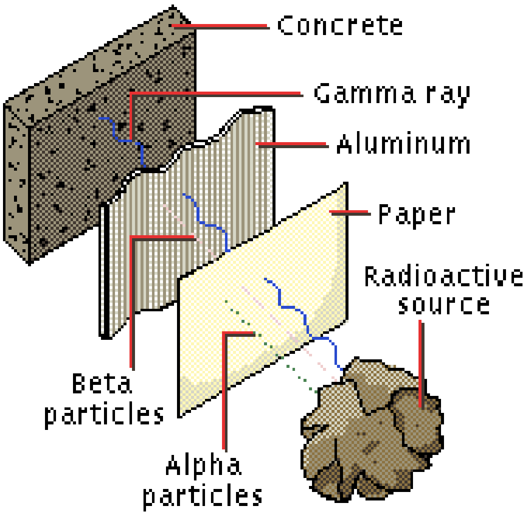

Figure 2.6: *Different range of the alpha, beta and gamma rays*

	Mass attenuation coefficient. (cm^2/g)		Linear attenuation coefficient (m^{-1})			
Isotope	Air	Rock/soil	Air (STP)	Regolith (1 g/cm^2)	Regolith (2.8 g/cm^2)	NaI crystal
Potassium (1.46 MeV)	0.0526	0.0528	0.0068	5.28	14.78	18.39
Uranium (1.76 MeV)	0.0479	0.0482	0.00619	4.82	13.5	16.95
Thorium (2.6 MeV)	0.0391	0.0396	0.00506	3.96	11.1	14.85

Table 2.1: Linear and mass attenuation coefficients for potassium, uranium and thorium isotopes

2.5 Properties of gamma ray spectra

Gamma rays emitted in potassium, uranium and thorium decay chains, in the case of secular equilibrium, have characteristic energy line spectra (Figures 2.7, 2.8 and 2.9).

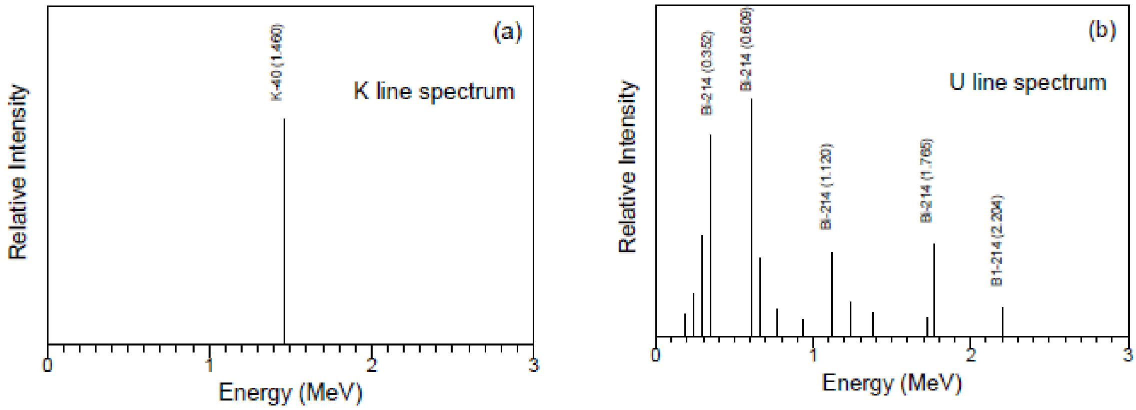

Figure 2.7 and 2.8: *Gamma ray emission line spectra of Potassium (left) and Uranium (right) (Modified from IAEA – TECDOC – 1363, 2003)*

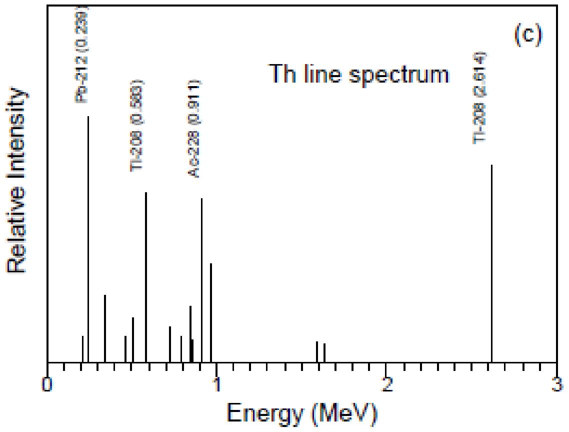

Figure 2.9: *Gamma ray emission lines spectra of Thorium (Modified from IAEA – TECDOC – 1363, 2003)*

These are theoretical abstractions that represent the energy distribution of photons emitted from the source. Each line shows the energy and relative intensity of gamma ray emissions. However, Compton scattering in the source, in the detector, and in matter between the source and detector reduced energies that comes from the originals photons. Scattered and unscattered photons contribution to the gamma ray fluence rate thus depends on the source-detector geometry and on the amount of material between source and detector. Figures 2.10, 2.11 and 2.12 show the simulated gamma ray flux from K, U and Th at 300 m height (Kirkegard & Lovborg, 1974).

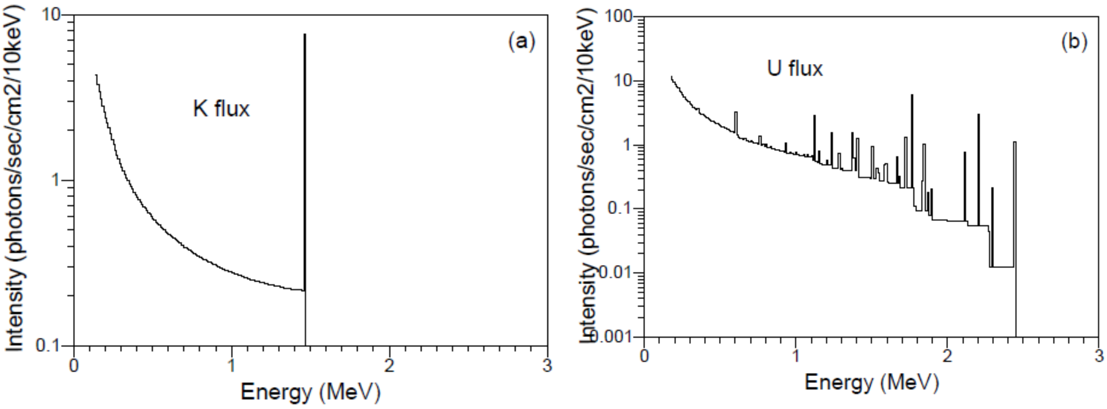

Figures 2.10 and 2.11: *Simulated potassium (left) and uranium (right.) fluence rates at 300 meter height (Modified from IAEA – TECDOC – 1363, 2003)*

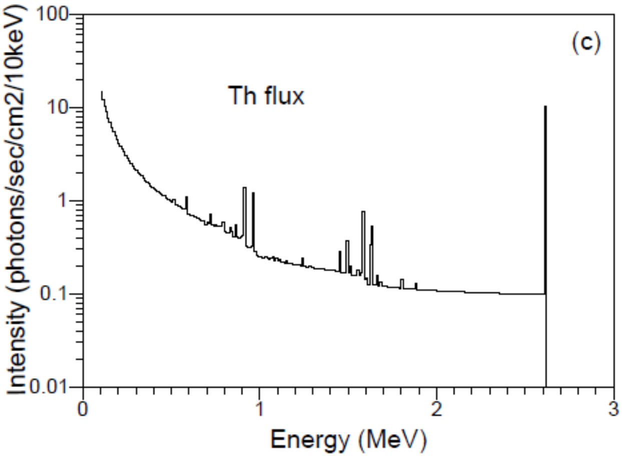

Figure 2.12: *Simulated thorium fluence rates at 300 m height (Modified from IAEA – TECDOC – 1363, 2003)*

Each radionuclide generates a sharp peak (full-energy peak or photopeak), this peak represent the energy of directly transmitted photons. The spectrum of Compton scattered photons shows a continuum of energies up to the maximum energy of the photons emitted by the isotope. This continuum is due to single and multiple scattering events, which happen between source and detector. These events are recorded with an energy equal to that transmitted by the photon to the detector. This energy is less than the energy of the gamma radiation produced from the source. This type of events generates the Compton continuous within the total spectrum. It is almost impossible to record the gamma ray flux spectra shown in figures 2.10, 2.11 and 2.12. This is due to the fact that, in addition to the factors mentioned above, the shape of the spectrum, which have to be measured, is also a function of the detector response.

The main aspect of the detector response are:

- **detector efficiency**: it is relates to how the detector absorbs gamma rays;

- **dead time**: it is refers to the time, which is necessary to the spectrometer to process individual photons;
- **energy resolution of the detector**: it is defined as the full width of a photopeak at half of the maximum amplitude expressed (FWHM) as a percentage (R):

$$R(\%) = (100 * FWHM) / E$$

Where E is the energy of the photopeak. Spectrum of photopeak has a Gaussian shape.

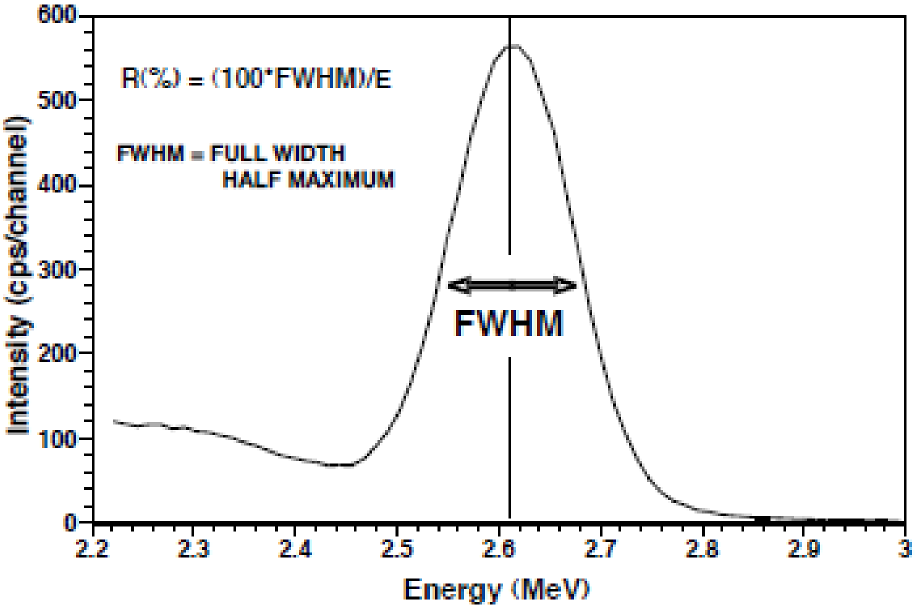

Figure 2.13: *Energy resolution of a gamma-ray spectrometer (After IAEA – TECDOC -1363, 2003)*

- Heath (1964) gives a good summary to the other factors that influence on the shape of the pulse amplitude spectrum, such as **escape events, accidental summing**, and the characteristic "**Compton edge**".

Spectrum measured also includes contribution from background radiation. It is the radiation produced by external sources. There are three main sources of background radiation:

- **Atmospheric radon**: It and its daughter products are the main sources of background radiation. Its daughter products (^{214}Bi and ^{214}Pb) attach to the airborne aerosols and dust particles and decay with emission of gamma rays.
- **Cosmic background**: Gamma rays with high energy and atomic particles of cosmic origin react with atoms and molecules in the upper atmosphere and generate a

secondary radiation. This secondary radiation reacts with surrounding matter and produce a “cosmic” background.

- **Instrument background**: It refers to radiation due to trace amounts of K, U and Th in the detector and surrounding equipment.

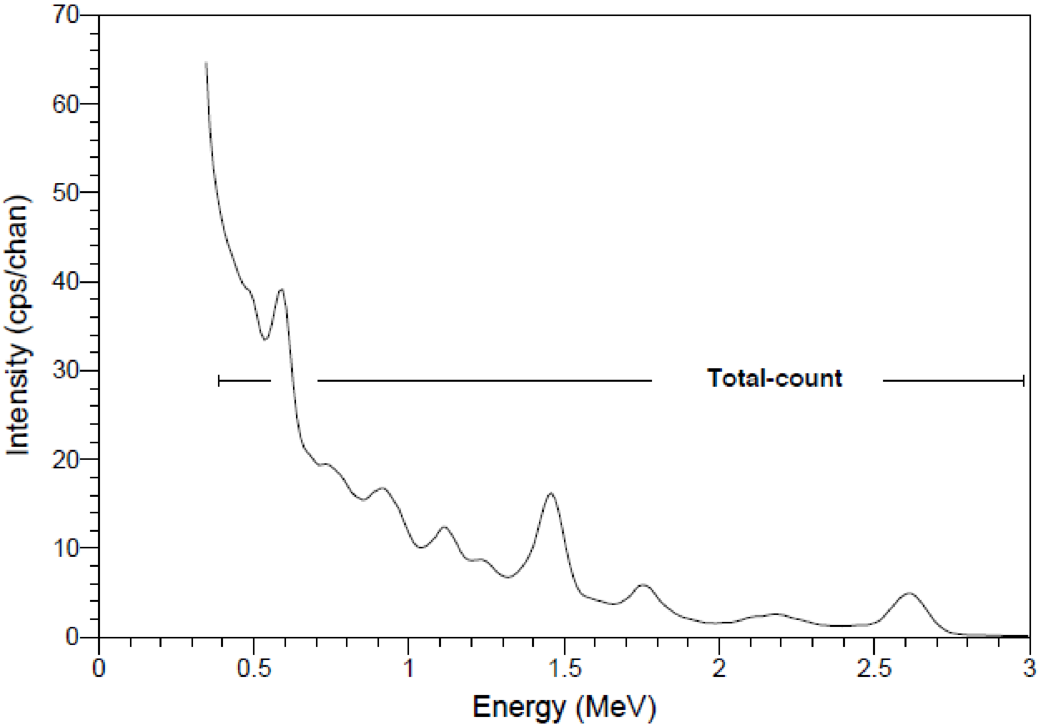

Figure 2.14: *Typical gamma ray spectrum*

Section 3 – Gamma ray detection instruments

In this Phd. thesis were used two gamma-ray spectroscopy techniques: high resolution gamma-ray spectrometry with HPGe semiconductor detectors for measurement (on samples) in laboratory and portable NaI(Tl) scintillation detectors for in-situ measurement (in most cases). In general in-situ measurements were applied in the cases of relatively large (about 1 m^2) rock outcrop surfaces of homogeneous lithology and laboratory measurements were used to characterize heterogeneous outcrops (veins). In this section we briefly describe some important characteristic features of the detectors used in this work:

- NaI(Tl) inorganic scintillation detector
- HPGe semiconductor detector

The principle of operation of both detectors is based on the properties of interaction with matter (crystal) of gamma radiation. So the whole or part of energy is transferred to matter constituent electrons where the primary ionization process is broadly the same in both types of detectors but the collection process is quite different. In semiconductor detectors the primary ionization electrons lose their energy generating secondary electron-hole pairs which are collected producing an electrical signal. In scintillation detectors the secondary electron-hole pairs de-excite emanating electromagnetic radiation (photons) which are collected through photosensitive devices and converted in electrical signal. The electric signal is properly amplified and the response function of the detector is sampled and digitalized through analog-to-digital module (ADC) and a multi-channel analyzer (MCA).

3.1 Basic feature of a gamma radiation detector

Some general properties of gamma radiation detectors which are important for gamma-spectrometry measurements are:

- energy resolution;
- efficiency;
- dead-time.

This features are related with the physical properties of the detector and sometimes are refereed as instrumental limitation, therefore important for the right choice of the instrument.

3.1.1 Energy resolution

The energetic resolution of a detector is the ability to separate energy lines close to each other. The definition of detector energy resolution can be represented from the detector response function to a monoenergetic source of radiation (Fig. 3.1).

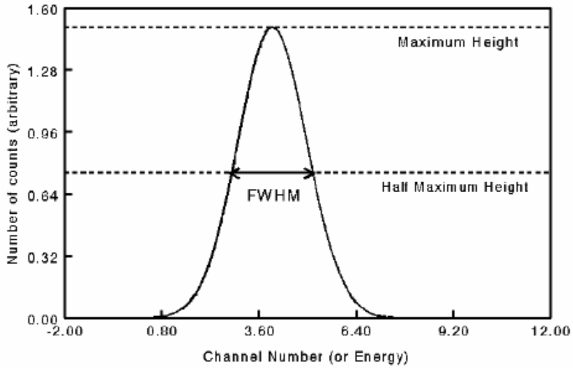

Figure 3.1: *Example of response function of a detector to a monoenergetic radiation source*

$$R = \frac{FWHM}{H_0}$$

where FWHM is the full width at half maximum and H0 is the average pulse height. As a rule of thumb the detector is able to resolve two energies that are separated by more than one value of the detector FWHM.

There are a number of potential sources of fluctuations in the response of a detector which result in imperfect energy resolution. If fluctuations are symmetric and independent, then the response present a Gaussian shape. The main causes of such fluctuation are as follows:

- **Statistical noise**: the charge carriers produced in the detector is a discrete number and subject to random variations. An estimate of the fluctuations can be done assuming that the formation of each charge carriers is described by a Poisson distribution. If products are n charge carriers, then we expect a standard deviation associated with the number of carriers (*n*), then σ equal to $\sqrt{n}$ (statistical noise). As *n* is a large number, then response function *G* has Gaussian distribution:

$$G(E) = \frac{A}{\sigma\sqrt{2\pi}} \exp\left(-\frac{(H - H_0)^2}{2\sigma^2} \right)$$

where E_0 is the energy of the peak and A is the photopeak area. The standard deviation is related to FWHM by the following expression:

$$FWHM = 2.35\sigma$$

The response of many detector is linear, where the output pulse height are proportional to the amount energy amount deposited in the detector ($H_0 = Kn$). The energy standard deviation is $\sigma = K\sqrt{n}$. From this expression can be calculated the resolution due to the statistical noise:

$$R = \frac{2.35}{\sqrt{n}}$$

Resolution increase with increasing of n (this is the reason why semiconductor detectors are more energy resolution than scintillators detector). Some detectors have an FWHM calculated greater than that measured experimentally. The fano factor ($F << 1$ for semiconductor detectors) is introduced as a correction term. Then, the energy resolution is:

$$R = 2.35\sqrt{\frac{F}{n}}$$

- **Electronic noise**: it is related to current fluctuations which occur in electronic circuits of the detector.
- **Fluctuation in charge collection**: it is correlated to any loss or incomplete collection of charge carriers. It depends on the structural characteristic of detector.

3.1.2 Efficiency

The detector efficiency is an important property which allows to relate the number of pulses registered by instruments with the number of photons emitted by the source. Not all radiation emitted by the source gives rise to a signal in detector due to various factors (e.g. geometric configuration, absorption by material interposed between source and detector, response time of instrument). The efficiency can be conveniently divided in two classes: as absolute efficiency and intrinsic efficiency.

Absolute efficiency is defined as:

$$\varepsilon_{abs} = \frac{number\ of\ pulses\ recorded}{number\ of\ radiation\ quanta\ emitted\ by\ source}$$

Intrinsic efficiency is determined by the ratio:

$$\varepsilon_{\mathrm{int}} = \frac{number\ of\ pulses\ recorded}{number\ of\ quanta\ incident\ on\ detector}$$

Absolute and intrinsic efficiency are related by a simple relationship as follows:

$$\varepsilon_{abs} = \varepsilon_{\mathrm{int}} \frac{\Omega}{4\pi}$$

where Ω is the solid angle between detector and source in steradians.

3.1.3 Dead time

The dead time is defined as the minimum time required at the detector system to separate two events in order that they be recorded as two separate pulses. Recording is not instantaneous, but requires a certain time that depends on the characteristic of detector and electronics. During this period, detector can be sensitive or insensitive to radiation. If detector is insensitive, every event that occurs during the dead time is lost. If detector is sensitive to the arrival of a second event causes a restart of dead time.

3.2 Inorganic scintillation detector

Scintillation counter consist of a hermetically canned scintillator crystal which is optically coupled with a photomultiplier tube (Fig. 3.2). The scintillation effect depend on the fact that when certain solid or liquid material, called phosphors, are exposed to ionizing radiation, excitation of some kind occurs in the material and de-excitation of the material results in the emission of visible radiation. The prompt emission of visible radiation is also called fluorescence.

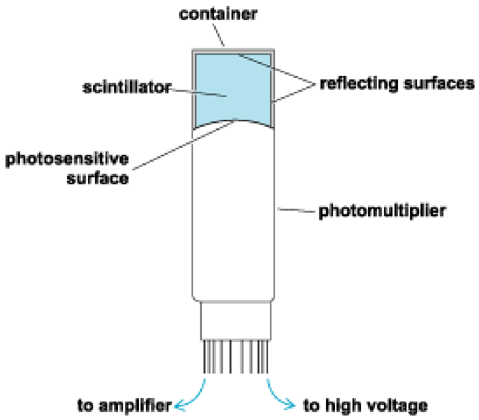

Figure 3.2: *Scintillation counter*

The flashes of light produced have very short time duration and low intensity and are not measured directly. Instead, they are allowed to interact with a photocathode which results in the release of photoelectrons. These are then multiplied in a device known as a photomultiplier tube (PM). The light quanta are thus converted into pulses of electrical charge, which can then be amplified and counted. The inorganic scintillators are the most important group of solid scintillators. A wide range of substances are now commercially available as inorganic scintillators. These usually contain at least one and some of them two elements with high atomic number: NaI(Tl) have an effective atomic number of 49.7. It is the presence of these elements which provides to the scintillator with its relatively high efficiency, even for high-energy gamma-rays. Secondly, many of the materials are ‘doped’, i.e. small amounts of impurities have been deliberately introduced into the main crystal lattice. For example NaI(Tl) crystal, is a NaI crystal doped with a small amounts of thallium ions (0.1 % of weight mass), called also activator. This introduction of an impurity ion has important effects on the quality of the light output from the scintillator. When ionizing radiation passes through the scintillator, electrons are promoted from a lower to a higher, excited state. The return of the electron to the lower state results in a fraction of them emitting a light photon. The activator promotes these transitions and also shift the wavelength of the emitted radiation into the visible range which better matches the requirements of the photomultiplier tubes (Fig. 3.3) used in conjunction with the scintillator. This shift in wavelength also means that the crystal is essentially transparent to the light emitted. It is important that the light output should be a linear function of the energy of the radiation. Most scintillator exhibit such behavior and thus provide a linear response with the energy of the radiation. The energy resolution of a scintillator is set by the fluctuations in the number of light quanta generated by radiation of a specific energy.

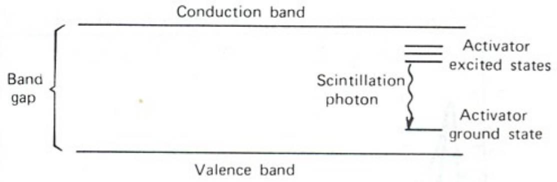

Figure 3.2: *Band structure of an inorganic scintillator crystal. Activator introduce energy levels into energy gap between conduction band and valence band*

The scintillators are optically coupled to a system of light amplification, the photomultiplier tube (PM) (Fig. 3.4).

The major components of a PM are:

- **Photocatode**: it converts photons into a equivalent number of electrons and is therefore the source of electrons in the photomultiplier tube. The face of the photomultiplier tube is made of glass on which is coated a material (usually a combination of alkali metals and antimony), which release electrons when irradiated with light photons. These electrons, known as photoelectrons, are then accelerated and focused onto the first dynode of the tube. The sensitivity of the photocatode is estimated by a parameter named quantum efficiency (QE), defined by the following formula:

$$QE = \frac{number\ of\ photoelectrons\ emitted}{number\ of\ photons\ incident}$$

- **Dynode chain**: it makes the electron multiplication. When the photoelectrons strike the first dynode, a number of secondary electrons are produced and emitted from the surface of the dynode material. These emitted secondary electrons are then accelerated towards the second dynode, where further secondary electrons are produced. This process is then repeated down the chain of dynodes. The final bunch of electrons emitted from the final dynode is then collected by the anode.
- **Anode**: it converts an electronic current generated in the dynode chain into an equivalent voltage pulse.

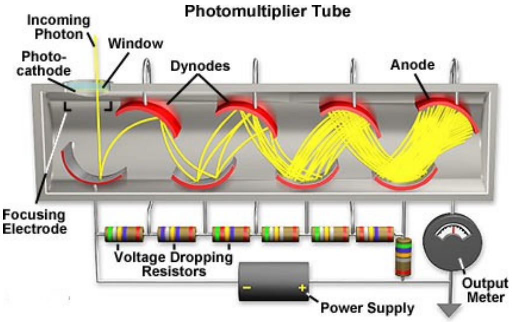

Figure 3.4: *A photomultiplier tube*

3.2.1 NaI(Tl) detector

In this work we used for in-situ measures a NaI(Tl) detector. Thallium-activated sodium iodide NaI(Tl) crystal is mainly used as detectors in field gamma ray surveys. It has a density of 3,66 g/cm^3, and can be manufactured in large volumes. It has an exceptional light output: ≈ 38000 photons per MeV. The detection efficiency of up 100% for low-energy gamma rays but somewhat less for high-energy gamma rays. The dead time is the order of 10^{-7} s. The main disadvantage of NaI(Tl) is that the crystal is hygroscopic and so has to be kept perfectly dry and cannot be exposed in the atmosphere. Consequently, it has to be kept permanently inside a suitable can and so cannot be used in "window-less" mode. It also has to be taken into account the possibility of any damage for mechanical or thermal shock.

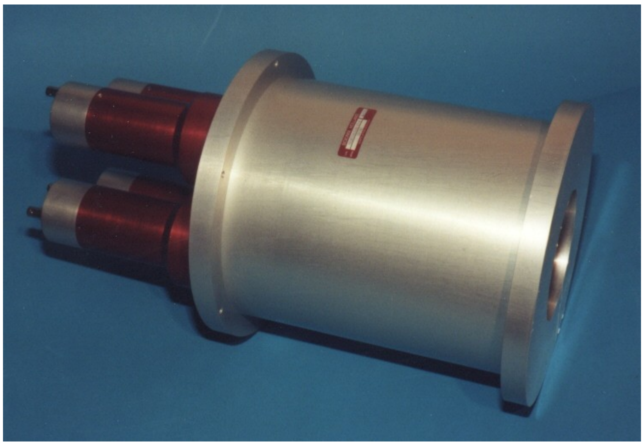

Figure 3.5: *Example of an NaI(Tl) detector*

3.3 Semiconductor detector

The semiconductors materials used as radiation detectors are generally made from crystalline silicon or germanium. In such materials, the atoms are bounded together via valence electrons and each atom is bound with other four. In energy terms, these atoms are in the "valence band". Above the valence band, lies the "conduction band". In metals, the energy gap ("band gap") between these two bands is small and so electrons are easily promoted from the valence to the conduction band, where they can travel through the crystal lattice quite freely. This freedom of movement of electrons in the conduction band is why metals are good electrical conductors. Conversely, in insulators the band gap is very wide (Fig. 3.6) and virtually no electrons are found in the conduction band – hence their do not conduct electricity. Semiconductors lie between these two extremes. In highly pure form of both silicon and gernanium, the band gap is of order of eV and promotion of the valence electrons from the valence to the conduction band is only brought about at high temperatures so that these materials have high resistivity at ambient temperatures. The flow of electrons due to thermal agitation provides a background signal, which is not associated with the recording of a radiation events. Therefore such detectors works at low temperatures in order to limit the number of electron that can jump in the conduction band for thermal agitation. Like inorganic detectors, these pure materials are "doped" with elements that are either one place above or below them in the Periodic Table, altering in this way the electronic structure by increasing the presence of free carriers and effectively reducing the band gap.

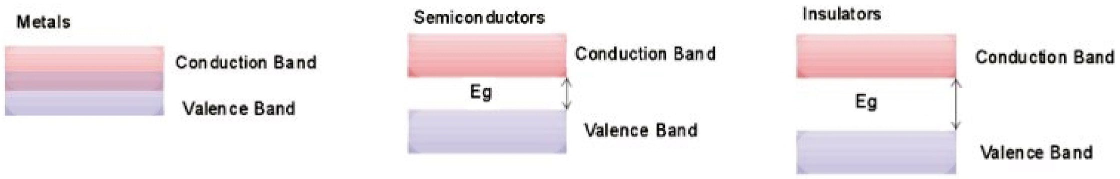

Figure 3.6: *Band structure of metals, semiconductors and insulators*

3.3.1 High-purity Germanium detector

In this thesis measurements in laboratory were done using HPGe detectors. Germanium has an atomic number Z = 32, an energy gap between valence and conduction band E_g = 0,67 eV, and the energy required to create an electron-hole is equal to 2,96 eV at a temperature of -196 °C. To be used as detectors for gamma radiation must be kept at very low temperature (tipically -196 °C) to minimize the background current caused by thermal agitation; therefore it is necessary to use a cooling system, tipically consisting from a Dewar vessel in which a tank of liquid nitrogen (LN_2) is kept in thermal contact with detector. To obtain materials of high purity is needed to reduce concentrations of impurities up to 10^{10} atoms per cm^3 and obtain a depletion region of 10 mm for a reverse bias voltage of 1000 V. The detectors fabricated with this type of ultra-pure germanium are called HPGe (High-purity Germanium) (Fig. 3.7). The technique developed to produce ultra-pure crystals is called refining areas: impurities are progressively eliminated locally heating the germanium. Germanium is melted in a quartz crucible in which temperature is kept just above melting temperature (959 °C). A small single crystal seed is cut from the purified crystal precisely along the crystal planes, and plunged in crucible containing molten Germanium. Before you leave refund some seed and then extracted with slow rotation. Crystal growth is a process that requires high precision and this is the reason that limits the size of a semiconductor detector. The crystal has within it a small amount of impurities: if remaining impurities are acceptors, electrical properties are those a crystal weakly doped p-type, otherwise n-type. The depletion region is achieved by creating a diode structure; for example, lithium is evaporated onto a surface of the crystal weakly doped p-type creating a contact n+ that typical thickness of 600 μm. On another surface boron ions are inserted with typical thickness of 0,3 μm creating a p+ contact. By applying a reverse voltage charges are separated and create so-called area-discharge which is the active volume of the detector.

Figure 3.7: *HPGe detector*

3.3.1.1 MCA_Rad

In University of Ferrara (Physics Department) has been developed a system for measuring environmental radioactivity called MCA_Rad that can measures a large number of samples with minimal assistance from an operator (Fig. 3.8). Through this instruments can be measured all types of material (solid, liquid or gas) and thanks to its high efficiency it allows measurements of absolute activity with uncertainties of less than 5%. The core of the MCA_Rad system is made of two 60% relative efficiency coaxial p^+-type HPGe gamma-ray detectors having an energetic resolution of about 1.9 keV at 1332.5 keV (^{60}Co). The new cooling technology which use mechanical coolers permits to simplify the management of the system. The detectors are accurately shielded and positioned facing each other 5 cm apart. With a lead shielding size 20 cm x 25 cm x 20 cm and a core copper shielding size 10 cm x 15 cm x 10 cm, the background recorded in the measuring chamber due to the ^{40}K (1460 keV) is reduced to 32 counts/hour and that due to the ^{214}Bi (609 keV) is 14 counts/hour. Samples are introduced between the two sides of the detector through a rectangular opening of 5 x 10 cm^2. Sample material is contained in a cylindrical polycarbonate box of 75 mm in diameter, 45 mm in height and 180 cm^3 of useful volume, labeled by a barcode. Up to 24 samples can be charged in a slider moving on gravity and further introduced at the inner chamber through an automatic "arm" made of copper, lead and plastic closing the lateral hole of the housing. The mechanical automation consists on a barcode scanner and a set of compressed air driven pistons, which permits, first the sample identification, and second to introduce/expel the samples. The full operations is controlled by a PC where a dedicated software runs the measurements.

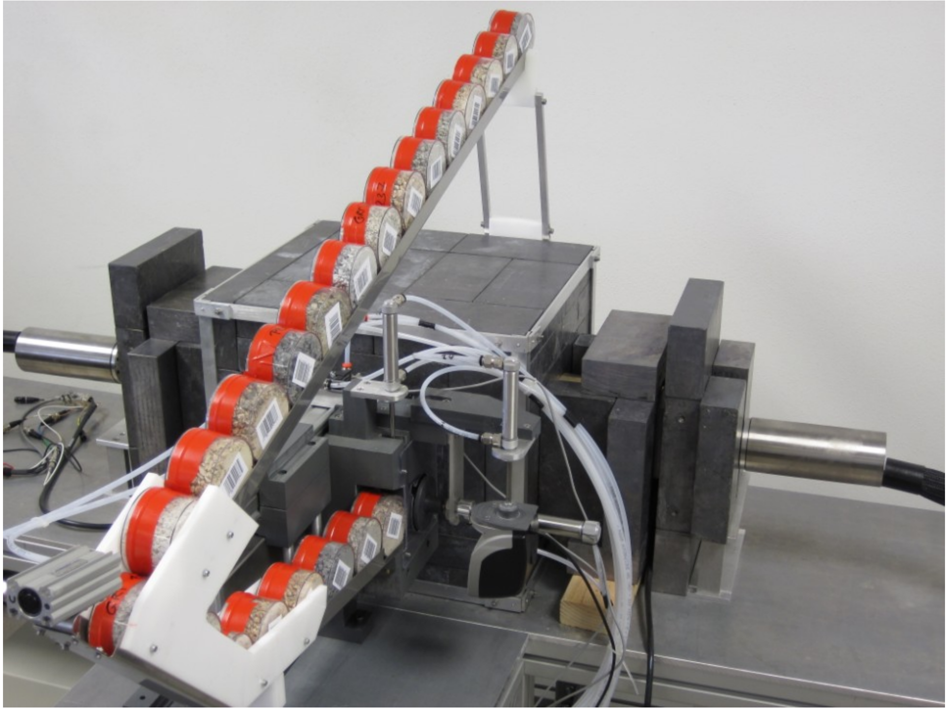

Figure 3.8: MCA_Rad system in University of Ferrara

Section 4: Portable gamma-ray spectrometer

In this section will be describe the basic characteristics and management software of the portable gamma-ray spectrometer used for in-situ measurements. In addition, we report the calibration procedure and the differences between MCA_Rad and portable spectrometer.

4. 1 Description

The equipment developed at the National Laboratory of Legnaro (INFN) (Fig. 4.1), consists of a scintillation detector NaI(Tl) crystal of 1L volume coupled with an HV supply, preamplifier and multichannel Analyzer (MCA) (digiBASE by ORTEC) and governed by a netbook. In Figure 4.1 is shown the detector and photomultiplier tube canned in an aluminum case and connected to a integrated signal processor called DigiBASE. The DigiBASE supplies the high voltage to the detector and sampling of the pulses converting them after amplification from analog signal coming from the detector into a digital signal. Everything is connected via a USB cable to a netbook, and finally information is analyzed using two software: a commercial software called "Maestro" which permits to control the spectrum acquisition parameters, and "jRadView" a self–programmed software which is used for spectrum analysis and used to calculate automatically activity concentration of K, U and Th.

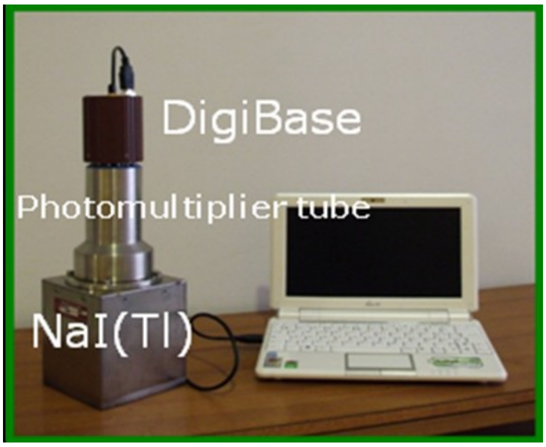

Figure 4.1: Portable gamma-ray spectrometer connected to net book.

The main features of this instruments are:

- Measurement quickness: good accuracy in 5 minutes;

- **In situ detection of radioisotopes:** instrument is able to discriminate different natural isotopes in situ through a spectral analysis:
- **Conformity with international guidelines:** hardware and software of devices are constructed by taking as reference IAEA and ANSI international guidelines;
- **Easy to use:** it can be easily managed by single person;
- **You can carry out measurements in extreme environment and difficult condition**.

The equipment is contained in backpack (Fig 4.2). For our measurements we have always placed instrument on the ground. For a detector placed on the ground, the effective rock sample has a thickness of approximately 25 cm, a radius of 1 m, and a mass exceeding 100 kg (IAEA TECDOC-1363, 2003).

Figure 4.2: Spectrometer during in-situ acquisition

4.2 jRadView software

jRadView software was designed, with our collaboration, by the research group of dr. Fabio Mantovani, and is updated periodically. Algorithms of jRadView software following the main international guide lines (ANSI, 1999; IAEA TECDOC-1363, 2003). The code allow to determine the activity concentration of ^{40}K, ^{214}Bi (^{238}U decay series), ^{208}Tl (^{232}Th decay series) in Bq kg^{-1} and to calculate their respective abundance expressed in ppm for uranium and thorium and in % for potassium. We can also obtain the concentration in the rocks of the ^{137}Cs express in cps through full spectrum analysis as described later. The uranium and thorium activity concentration and abundances are calculated under the consideration that their respective decay series are in secular equilibrium and therefore indicated as equivalent uranium (eU) and thorium (eTh). With the aim to increase the statistics in a short acquisition time and extend the analysis beyond the three main radioisotopes (^{40}K, ^{214}Bi and ^{208}Tl), we developed a method for data analysis that consider the full spectrum analysis with non-negative least square (FSA-NNLS) constrains (Caciolli et al., 2011, in press). Only the energy range from 300 keV up to 2900 keV is considered in the analysis. Below 300 keV there is a strong presence of the backscattering events which depends on the atomic number and density of the surrounding materials. Above 2900 keV only the cosmic ray contribution is present. Counts recorded in the energy range between 300 and 2900 keV corresponds to about 867 energy bin (3 keV for each channel). With FSA method, the overall spectrum is analyzed as results of the composition of the basic spectra product by cesium, potassium, thorium, uranium and background (Fig. 4.3). Overlap of the different components determines the shape of the spectrum, while weight of each element is determined by its concentration in the sample.

The events registered in each channel in the measured spectrum, N, can be expressed as:

$$N(i) = \sum_{k=1}^{4} C_k S_k(i) + B(i)$$

where N(i) are the count in the channel *i*; C_k are the concentration of the element *k*; $S_k(i)$ are the associated counts to the fundamental spectrum of the element *k* in the channel *i*; B(i) are the counts in the channel *i* due to the intrinsic background and the index k stays for ^{40}K, ^{232}Th, ^{238}U and ^{137}Cs.

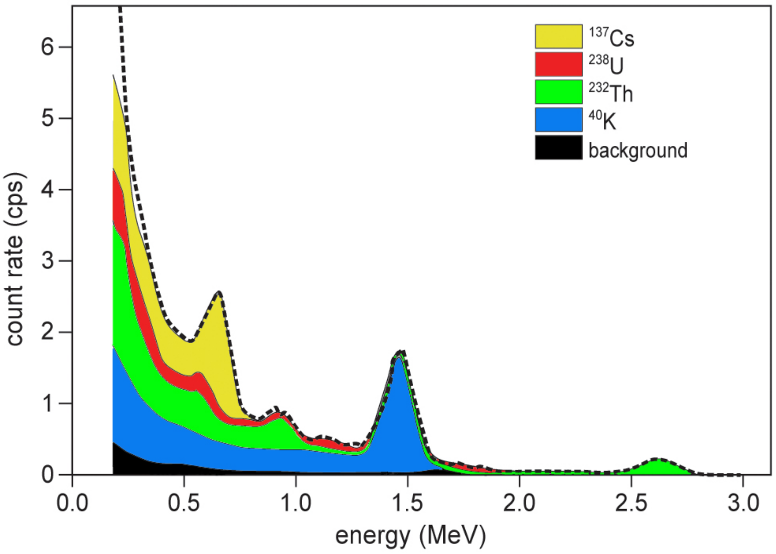

Figure 4.3: *Total spectrum*

During calibration of the system, carried out by Dr. Fabio Mantovani and its research group and described in Caciolli *et al.* (2011, in press), the fundamental spectra (S matrix) are obtained by solving previously equation with the radionuclide concentrations (the C_k coefficients). Once the first solution has been obtained, in order to improve the χ^2 minimization, a trimming procedure is executed by changing the site concentrations (C_k) in small steps around the measured intervals and repeating the matrix solution.

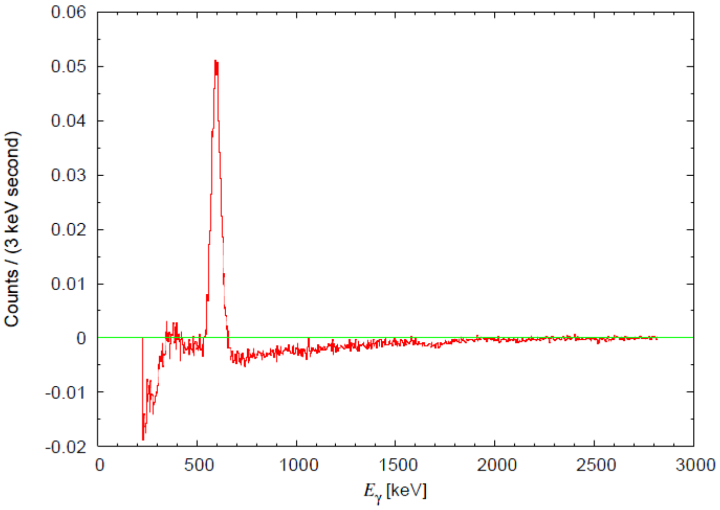

Figure 4.4: *The sensitive spectra of* ^{137}*Cs, obtained using the FSA method. Green line is placed to show zero counts level (Modified from Caciolli et al., 2011, in press)*

The χ^2 minimization without any further conditions, which is the base of the FSA method, can bring to sensitive spectra having energy regions of negative counts. Two evident examples of this problem are shown in Figure 4.4 and 4.5. The presence of these non physical results introduces crosstalk effects in the analysis, leading to systematic errors.

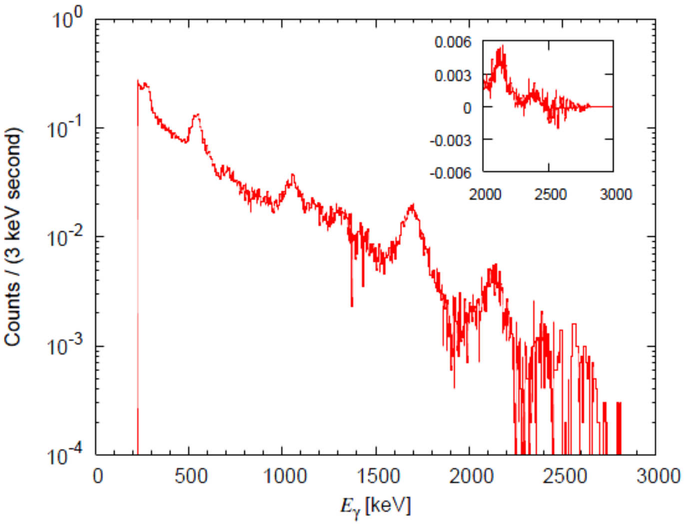

Figure 4.5: *The sensitive spectra of* ^{238}*U; obtained used the FSA method. In the small box is reported negative counts (Modified from Caciolli et al., 2011, in press)*

The NNLS (Non Negative Least Square) constraint (Lawson & Hanson, 1995; Désesquelles *et al.*, 2009; Boutsidis & Drineas, 2009), which forces the counts on each bin to be zero or positive, has been for the first time implemented in the FSA algorithm in order to avoid this problem (Baldoncini, 2010). The sensitive spectra calculated with the new algorithm are shown in Fig. 4.6, where it can be directly seen a more reliable sensitive spectra with the NNLS implementation.

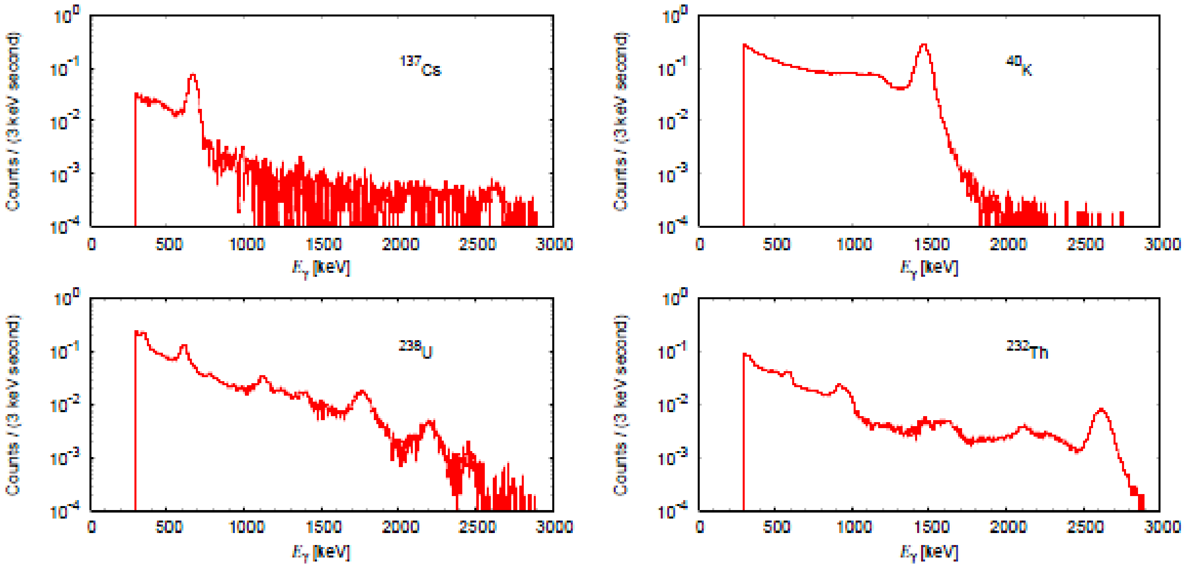

Figure 4.6: *Sensitive spectra obtained through the FSA with NNLS constrains (Modified from Caciolli et al., 2011, in press)*

4.3 Calibration

Calibration is used to estimate the detector sensitivity in presence of a source of radioactivity. An instrument with known characteristic is used to determine the concentration of radioactive elements. Once you know radionuclides concentration and energy distribution of the counts is possible to determine the sensitivity constants. When sensitivity of the detector is determined we carried out radiometric measures in the site investigated.

To make a good tool calibration is necessary to create a calibration system consists of several radioactive sources with properties similar to the following:

- Uniform distribution of the radioisotopes;
- Wide and flat surface that approximates an infinite geological source;
- Low moisture content;
- Sealed surface to prevent the radon escape;
- Low porosity and homogeneity.

The IAEA recommends to calibrate using artificial pad. An artificial pad is a slab of concrete containing known concentration of radioelements (Tab. 4.1). The IAEA (IAEA, 1989) recommended 4 cylindrical concrete pads with dimension: diameter about 3 m and thickness about 0,5 m. Each of the pads is enriched in either K, U or Th. The fourth pad serves as background pad. The pads must be sufficiently radioactive to minimize the acquisition time necessary to have a good statistic, but without distorsions in the spectrum that can determine constants sensitivity unreliable. For NaI(Tl) detector, the ideal concentration must not exceed the rate of 2000 counts sec^{-1}.

Ideal concentration established by the IAEA are given in Table 4.1.

Block Type	K (%)	eU (ppm)	eTh (ppm)
Background	0	0	0
K	8	0	0
U	0	50	0
Th	0	0	125

Table 4.1: *Ideal concentration for the calibration blocks*

Pad as those of Table 4.1 are impossible to build because you can’t construct pad completely potassium, uranium and thorium free.

Then you should build blocks that have concentrations equal to those value reported in Table 4.2 following the guideline of the IAEA.

Block Type	K (%)	eU (ppm)	eTh (ppm)
Background	0,5	1,1	1,4
K	6,5	1,1	1,4
U	0,5	50	1,5
Th	0,5	6,4	125

Table 4.2: *Real concentration for the calibration blocks*

Artificial pads, however, are difficult to achieve and very expensive. For this reason concentration values of Table 4.2 are used as references for the choice of natural sites. The calibration sites are outcrop of rocks characterized by a relative abundance of one element other then. Background measurements are done on small boat in water about 200 meters from the coast. Natural sites selected for the calibration of the our portable spectrometer, could satisfy concentration characteristics of an ideal calibration system (Tab. 4.2). Spectrometer must be place on the ground. Acquision time is 30 minutes. . In each test sites at least 5 samples are collected, and analyzed with the MCA_Rad in laboratory. One sample are collected under portable spectrometer and others 1 meter away (Fig. 4.7). MCA_Rad measurements during about 1 hour, are affected by a statistical uncertainty of less than 10%.

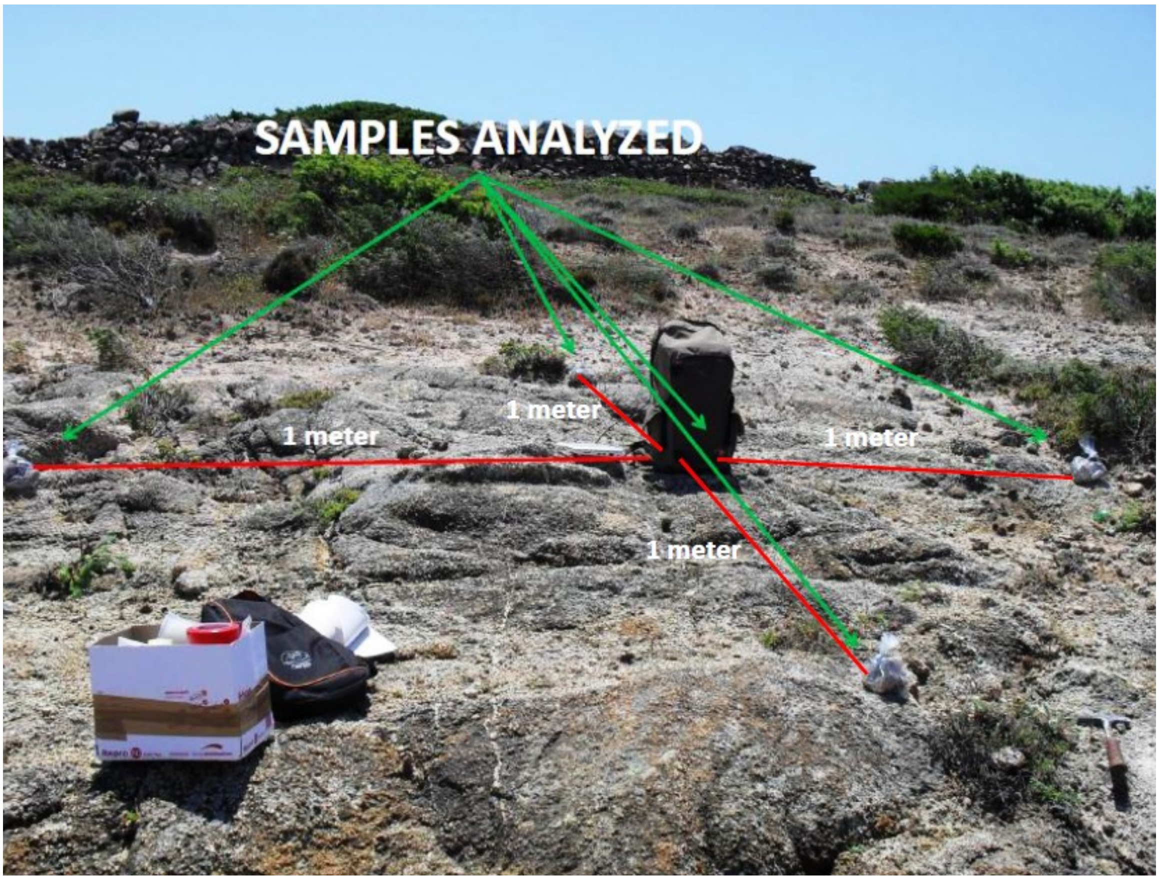

Figure 4.7: *Example of calibration test*

4.4 Portable spectrometer vs. MCA_Rad

The main differences between portable spectrometer and MCA_Rad are:

- **Efficiency:** MCA_Rad has less efficiency than the portable gamma ray spectrometer;
- **Energy resolution:** MCA_Rad has more energy resolution than the NaI(Tl) scintillator (Fig. 4.8);
- **Measurements length:** MCA_Rad acquisition time during 1 hour; portable gamma ray spectrometer during 5 minutes;
- **Interaction volume (Figures 4.9 and 4.10):** MCA_Rad interaction volume is about 200 cm^3, NaI(Tl) portable detector interaction volume is about 785000 cm^3;

- **Price:** MCA_Rad is more expensive than portable gamma-ray spectrometer.

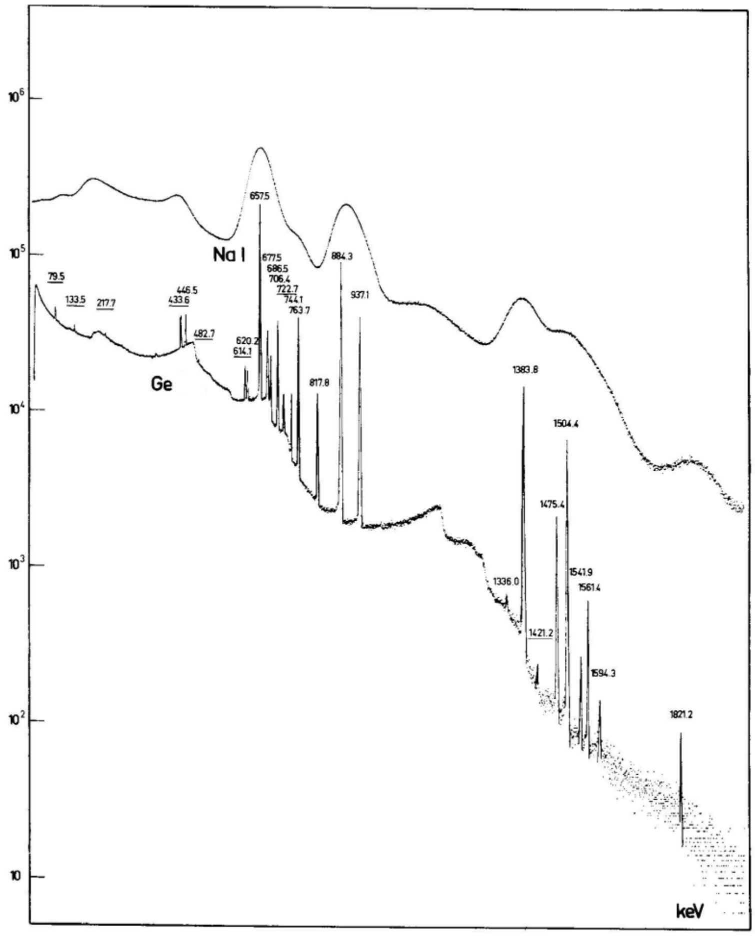

Figure 4.8: *Comparison of Ge and NaI(Tl) spectra, showing the greater resolution of Ge detector (Modified from Baldoncini, 2010)*

Figures 4.9 and 4.10: Comparison of portable spectrometer (left) and MCA_Rad (right) interaction volume

Section 5: Geochemistry of the radioelements in the crust

Natural radioactivity, in the crust, is due to the presence of high concentration of primordial radionuclides. In this section we describe the distribution of K, U, Th in the crust and some basic concepts of their geochemistry.

5.1 Distribution of the radioelements in the crust

Most of natural radioactivity in the crust is due to the presence of three elements as K, U and Th. The average abundance of U, Th and K in the upper crust is about 3 ppm, 10 ppm and 2.33% respectively (Dickson & Scott, 1997). U, Th and K and other minor radioactive isotopes preferentially concentrate in acid and alkaline rocks. Basic and ultrabasic rocks have extremely low levels of radionuclides.

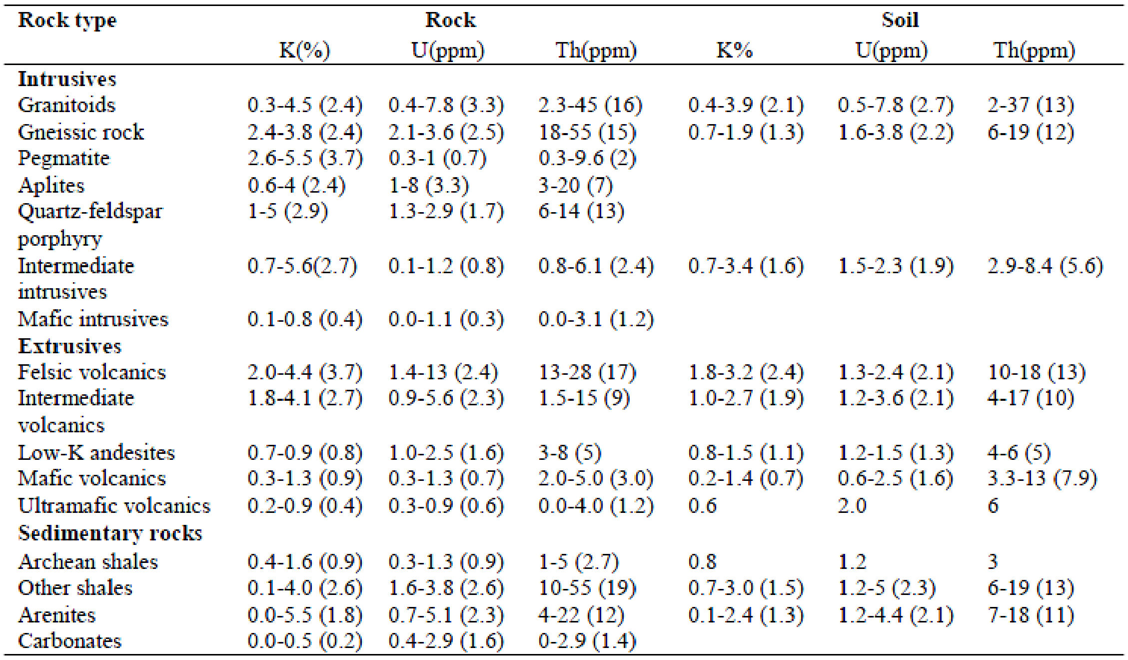

Rock type		**Rock**			**Soil**	
	K(%)	U(ppm)	Th(ppm)	K%	U(ppm)	Th(ppm)
Intrusives						
Granitoids	0.3-4.5 (2.4)	0.4-7.8 (3.3)	2.3-45 (16)	0.4-3.9 (2.1)	0.5-7.8 (2.7)	2-37 (13)
Gneissic rock	2.4-3.8 (2.4)	2.1-3.6 (2.5)	18-55 (15)	0.7-1.9 (1.3)	1.6-3.8 (2.2)	6-19 (12)
Pegmatite	2.6-5.5 (3.7)	0.3-1 (0.7)	0.3-9.6 (2)			
Aplites	0.6-4 (2.4)	1-8 (3.3)	3-20 (7)			
Quartz-feldspar porphyry	1-5 (2.9)	1.3-2.9 (1.7)	6-14 (13)			
Intermediate intrusives	0.7-5.6(2.7)	0.1-1.2 (0.8)	0.8-6.1 (2.4)	0.7-3.4 (1.6)	1.5-2.3 (1.9)	2.9-8.4 (5.6)
Mafic intrusives	0.1-0.8 (0.4)	0.0-1.1 (0.3)	0.0-3.1 (1.2)			
Extrusives						
Felsic volcanics	2.0-4.4 (3.7)	1.4-13 (2.4)	13-28 (17)	1.8-3.2 (2.4)	1.3-2.4 (2.1)	10-18 (13)
Intermediate volcanics	1.8-4.1 (2.7)	0.9-5.6 (2.3)	1.5-15 (9)	1.0-2.7 (1.9)	1.2-3.6 (2.1)	4-17 (10)
Low-K andesites	0.7-0.9 (0.8)	1.0-2.5 (1.6)	3-8 (5)	0.8-1.5 (1.1)	1.2-1.5 (1.3)	4-6 (5)
Mafic volcanics	0.3-1.3 (0.9)	0.3-1.3 (0.7)	2.0-5.0 (3.0)	0.2-1.4 (0.7)	0.6-2.5 (1.6)	3.3-13 (7.9)
Ultramafic volcanics	0.2-0.9 (0.4)	0.3-0.9 (0.6)	0.0-4.0 (1.2)	0.6	2.0	6
Sedimentary rocks						
Archean shales	0.4-1.6 (0.9)	0.3-1.3 (0.9)	1-5 (2.7)	0.8	1.2	3
Other shales	0.1-4.0 (2.6)	1.6-3.8 (2.6)	10-55 (19)	0.7-3.0 (1.5)	1.2-5 (2.3)	6-19 (13)
Arenites	0.0-5.5 (1.8)	0.7-5.1 (2.3)	4-22 (12)	0.1-2.4 (1.3)	1.2-4.4 (2.1)	7-18 (11)
Carbonates	0.0-0.5 (0.2)	0.4-2.9 (1.6)	0-2.9 (1.4)			

Figure 5.1: *Radioelements concentration of Australian rocks and soil (Average value in brackets) (Modified from Dickson and Scott, 1997)*

Magmatic rocks, generally, show an increase of radioelements with increase of SiO_2 (Fig. 5.2).

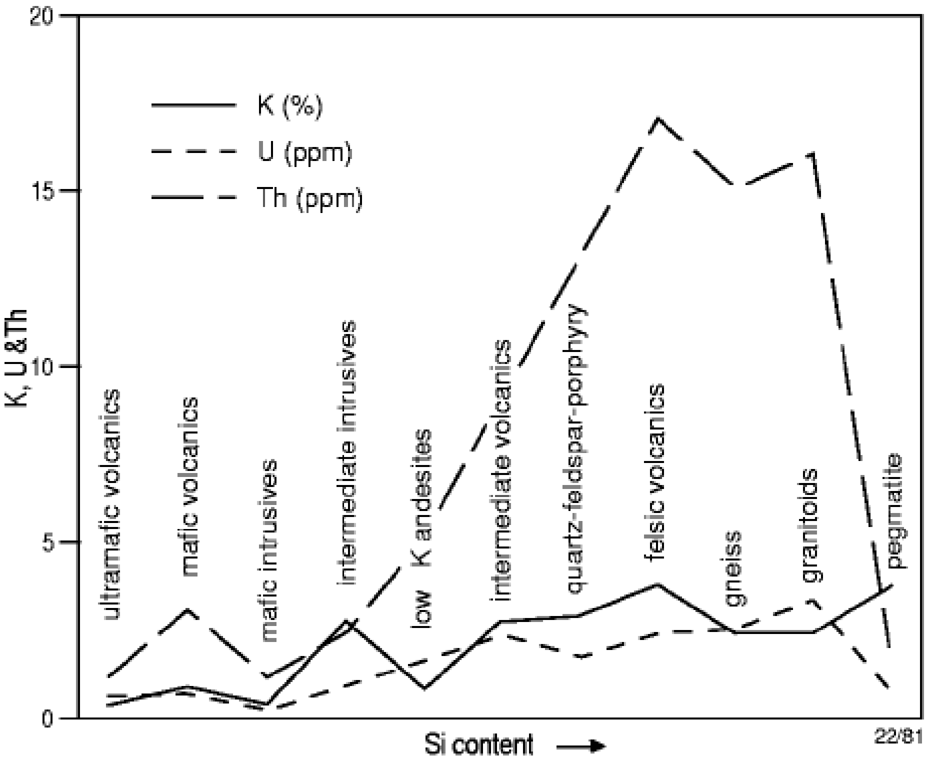

Figure 5.2: *K, U and Th average abundances for igneous rocks with increasing of SiO2 content (Modified from Dickson and Scott, 1997)*

In sedimentary rocks, radionuclides concentration depends on the environmental conditions which occurred during deposition and diagenesis. Metamorphic rocks generally retain the concentration of protolites.

Radioactive elements have an important role both as main constituent and as vicariant elements of both main and accessory mineral phases. Moreover uptake of radioactive elements by tunneled mineral phases such as e.g. hollandite, zeolites can increase the content of exchangeable radioactive nuclides. These nuclides can easily be released if changes of the physical-chemical condition occur.

Petrogenetic processes (hydrothermal or magmatic) forming primary minerals. They are important in the distribution of the radioactive nuclides even if supergene processes can account for very high concentration.

5.2 Uranium

Uranium is a metallic element of the actinides serie, with atomic number 92. Uranium has four oxidation states U^{3+}, U^{4+}, U^{5+} and U^{6+}, the most important of which are U^{4+} and U^{6+} (Fig. 5.3).

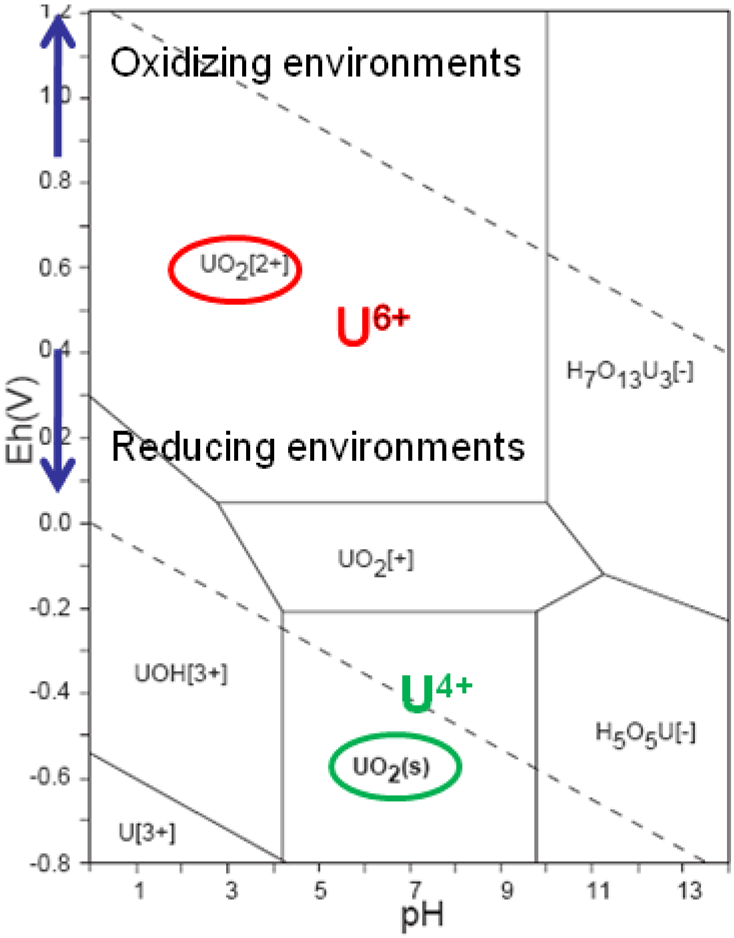

Figure 5.3: *Eh-pH diagram of the system U-O-H at 298.15 °K and P = 10^5 Pa (Modified from Takeno, 2005)*

The geochemical behavior of uranium is influenced by:

- Redox conditions (Eh),
- pH;
- Water-rocks or water-soils reactions.

The hexavalent form is more mobile in the environment compared with the tetravalent form. Such a mobility is due to the high solubility of the uranyl complex $(UO_2)^{2+}$. Changes in the redox conditions may cause uranium reduction to the tetravalent form which is removed from the solution by precipitation. In reducing environments U precipitates as U_3O_8 (Pitchblende) or UO_2 (Uraninite), in sedimentary environments as Autunite. U appears as U^{4+} in igneous rocks with crystallochemical properties close to Th^{4+} and Light Rare Earth Elements (LREE), which explains the coherent geochemical behavior of U, Th and LREE in igneous rocks (Bea, 1999). This coherence is lost in hydrothermal and supergene conditions, where uranium is partially or totally oxidized to U^{6+}, which forms soluble complexes combined with the anions: CO_3^{2-}, SO_4^{2-} and PO^{3-} (Langmuir & Hermans, 1980). The most abundant uranium minerals are listed in Table 5.1.

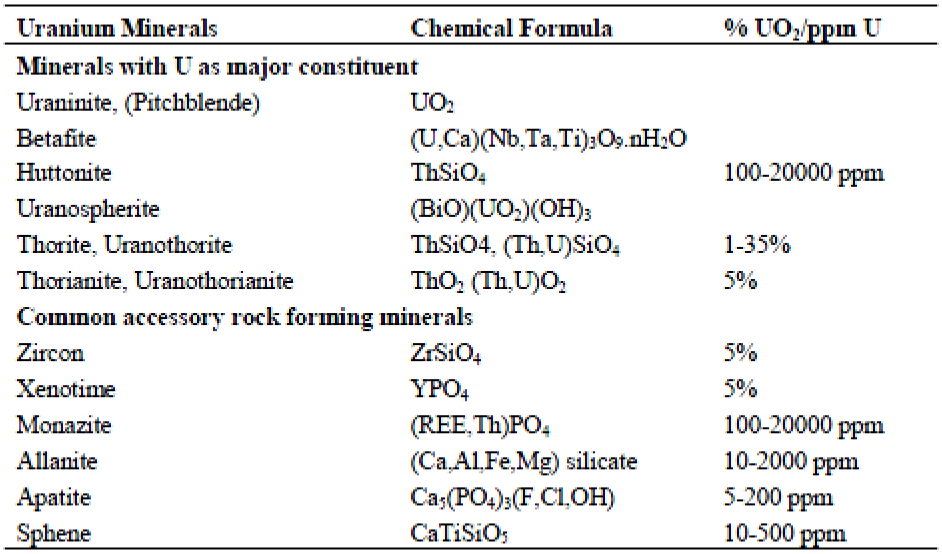

Uranium Minerals	Chemical Formula	% UO_2/ppm U
Minerals with U as major constituent		
Uraninite, (Pitchblende)	UO_2	
Betafite	$(U,Ca)(Nb,Ta,Ti)_3O_9.nH_2O$	
Huttonite	$ThSiO_4$	100-20000 ppm
Uranospherite	$(BiO)(UO_2)(OH)_3$	
Thorite, Uranothorite	ThSiO4, $(Th,U)SiO_4$	1-35%
Thorianite, Uranothorianite	ThO_2 $(Th,U)O_2$	5%
Common accessory rock forming minerals		
Zircon	$ZrSiO_4$	5%
Xenotime	YPO_4	5%
Monazite	$(REE,Th)PO_4$	100-20000 ppm
Allanite	(Ca,Al,Fe,Mg) silicate	10-2000 ppm
Apatite	$Ca_5(PO_4)_3(F,Cl,OH)$	5-200 ppm
Sphene	$CaTiSiO_5$	10-500 ppm

Table 5.1: *The most important uranium minerals (Modified from IAEA – TECDOC – 1363, 2003)*

Uraninite is common as minute inclusions in the rock forming minerals in granites or as large grains in mineralized granites and pegmatites. Uraninite also occurs in hydrothermal veins and sedimentary rocks. The accessory minerals zircon, monazite, apatite, allanite and sphene are common in igneous and metamorphic rocks, of which zircon and monazite are the most resistant to weathering. As U becomes mobile under supergene conditions, a large variety of U^{6+} minerals may form. This explains the variety of minerals found in uranium deposits, including silicates, phosphates, carbonates, sulphates, vanadates, molybdates, niobates, tantalates and titanates (Bea, 1999).

5.3 Thorium

Thorium is a chemical element with atomic number 90. Thorium is an actinide with oxidation state Th^{4+} in solution (Fig. 5.4). Thorium shows high affinity with elements such as U, Ce and Zr. Thorium can be dissolved in acid solutions and its solubility is enhanced by humic acids (Chopin, 1988). It less soluble in water where exhibits strong colloidal characteristics giving rise to hydroxyl compounds and insoluble silicates that may precipitate. Th^{4+} has strong tendency to form complex ions which combined with chloride, fluoride, nitrates, sulfates and carbonates are easily soluble. This complex ions are able to mobilize thorium under certain conditions of Eh and pH.

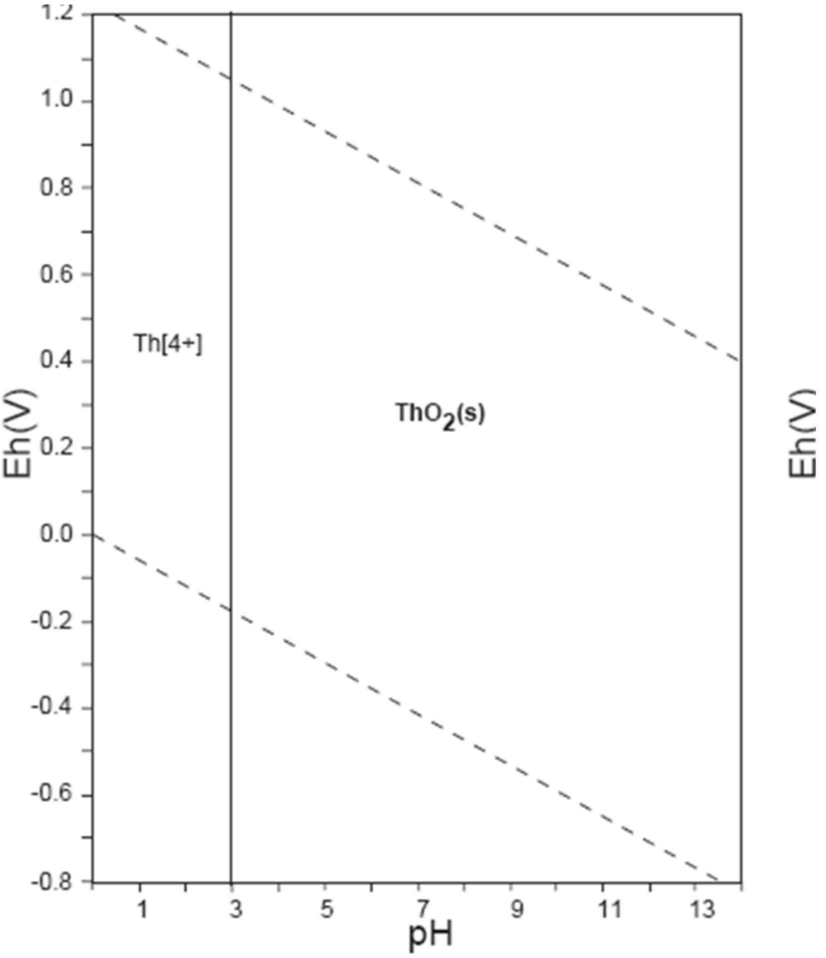

Figure 5.4: *Eh-pH diagram of the system Th-O-H at 298.15 °K and $P = 10^5$ Pa (Modified from Takeno, 2005)*

Thorium is a constituent of accessory minerals such as zircon, monazite, allanite and xenotime, apatite and sphene. Table 5.2 lists these with their average Th content, along with other minerals that have Th as a major constituent.

Thorium Minerals	**Chemical Formula**	**% ThO_2**
Minerals with Th as major constituent		
Huttonite	$ThSiO_4$	80
Thorite, Uranothorite	$ThSiO_4$, $(Th,U)SiO_4$	50, < 50
Cheralite	$(Th,Ce,Ca)(SiO_4PO_4)$	30
Thorianite, Uranothorianite	ThO_2, $(Th,U)O_2$	80, < 80
Common accessory minerals		
Monazite	$(REE,Th)PO_4$	10
Xenotime	YPO_4	0.4-1
Zircon	$ZrSiO_4$	0.01-1
Allanite	(Ca,Al,Fe,Mg) silicate	0.1-1
Apatite	$Ca_5(PO_4)_3(F,Cl,OH)$	0.001-0.1
Sphene	$CaTiSiO_5$	0.001-0.1
Epidote	$CaFe^{3+}Al_2O.OH(Si_2O_7)(Si_2O_4)$	0.005-0.05

Table 5.2: *The most important thorium minerals (Modified from IAEA – TECDOC – 1363, 2003)*

5.4 Potassium

Potassium is a lithophile element and is monovalent under natural conditions (Fig. 5.5).

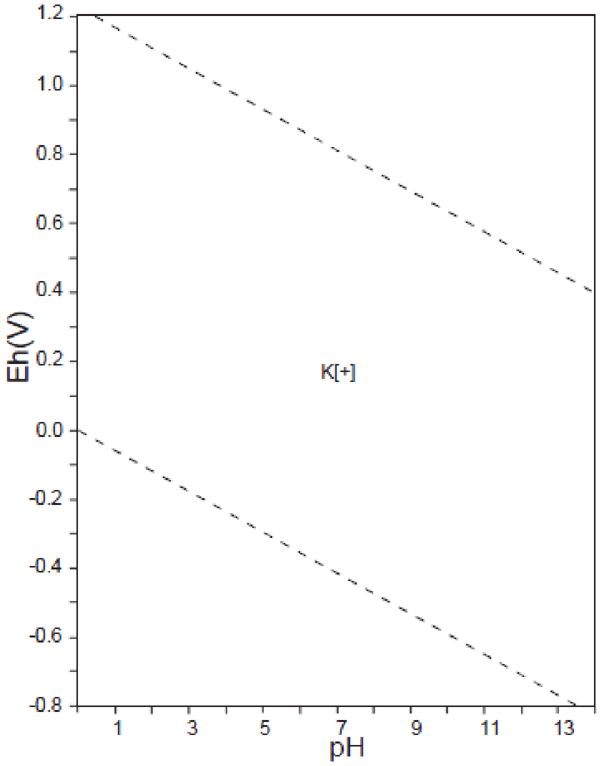

Figure 5.5: *Eh-pH diagram of the system K-O-H at 298.15 °K and P = 10^5 Pa (Modified from Takeno, 2005)*

Most K occurs in felsic rocks as alkali-feldspar. Alkaline lavas can exceed 6% of K, K in granitoids is 3,5% on average. Mafic and ultramafic rocks contain much lower concentrations, with average K content ranging from 0.58 to 0.75 %. The feldspar mineral series, the feldspathoids leucite and nepheline, and the micas biotite and muscovite, together contain virtually all the potassium in magmatic and metamorphic rocks respectively. Some amphiboles contain up to 1 % K. Table 5.3 lists the common minerals of which K is an essential constituent and some other common K-bearing minerals (Mittlefehldt, 1999).

Potassium Minerals	**Chemical Formula**	**% K**
Rock forming silicate minerals		
Feldspars	$(K,Na)AlSi_3O_8;(Na_x,Ca_{1-x})Al_2\text{-}xSi_2\text{+}xO_{8(x=0\text{-}1)}$	
Alkali-feldspar	$(K,Na)AlSi_3O_8$	13
Microcline	$KAlSi_3O_8$	13
Orthoclase	$KAlSi_3O_8$	13
Sanidine	$KAlSi_3O_8$	13
Leucite	$KAlSi_2O_6$	17
Nepheline	$(Na,K)AlSiO_4$	23
Biotite	$K(Mg,Fe)_3AlSi_3O_{10}(OH)_2$	8
Muscovite	$KAl_2AlSi_3O_{10}(OH)_2$	8
Phlogopite	$KMg_3AlSi_3O_{10}(OH)_2$	8
Hornblende	$(K,Na)_{0\text{-}1}(Na,Ca)_2(Fe,Mn,Mg,Ti,Al)_5(Si,Al)_8O_{22}(OH,F)_2$	1
Other K-minerals		
Alunite	$KAl_3(SO_4)_2(OH)_6$	
Glauconite	$(K,Ca,Na)_{<1}(Al,Fe^{3+},Fe^{2+}Mg)_2[(OH)_2/Al_{0.35}Si_{3.65}O_{10}]$	
Sylvite	KCl	

Table 5.3: *The most important potassium minerals (Modified from IAEA – TECDOC – 1363, 2003)*

Section 6: The Sardinian Variscan Crust

The Sardinia–Corsica Microplate (S-CM) exhibits one of the most complete and best-preserved transects of the southern European Variscides, and it can be divided into the following tectono-metamorphic zones: a Foreland Zone in the SW with either very low grade or no metamorphism; a Nappe Zone in the SE and central parts of the island (subdivided into external and internal nappes, with several stacked tectonic units), affected by low grade metamorphism; an Inner Zone in the north, with medium to high grade metamorphism (Figure 6.1).

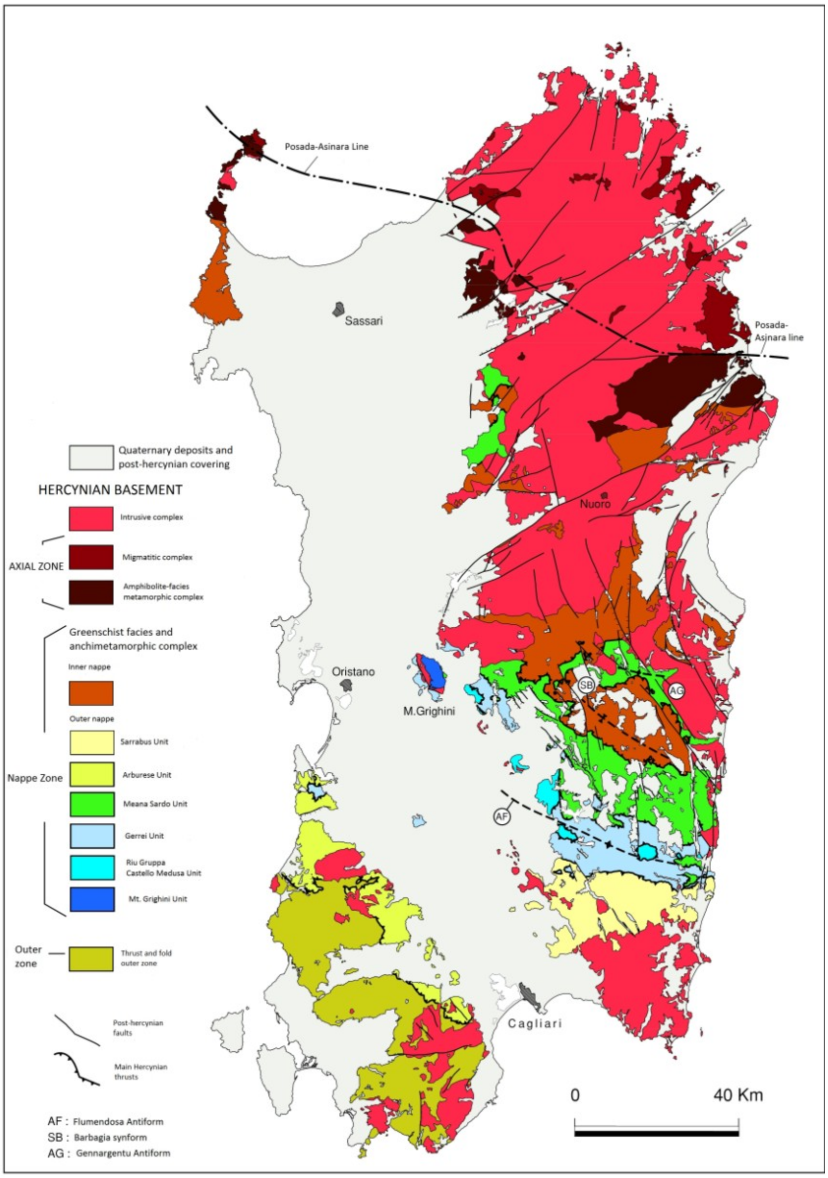

Figure 6.1: *Tectonic sketch map of the Variscan basement of Sardinia (Modified from Carmignani et al., 2001)*

The Foreland and Nappe zones are also characterised by a Middle Ordovician angular unconformity (Sardic Unconformity: Carmignani *et al*., 2001, and references therein), which is also recognised in the Eastern Iberian Plate (Casas-Sainz & de Vicente, 2009; Navidad *et al*., 2010). Along the southern boundary of the Inner zone an eclogite-beareing belt is exposed, which was supposedly considered a suture zone (Cappelli *et al*., 1992; Carmignani *et al*., 1994). The protolith of the eclogite has been dated at 457 ± 2 Ma, the high-pressure event is Devonian (Cortesogno *et al*., 2004; Giacomini *et al*., 2005; Franceschelli *et al*., 2007). Eclogites have MORB signatures, and are embedded within a metapelitic-metarenaceous complex hosting also homogeneous quartzite beds (metacherts?), orthogneisses, and metabasite with high-medium-P granulite metamorphic imprint (Franceschelli *et al*., 2007). The deformation, localized in low-strength shear zones, and the geometric association of rock bodies with different metamorphic record, point to a mélange of rocks tectonically sampled from diverse crustal levels within a channel flow, probably linked to the subduction of a lower Paleozoic ocean (Cappelli *et al*., 1992). Throughout the external nappes (Carmignani *et al*., 1994), the sedimentary record and fossil content is generally preserved, and several volcano-sedimentary complexes are stacked in the Nappe Zone (Di Pisa *et al*., 1992; Carmignani *et al*., 1994) (Figure 2). This collisional structure is well preserved after the post-collisional evolution and the emplacement of the huge Sardinia-Corsica Batholith (S-CB) (Figure 6.2). The S-CB stretch over 10.000 Km^2 and its composition is mostly monzogranitic with minor amounts of granodiorite/tonalite and 1% of gabbroic masses. Leucogranites are common and equal in volume at the granodiorites. Most authors interpreted the origin of the S-CB purely in terms of post-collisional gravitational collapse of the mountain chain (Carmignani *et al*., 1992; Ferré & Leake, 2001). A model of generalized vertical shortening account for the generation of hybrid magmas during progressive decompression. Over the past decades, it has been demonstrated that decompression-related melting played a major role during the formation of the S-CB (Rossi & Cocherie, 1991; Ferré & Leake, 2001). Crustal extension may effectively results in a pronounced thermal anomaly that have the potential for generating melts in the uppermost subcontinental mantle, and also in the felsic lower crust by self-feeding mechanisms (Ferré & Leake, 2001). Anatexis of the Variscan crust is a major event in the Corsica-Sardinia block from about 350-345 Ma (Ferrara *et al*., 1978; Giacomini *et al*., 2006). The early melts consist of trondhjemitic leucosomes that reflect focused anatexis of metasediments by muscovite dehydration melting (Cruciani *et al*., 2008). Somewhat younger leucosomes characterized by granodioritic and granitic composition testify slightly higher solidus temperatures and increased rates of melt production, however the petrologic difference between these two generation of melts is generally explained in terms of source heterogeneity rather than changing PT conditions (Cruciani *et al*., 2008; Macera *et al*., 2011).

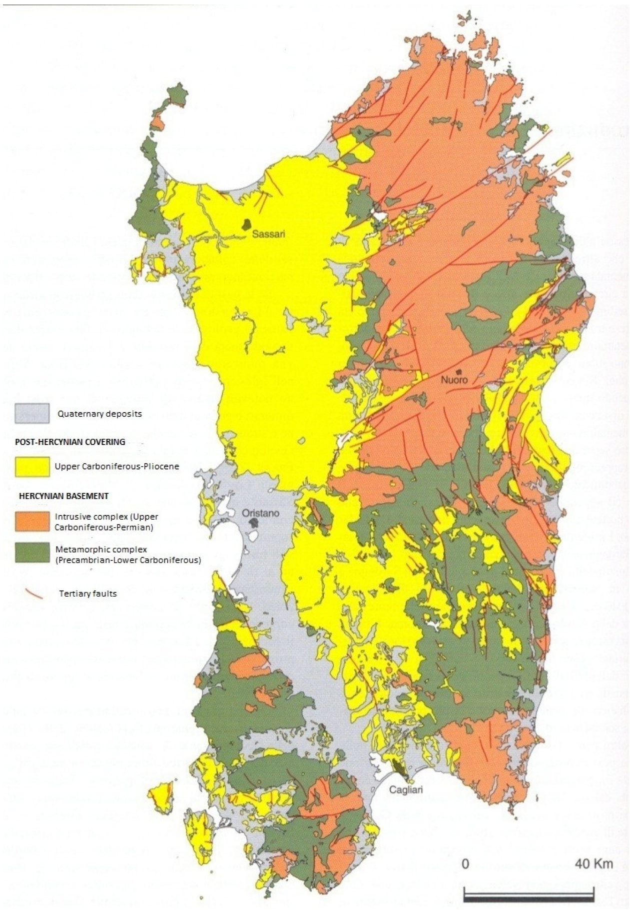

Figure 6.2: *Intrusive complexes reported with orange color (Modified from Carmignani et al., 2001)*

The majority of authors separate the late stage of regional anatexis and the growth of the C-SB assembly on the base of circumstantial field evidences, however there is no geochronological constraints supporting this interpretation. The only certain conclusion is that the growth of the batholith is mainly due to anatexis of a variscan crust with some contribute of subcrustal melts (Zorpi *et al*., 1991). Based on field relationships, U-Pb zircon ages and petrologic considerations, Rossi and Cocherie (1991) and Ferrè & Leake (2001) distinguished three main magmatic suites within the S-CB. The early magmatic sequence (U1) developed in northern Corsica around 340 Ma (Paquette *et al*., 2003) during N-S shortening. U1 melts gave rise to high-K/Mg calc-alkaline plutons that emplaced at depths ranging from mid-crustal levels (< 0.37 GPa according to Ferré & Leake, 2001) up to the surface. Between about 320-280 Ma, the composition of the granitic melts evolved to lower MgO compositions, producing the large granodioritic and monzogranitic U2 plutons, which form the largest part of the S-CB (del Moro *et al*., 1975; Ferrè & Leake, 2001; Paquette *et al*., 2003; Oggiano *et al*., 2005, 2007). Only a few studies have attempted to reconstruct the tectonic setting that brought to the emplacement of U2 plutons (Rossi & Cocherie, 1991; Gattacceca *et al*., 2004; Kruhl & Vernon, 2005). The observation that most of the U2 early melts (around 320 Ma) were emplaced within narrow emplaced within narrow strike-slip shear zones (Gébelin *et al*., 2009) suggests that they formed during the transitional phase from bulk shortening to extension. The alkaline suite U3 is the last magmatic phase in the S-CB and includes ~250 Ma post-orogenic plutons emplaced at very shallow structural levels (P < 0.2 GPa) and sub-volcanic complexes not exposed in north Sardinia (Cocherie *et al*., 2005).

Crustal features similar to that of Sardinia and Corsica occur both in France (Maure Massif, Central Massif, Pyrenees) and Spain (Coastal Catalan Chain).

The fittings with these south European regions is obvious considering that the nowadays position of the Sardinia-Corsica Block is the consequence of the Burdigalian counter-clockwise rotation of this microcontinent as consequence of the roll-back and slab retreat of the insubric slab subducted beneath the south-european margin (i.e. Sardinia Corsica crust) (Malinverno & Ryan 1986; Carmignani *et al*., 1995, Oggiano *et al*., 2009 and reference therein).

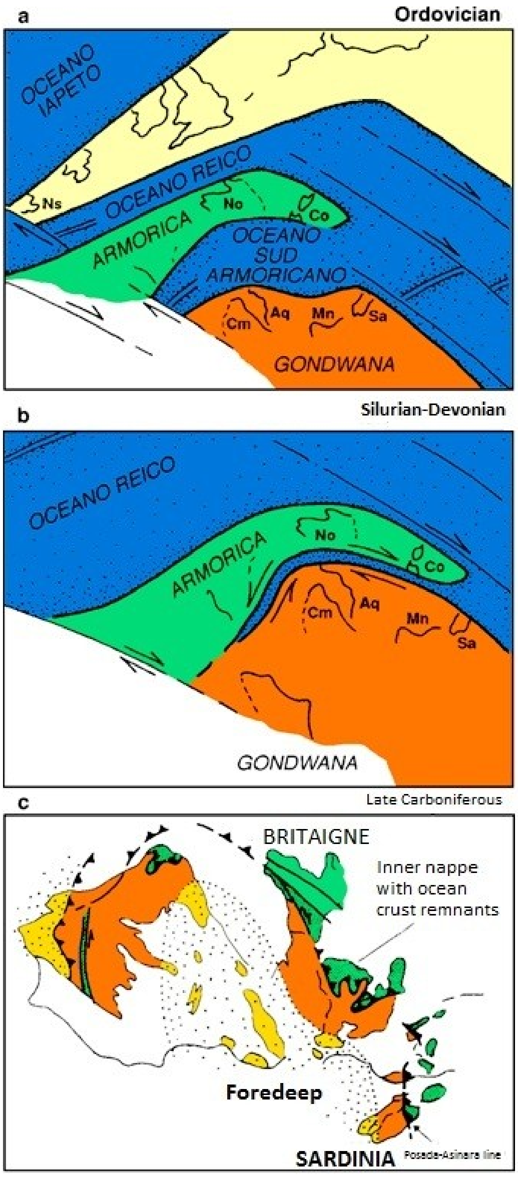

Figure 6.3: *Paleogeographic reconstruction of the Hercynian of South Europe: a) Ordovician paleogeography (Modified from Vai & Cocozza, 1986 and Paris & Robardet, 1990); b) Silurian-Devonian paleogeography; c) Late Carboniferous paleogeography (Modified from Matte, 1986 and Franke, 1989). Sa: Central and southern Sardinia; Co: Corsica and northern Sardinia; No: Normandie; Cm: Cantabrian chain; Aq: Aquitaine; Mn: Montaigne Noire; Ns: Nova Scotia.*

The age of the rifting phase is dated to Oligocene (from 30 to 24 Ma) followed by a short Early Miocene oceanic accretion (ages ranging from 23 to 15 Ma, Ferrandini *et al.*, 2000). Then the structural pre-drift directions, namely Variscan, have to be restored of ~30° with respect to the stable Europe. Pre-mesozoic geometry of the belt was an orogenic curved belt that reaches from Spain, the Massif Central. The belt have a double vergence, with a central wide range of high and medium-grade metamorphic rocks exhumed from mid-crustal layer before late Carboniferous. The N vergence continues to north of the Alps through Ardenne, up to Bohemia.

Section 7: Evaluation of Hazard

7.1 Introduction

A large part of Sardinia, approximately 6000 km^2 (Ghezzo & Orsini, 1982), consists of granitic rocks of the Sardinia-Corsica Batholith (S-CB). The S-CB is deeply related to the evolution of the south European Variscan belt (Paquette et al., 2003). The batholith emplaced in a time interval of about 60 Ma, from 340 Ma to 280 Ma. The long period of emplacement reflects important differences in terms of chemical-mineralogical composition and texture. Texture variability gives different "drawings" at these granites, a feature that makes them interesting as dimension stones for a wide variety of usages, including flooring, columns, ashlars or other architectonic elements. Therefore, the knowledge of their natural radioactivity is very important for the evaluation of the amount of public exposure.

Natural radioactivity on Earth is caused by radiation from outer space and radioactive decay of lithophile elements in the lithosphere, mainly represented by ^{226}Ra, ^{232}Th and ^{40}K. Because of peoples spend most time indoors (Stoulos *et al.*, 2003), they expose themselves to radiations in two ways: I) from gamma-radiation caused by external sources, and II) from an internal radiation due to inhalation and accumulation of radon and related its decay products in the respiratory tract. Many governmental and international organizations (UNSCEAR, European Commission, OECD etc…) have recently focused particular attention on trying to minimize the health risks associated with the exposure to these indoor radiations. Radionuclides are widely distributed in the crust and their concentration is not homogeneous. Generally, highest values are found in acid igneous rocks (Dickson & Scott, 1997) such as granite, which is a very popular building material. For this reason, we developed a portable gamma-ray spectrometer in order to allow fast and in-situ survey on the Sardinian granite outcrops. The main aim of this screening was to collect a thorough database on the natural radioactivity of Sardinian granites. Then, results were used to address both the hazard related to the natural radioactivity of the most popular granitic dimension stones exploited in Sardinia, and the geochemical variation within and amongst plutons.

7.2 Materials and methods

7.2.1 Rocks investigated

A preliminary survey on several Sardinian plutons, ranging in composition from quarz-diorites to leuco-monzogranites, allowed us to get basic constraints on the distribution of the natural radioactivity carriers within the S-CB (Fig. 2). Based on a preliminary report which gave a bunch of very high radioactivity values, we decided to analyze more in detail seven Sardinian granitoids traded worldwide as dimension stones. These rocks are known as *Rosa Beta, Ghiandone*, *Giallo San Giacomo*, *Rosa Cinzia*, *Grigio Malaga, Bianco Sardo* and *Grigio Perla* (From Fig. 7.1 to Fig. 7.7).

Rosa Beta and *Ghiandone* are the most commercialized Sardinian granites, exploited in more than 150 quarries (RAS, 2007). *Rosa Beta* is characterized by a general pink coloration due to the abundance of Kfs phenocrysts (2-3 cm); the *Ghiandone* is quite similar to *Rosa Beta*, however it shows a more apparent porphyritic texture defined by larger Kfs phenocrysts (up to 12 cm).

Giallo San Giacomo is a leuco-monzogranite, actually very appreciated. Its coloration stems from selective weathering of biotite, and oxidization of Fe-Mg minerals which gives the rock its yellowish coloration. The *Rosa Cinzia* is a monzogranite characterized by pinkish coloration and equigranular structure. This granite has finer grain than *Rosa Beta.* It exploited only in 3 quarries near the town of Tempio Pausania.

Grigio Malaga, *Grigio Perla* and *Bianco Sardo* all belong to the Buddusò pluton (Barbey et al 2008) and represent, respectively, the less, intermediate and the most differentiated portion of the pluton. The *Grigio Malaga* is a tonalitic granodiorite showing a well-foliated structure evidenced by the shape preferred orientation of the mafic enclaves and of relatively amphibole-biotite-rich domains; the *Grigio Perla* is a monzogranite characterized by a greysh coloration and, finally, the *Bianco Sardo* is a leuco-monzogranite with overall whitish coloration

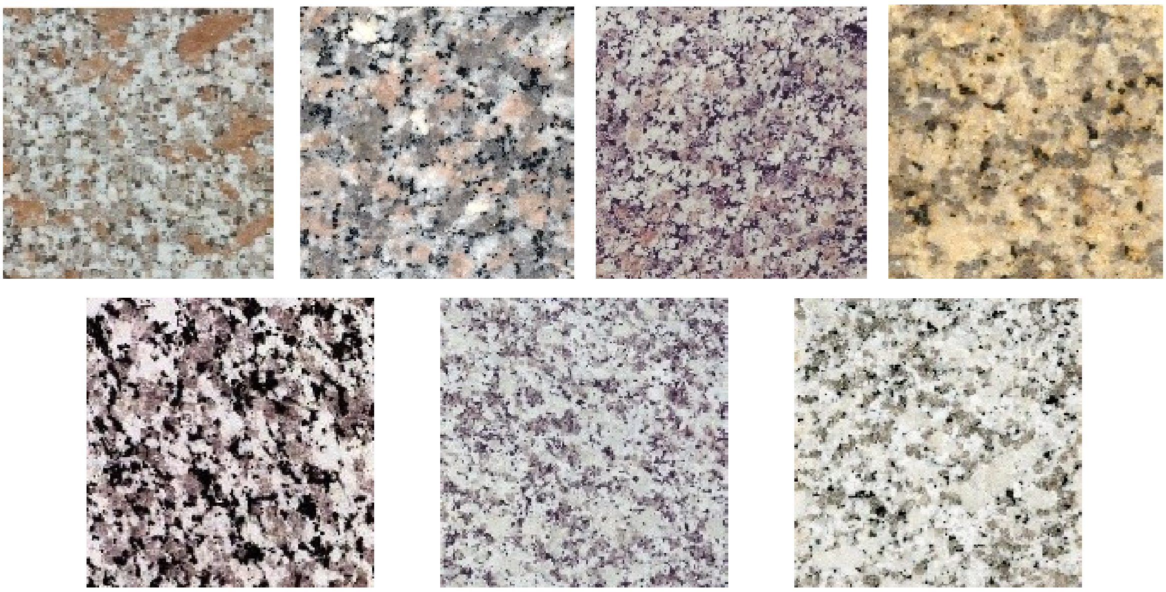

Figures 7.1, 7.2 , 7.3 and 7.4: Lithotypes exploited in Gallura region (from left to right): Ghiandone, Rosa Beta, Rosa Cinzia e San Giacomo; **Figures 7.5, 7.6 and 7.7:** Lithotypes exploited in Goceano region (from left to right): Grigio Malaga, Grigio Perla, Bianco Sardo

7.2.2 Radioactivity measurements

347 in situ radioactivity measurements were carried out through the portable gamma-ray spectrometer on several Sardinian plutons. More in details, 147 *in situ* measurements were carried out on the selected dimension stones (21 for each rock type). The accuracy and reliability of the portable gamma-ray spectrometer was controlled at each measurement site, by replicating one *in situ* analysis in laboratory with both the HPGe and ICP-MS methods.

The difference between results obtained with the portable gamma-ray spectrometer and both the HPGe and ICP-MS instruments is generally small: the discrepancy between I values calculated fromseven measurements performed by NaI(Tl) in-situ and HPGe in laboratory is less than 18,27% and less than 14,29% if we compare the measurements obtained by NaI(Tl) and ICP-MS (Tab.7.1). This small differences might reflects the usual variability observed within rocks, therefore both methods would be equally valid to characterize the natural radioactivity of granites. This small differences reflect the usual variability within the same lithotypes and it can be considered satisfactory, taking into account that the NaI(Tl) measurements are weighted on a slightly lower than 1 m^3 rocks volume whereas both HPGe and ICP-MS analyzes a spot sample .

Lithotypes	HPGe	ICP-MS	NaI	NaI vs. HPGe	NaI vs. ICP-MS
	I	I	I	%	%
Rosa Cinzia	0,89±0,02	0,86±0,004	1,02±0,01	12,75	15,69
Ghiandone	0,74±0,02	0,74±0,004	0,66±0,01	10,81	10,81
Grigio Perla	0,90±0,02	0,85±0,004	1,04±0,01	13,46	18,27
Giallo San Giacomo	0,86±0,02	0,82±0,004	0,94±0,01	8,51	12,77
Rosa Beta	0,75±0,02	0,76±0,004	0,73±0,01	2,67	4,11
Bianco Sardo	0,84±0,02	0,72±0,004	0,87±0,01	3,45	17,24
Grigio Malaga	0,60±0,02	0,71±0,004	0,70±0,01	14,29	1,41

Table 7.1: *Difference of the Activity Concentration Index (I) between portable gamma-ray spectrometer (NaI) and Lab analysis*

7.2.3 Activity Concentration Index

In granitic rocks, which are widely used as structural (ashlars, columns..) and ornamental materials (coating, tiles..), radioactivity can be evaluated through the Activity Concentration Index (I), an index proposed by UNSCEAR (1993) and European Commission (RP no. 112, 1999) that allows one to evaluate the dose rates in air from different combinations of the three radionuclides considered.

Within the European Union, the risk threshold gamma-ray dose has been established at1 mSv yr^{-1}. It is therefore recommended that controls should be based on a dose in the range 0,3-1 mSv yr^{-1}. Building materials avoid all restrictions concerning radioactivity if the annual effective dose is 0,3 mSV at the most.

According to the European Commission (RP no, 112, 1999), the I index is derived for identifying whether a dose criterion is met:

$$I = (A_{Ra}/300) + (A_{Th}/200) + (A_K/3000)$$

The I should not exceed the value reported in table 7.2, depending on the dose criterion and amount of materials used in dwelling construction.

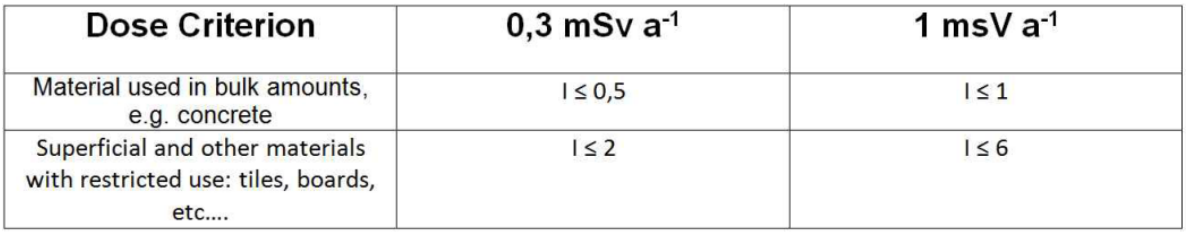

Dose Criterion	0,3 mSv a^{-1}	1 msV a^{-1}
Material used in bulk amounts, e.g. concrete	I ≤ 0,5	I ≤ 1
Superficial and other materials with restricted use: tiles, boards, etc....	I ≤ 2	I ≤ 6

Table 7.2: *Limited suggested by the European Commission for use of building materials (Modified from RP No. 112, 1999)*

7.3 Results and discussions

The preliminary survey reveals that Sardinian granites have quite a large radioactivity variability (Fig. 7.8 and fig. 7.9).

In Fig 7.8 and 7.9 we reported the total activity and the I index relative to the 347 in situ measurements carried out on several Sardinian plutons. The mean value of the total specific activity is 1512±17 Bq Kg^{-1}; the average value of I is 1±0,01.

The total specific activity ranges from 338 Bq Kg^{-1} to 2330 Bq Kg^{-1}; the I value varies from 0,22 to 2,08. 159 measurements, which represent about 45,8% of total measurements, show I values higher than 1.

Taking into account the world-wide average of ^{40}K, ^{238}U and ^{232}Th activity concentration in the earth's crust (400, 40, 40 Bq Kg^{-1} respectively (RP No.112, 1999)), we can say that 343, 204 and 329 measures exceed these values, respectively.

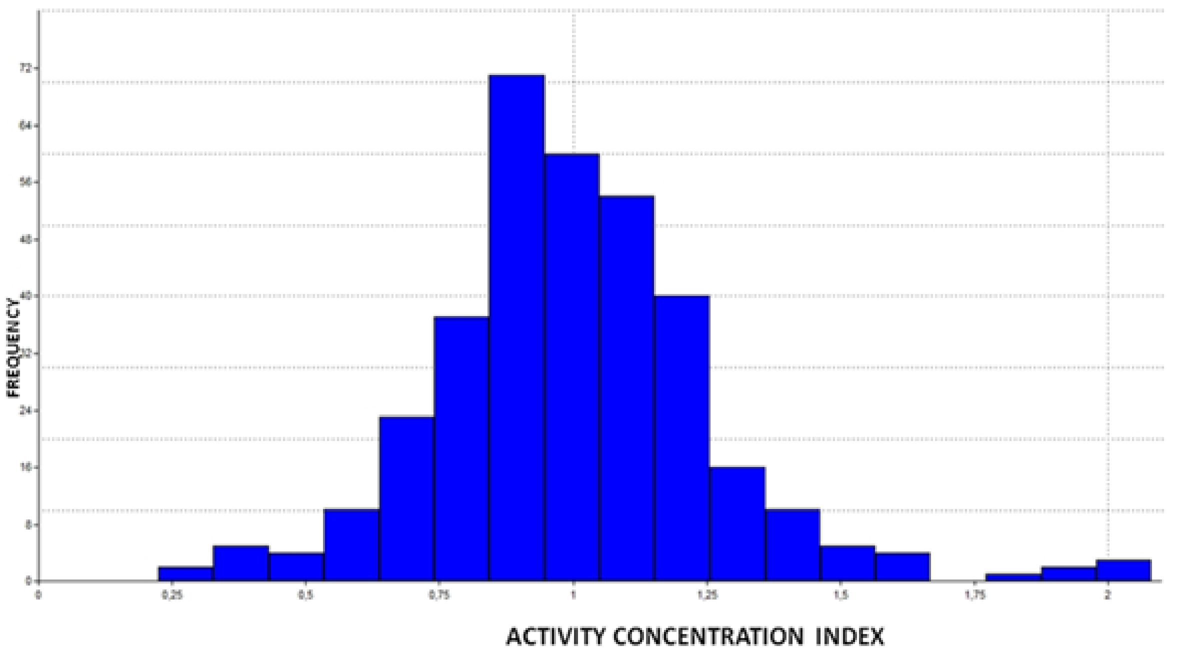

Figure 7.8: *Activity Concentration Index histogram of the 347 in-situ measurements*

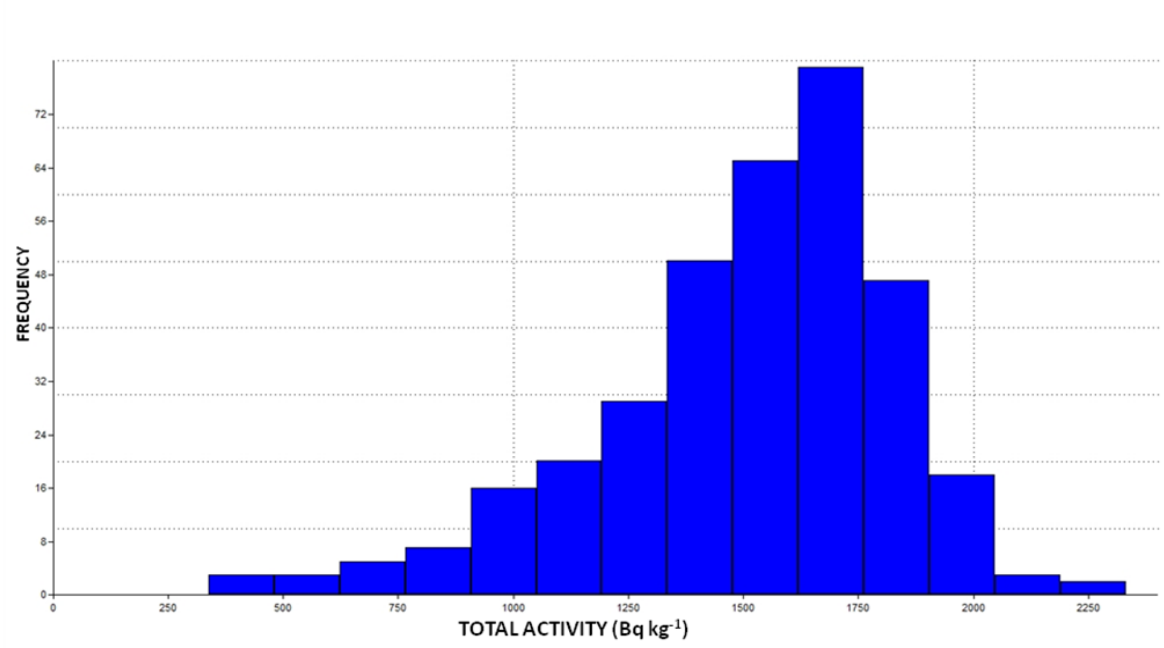

Figure 7.9: *Total Activity (expressed in Bq kg^{-1}) histogram of the 347 in-situ measurements*

These data highlighted that almost half of the sampled localities exceed the threshold value recommended in the European Union; this makes indispensable a survey of radioactivity before using these rocks as building materials. A detailed characterization of the seven selected dimension stones, taken as representative of presently traded materials, is reported in Table 7.3.

Lithotypes	**Measures**	**K (%)**	**eU (ppm)**	**eTh (ppm)**	**Activity ^{40}K (Bq Kg^{-1})**	**Activity ^{238}U (Bq Kg^{-1})**	**Activity ^{232}Th (Bq Kg^{-1})**	**Total Activity (Bq Kg^{-1})**
Rosa Beta	21	4,29±0,45	3,08±0,54	14,38±1,49	1344±141	40±7	58±6	1439±151
Ghiandone	21	4,08±0,7	4,37±1,02	18,05±2,62	1278±219	54±13	73±11	1391±233
G. San Giacomo	21	5,05±0,47	3,49±1,61	17,28±2,3	1582±147	43±20	70±9	1686±151
Rosa Cinzia	21	4,89±0,26	3,66±0,77	18,83±0,89	1533±80	45±9	76±4	1653±82
Grigio Malaga	21	3,17±0,46	2,02±0,46	15,76±1,25	1000±152	25±7	63±5	1081±157
Grigio Perla	21	4,63±0,61	2,46±0,46	16,17±1,12	1450±191	30±6	66±5	1541±195
Bianco Sardo	21	4,79±0,25	3,15±0,59	14,01±1,95	1487±92	39±7	57±8	1581±94

Table 7.3: *In this table are listed the average values, weighted with their instrumental uncertainty, with respective standard deviations of the abundance, the activity concentration of K, eU and eTh for 7 litotypes and the total specific activity.*

The ^{238}U average concentration range from 2,02±0,46 ppm (*Grigio Malaga*) to 4,37±1,02 ppm (*Ghiandone*), whereas the ^{238}U average specific activity range from 25±7 Bq Kg^{-1} (*Grigio Malaga*) to 54±13 Bq Kg^{-1} (*Ghiandone*).

The average value of ^{232}Th concentration have been found to lie between 14,01±1,95 ppm and 18,83±0,89 ppm in the *Bianco Sardo* and *Rosa Cinzia*, respectively. The ^{232}Th average specific activity vary from 57±8 Bq Kg^{-1} (*Bianco Sardo)* to 76±4 Bq Kg^{-1} (*Rosa Cinzia)*.

The ^{40}K average concentration vary from 3,17±0,46% (*Grigio Malaga)* to 5,05±0,47% (*Giallo San Giacomo)* and the ^{40}K mean specific activity vary from 1000±152 Bq Kg^{-1} (*Grigio Malaga)* to 1582±147 Bq Kg^{-1} (*Bianco Sardo)*.

These data show that all the lithotypes exceed the world reference for ^{40}K and ^{232}Th activity concentration values, whereas about the ^{238}U activities, only *Grigio Malaga*, *Grigio Perla* and *Bianco Sardo* show values lower than 40 Bq Kg^{-1}.

The calculated I values varies from 0,73±0,07 in *Grigio Malaga* to 1,04±0,05 in *Rosa Cinzia* (Fig. 1). Only the Rosa Cinzia and Giallo San Giacomo granites exceed the limit imposed for building materials. Their utilization as ornamental stones, say in manufactures requiring a limited volume of material, is instead allowed because the I-value don't exceed the limit of 6.

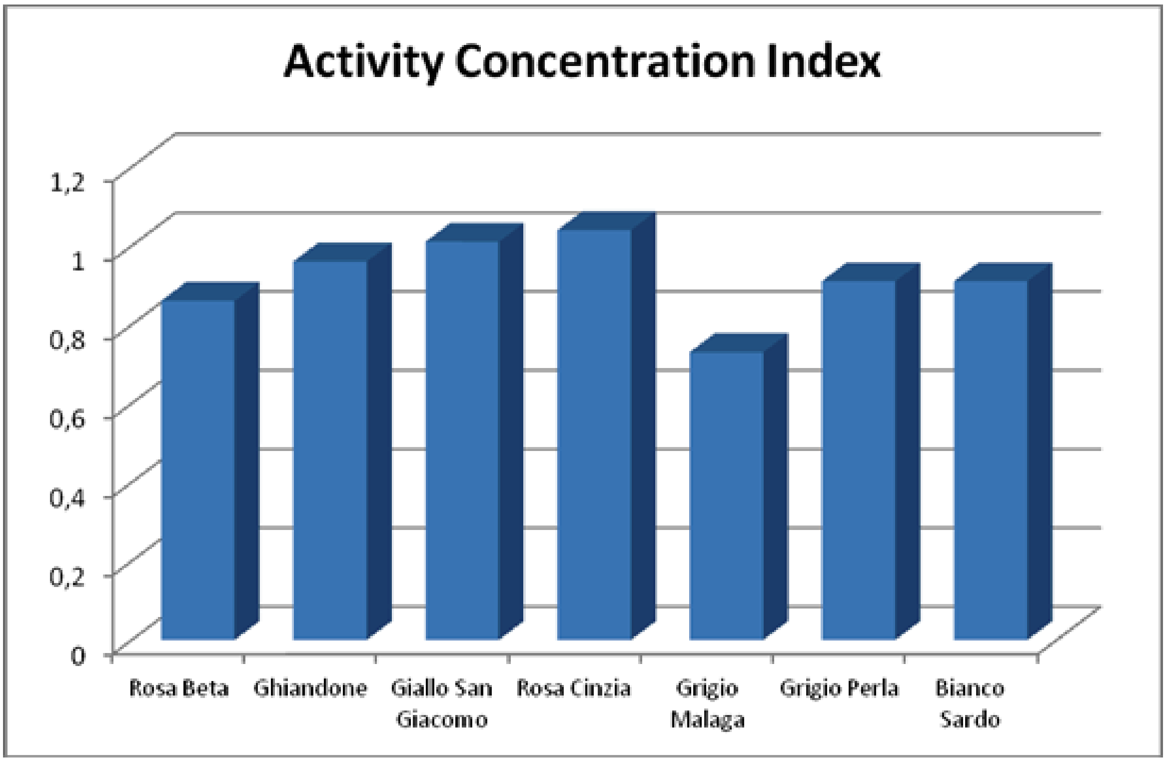

Figure 7.10: *Activity Concentration Index (I) in granite lithotypes considered*

7.4 Conclusions

This work highlighted that Sardinian dimension stones show a large variability in terms of concentration of radioactive elements. This makes indispensable some *a priori* evaluation of their total activity before proceeding with exploitation and trading. Based on the activity threshold indicated by the European guidelines in fact, more than 45% of the plutons investigated must be considered unsuitable for use in large amount including structural component (e.g. concrete, masonries) and, thus, may represent a serious problem for health.

The dimension stones analyzed in this work (most of which are still currently exploited) have almost always a I below the recommended limits, making these granites suitable as superficial materials; only the *Rosa Cinzia* and *Giallo San Giacomo* granites can't be used as structural elements (concrete, masonries, etc…) because their value is slightly above the limit fixed by the European Commission.

The portable gamma-ray spectrometer has proven to be an ideal tool for expeditious in situ measurements, allowing to get large amount of data nearly in real time. Furthermore, the portable device analyzes a larger amount of rock respect to the laboratory instruments, therefore the analyses made directly on the field are expected to be statistically sound. Another non-trivial advantage of the portable instrument is its relatively low cost. The portable spectrometer highlights a good reliability and the possibility to detect even small different of concentrations of radioisotopes in different lithologies. Comparison among portable gamma ray spectrometer and laboratory analyses (HPGe and ICP-MS) shows slight differences that can be attributed to the different amount of material analyzed which, being more in the in-situ measurement, provide us a measure weighted on a much larger volume of rock.

In conclusion we can say that the portable gamma-ray spectrometer is a powerful tool for evaluating the possibility of exploitation of new quarries and in general a useful device to perform low-cost, fast and accurate radioactivity surveys on granitic rocks.

Section 8: Employment of portable gamma-ray spectrometer in survey and mapping of intrusive complexes

8.1 Previous approach and cartographic evolution in Sardinia

Over the past 50 years the S-CB has been investigated using different approaches. The first attempts to characterize the S-CB have been made during the sixties (Simboli, 1962; Conti, 1966) by the means of a purely petrographic approach. In these early works, the S-CB was distinguished into :

- Basic masses;
- Tonalites and granodiorites;
- Monzogranites;
- Leucomonzogranites;

without paying attention to the parental relationships between magmatic pulses and plutonic complexes. Only in the eighties some researcher tried to distinguish between different plutons based on a rough timing of intrusion (mainly Rb-Sr whole rock methods) relative to the Variscan tectonics. This approach lead Ghezzo & Orsini (1982) to distinguish syn-, late- and post-tectonic granites, implicitly referring to the main Variscan collisional phase.

Finally, starting from the early nineties, the S-CB was re-considered in terms of coalescent plutons and studied by the means of a combined structural and petrologic approach (Cherchi & Musumeci, 1992).

The evolution of cartographic databases basically follows from the research approach established at the time of mapping. In many areas only 1:100000 scale maps are available, which were constructed following a petrographic approach. Obviously, as we can see in Figure 8.1, the vast majority of granites is represented with a single color, as the leading part of the S-CB consists of monzogranites. These maps are practically useless.

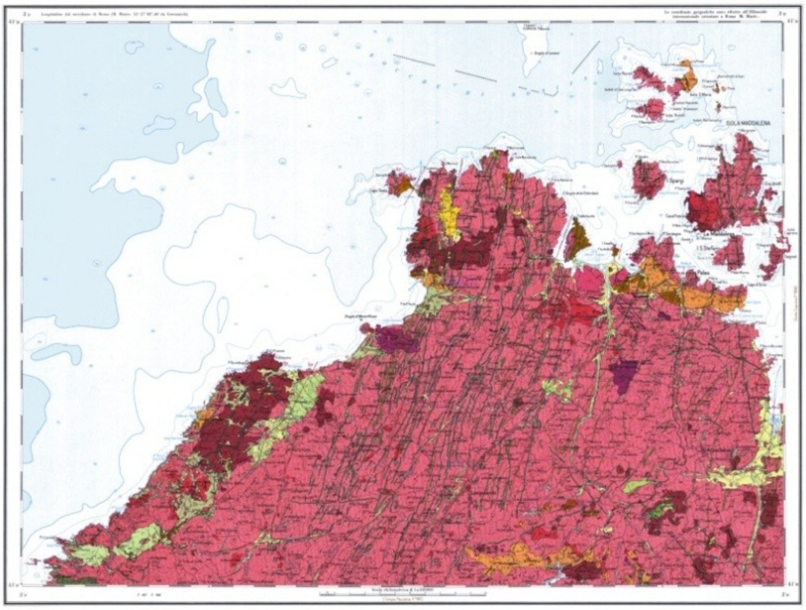

Figure 8.1: *A map 1:100000 scale.This map was made with a purely petrographic approach*

Only in 2005 the first CARG project map 1:50000 scale on the Sardinian batholith (Fig. 8.2, *Arzachena Map*) was published. This map represents a significant step forward compared to previous maps. Indeed, granitoid rocks were first mapped based on the concept of being part of a specified pluton, which is distinguishable from other plutons. Unfortunately, the 1:50000 scale maps are still very few, therefore many areas of the S-CB remains uncovered with such detail.

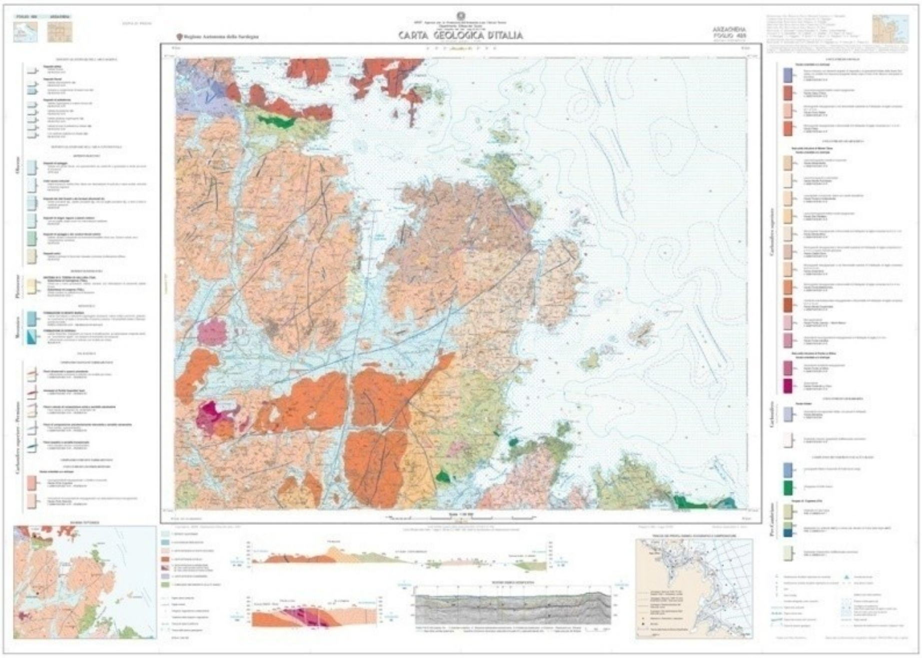

Figure 8.2: *Arzachena map 1:50000 scale*

8.2 Shortages in survey of intrusive complexes

Structural analysis is a prerequisite to survey granitic complexes. Such analysis can be made by the means of several methods, including:

- **Study of magmatic anisotropies (Magmatic flow) patterns**: As we can see in Figure 8.3, magmatic flow allow us to rebuild plutons geometry.

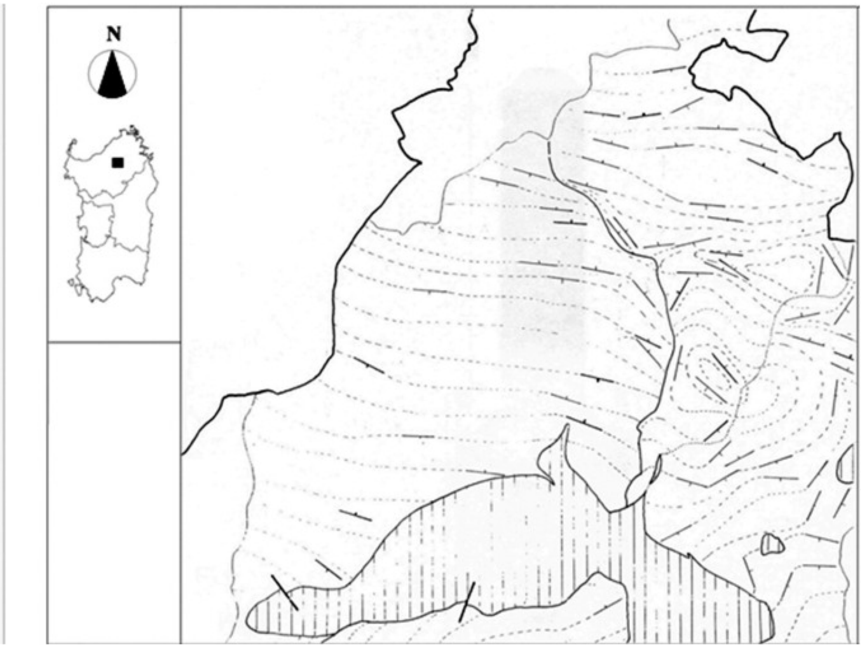

Figure 8.3: *Magmatic flow map*

Figure 8.4: *Orange line trace the development of magmatic flow in this outcrop*

- **Behavior of contacts:** Contacts between two magmatic rocks are classified as ductile contact (fig 8.5) if they bridge two rock-types while parental melts were hot, and sharp contact (“chilled margin” or “magmatic breccia”, fig 8.6 and fig. 8.7), meaning a contact that separates a cold rock from hotter ones.

Figure 8.5: *Example of “hot contact”*

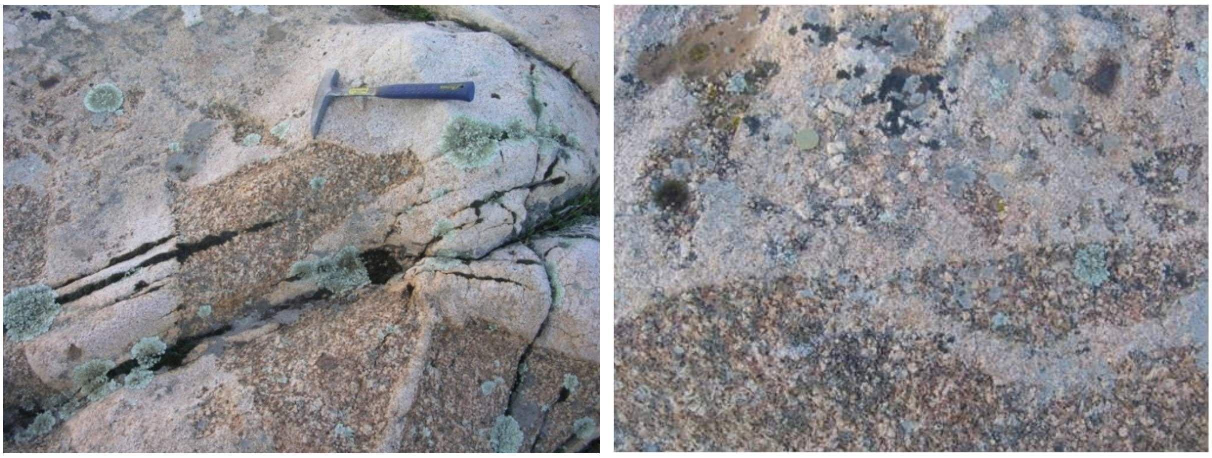

Figures 8.6 and 8.7: *Example of “magmatic breccia” (sx.) and “chilled margin” (dx.)*

.

A thorough structural analysis can be easily done where outcrops are large and contacts are exposed. Unfortunately, these conditions are not the rule. Compositionally similar terms of different plutons may be misinterpreted based on field evidences alone.

So if the field data are ambiguous laboratory analysis such as radiometric dating and chemical analysis are unavoidable. These analysis are certainly helpful but require high costs in terms of money and time.

8.3 Geological setting

8.3.1 The Buddusò Pluton and surrounding intrusions

The Buddusò Pluton belongs to the so-called U_2 high-K calc-alkaline plutonic association (about 305-290 Ma, Barbey et al., 2008), and consists of tonalites, granodiorites, monzogranites and leuco-monzogranites.

The internal structure of the pluton consists of three concentric shells that show a normal magmatic differentiation from tonalitic-granodioritic facies in the external shell to monzogranitic and leuco-monzogranitic facies in the core. Three magmatic units have been distinguished on the basis of petrography and fabric (Fig. 8.8):

- **The Outer unit:** It consist of banded, medium- to coarse-grained, porphyritic biotite/hornblende granodiorites and tonalites (Ou1), and of porphyritic biotite monzogranites (Ou2);
- **The Middle unit:** It is a layered, medium-grained, porphyritic biotite monzogranite. Bruneton & Orsini (1977) distinguish two subunits based on the amount of biotite, which is lower in the internal subunit (Mu2) than in the internal one (Mu1);
- **The Inner unit:** It consist of homogeneous, coarse-grained, leucocratic monzogranites (Iu).

The Buddusò Pluton has relatively small size (about 70 km^2) and is surrounded by several intrusions (Concas, Sos Canales, Benetutti, Monte Lerno and Tepilora plutons, which range in composition from tonalitic-granodiorites to leuco-monzogranites).

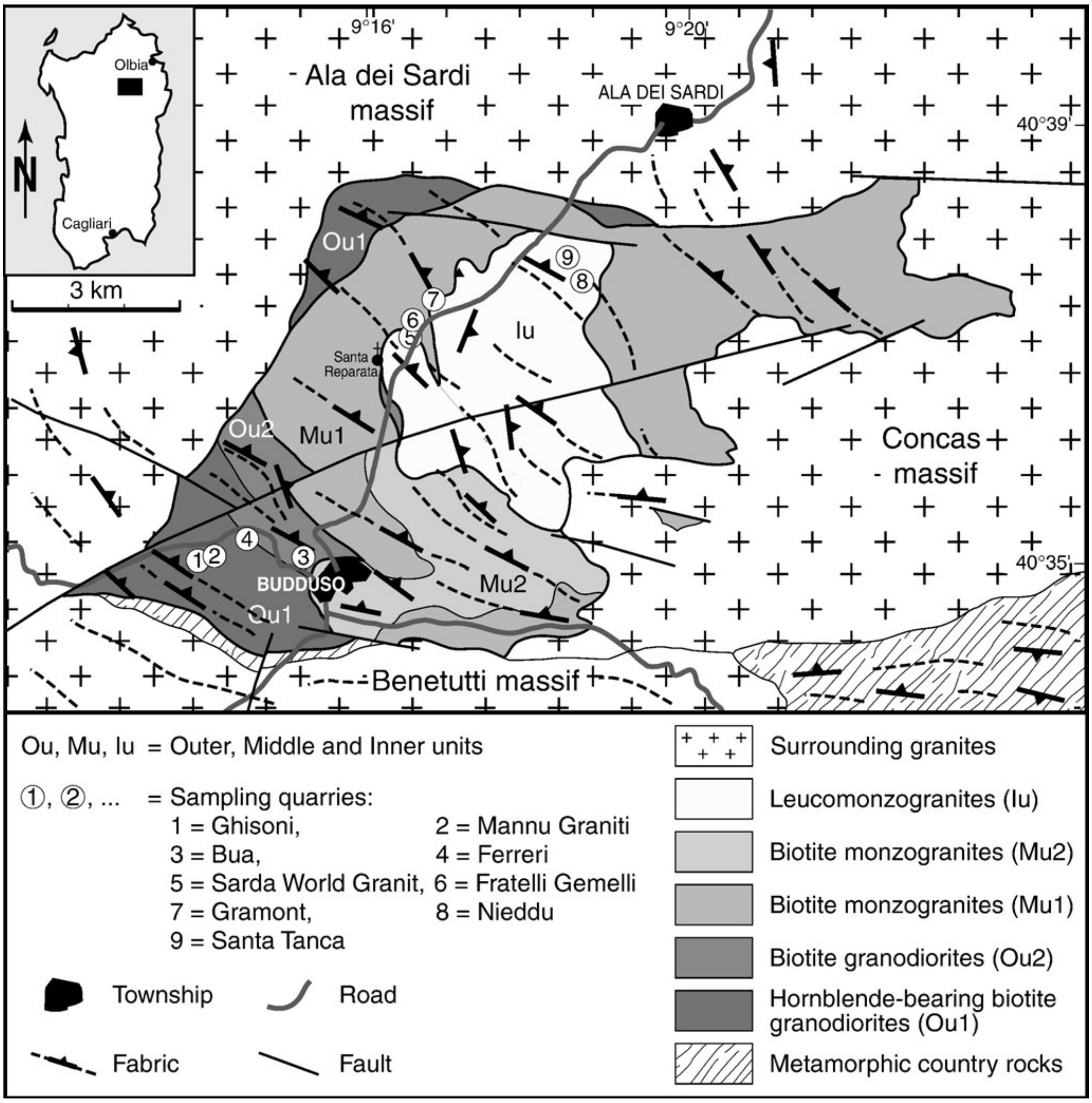

Figure 8.8: *Geologic map of the Buddusò Pluton (Modified from Barbey et al., 2008)*

8.3.2 The Arzachena Pluton and its neighbour intrusions

Arzachena (AZN) pluton (311+6/-4 Ma, Oggiano *et al.,* 2005) belongs to the high-K calc-alkaline magmatic association. The pluton is an elliptical, sill-shaped, intrusion elongated about SSE (Oggiano *et al.*, 2005). The pluton show an inverse magmatic differentiation from the external shell with prevailing leuco-monzogranites, to the core made up of granodiorites. AZN consists of three distinct shells organized into a concentric structure:

- **Granodiorite (Inner Unit):** It is the most mafic term of the intrusion and it is a medium-grained, slightly porphyritic, hornblende/biotite-granodiorite exposed along the southern margin of the pluton and inner part;

- **Porphyritic biotite-monzogranite (Middle Unit):** It represents the principal rock type of the AZN. It consists of strongly porphyritic biotite-monzogranite which grades internally to a slightly more differentiated megachrystic biotite/muscovite monzogranite.
- **Leuco-monzogranite (Outer Unit):** It consist of fine-grained leuco-granites (biotite < 5 wt.%) and represent the more evolved magmatic products.

The Arzachena pluton is one of the major calc-alkaline intrusive unit of the S-CB. Its surrounding intrusions are: Barrabisa Pluton (Granodiorite), Maddalena Pluton (Monzogranite) and other intrusive complexes such as S. Antonio di Gallura (Gabbro to Leucomonzogranite) and Aglientu (Monzogranite) complexes.

8.4 Results and discussion

8.4.1 The Buddusò pluton and its surrounding intrusion

63 measurements with the portable gamma-ray spectrometer were carried out on the Buddusò pluton (21 for each magmatic unit). All measurements were acquired *in-situ* and then plotted on eTh vs. K, eTh vs. eU and eU vs. K graphs (Fig. 8.9, 8.10 and 8.11). Taking into account these values, we noted that:

- The distribution of radioactive elements is not homogeneous, but mimic almost perfectly the petrologic zonation of the pluton there is a direct correlation from tonalites to leucomonzogranites and K and eU abundance. The eTh abundance instead has an opposite behavior, in fact it increases from tonalites to monzogranites, and decreases again from monzogranite to leucomonzogranites;
- measurements taken close to the contacts between different facies of the intrusion show transitional values, reinforcing the hypothesis that the distribution of radioactive elements is controlled by petrologic processes.

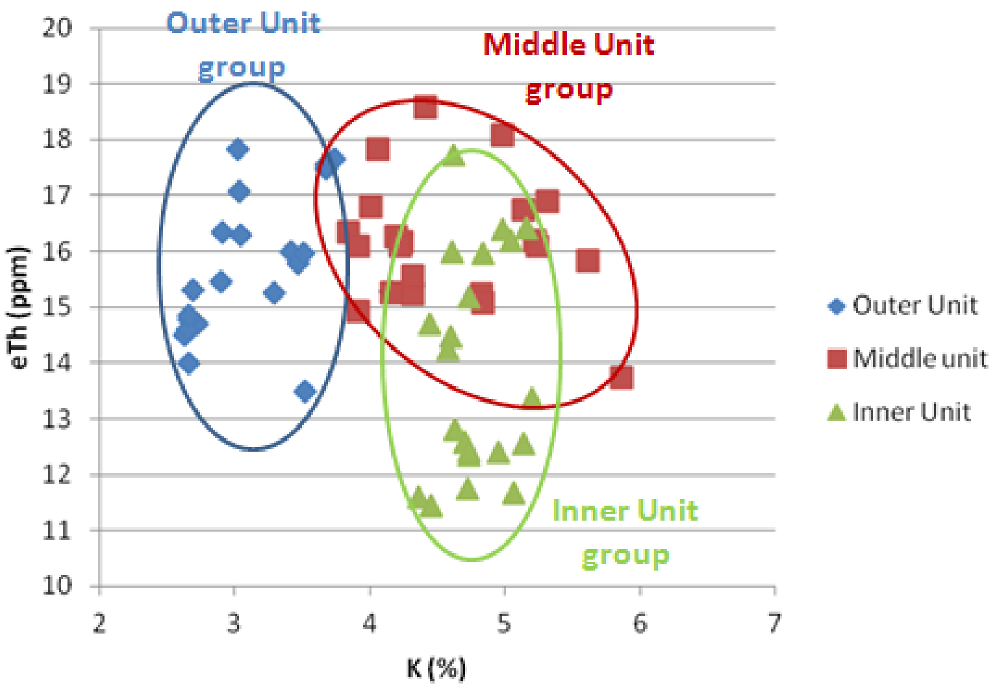
Outer Unit
group
Middle Unit
group
Inner Unit
group
eTh (ppm)
K (%)
20
19
18
17
16
15
14
13
12
11
10
2
3
4
5
6
7
◆ Outer Unit
■ Middle unit
▲ Inner Unit

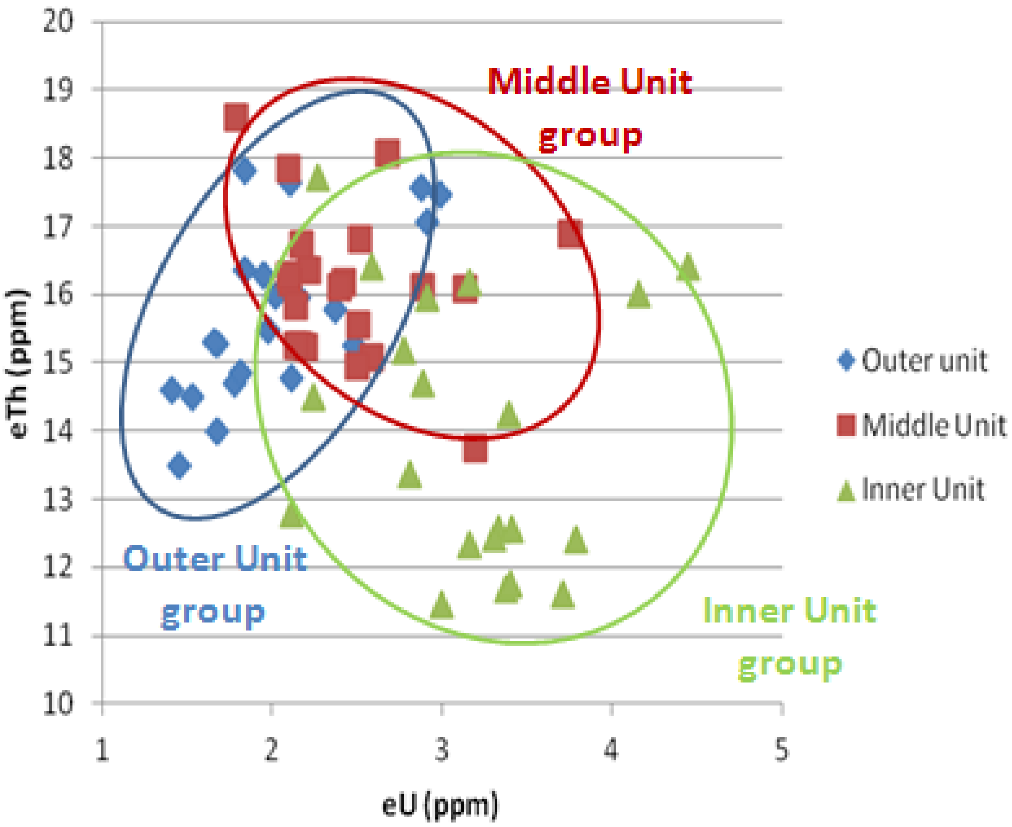
Middle Unit
group
Outer Unit
group
Inner Unit
group
eTh (ppm)
eU (ppm)
20
19
18
17
16
15
14
13
12
11
10
1
2
3
4
5
◆ Outer unit
■ Middle Unit
▲ Inner Unit

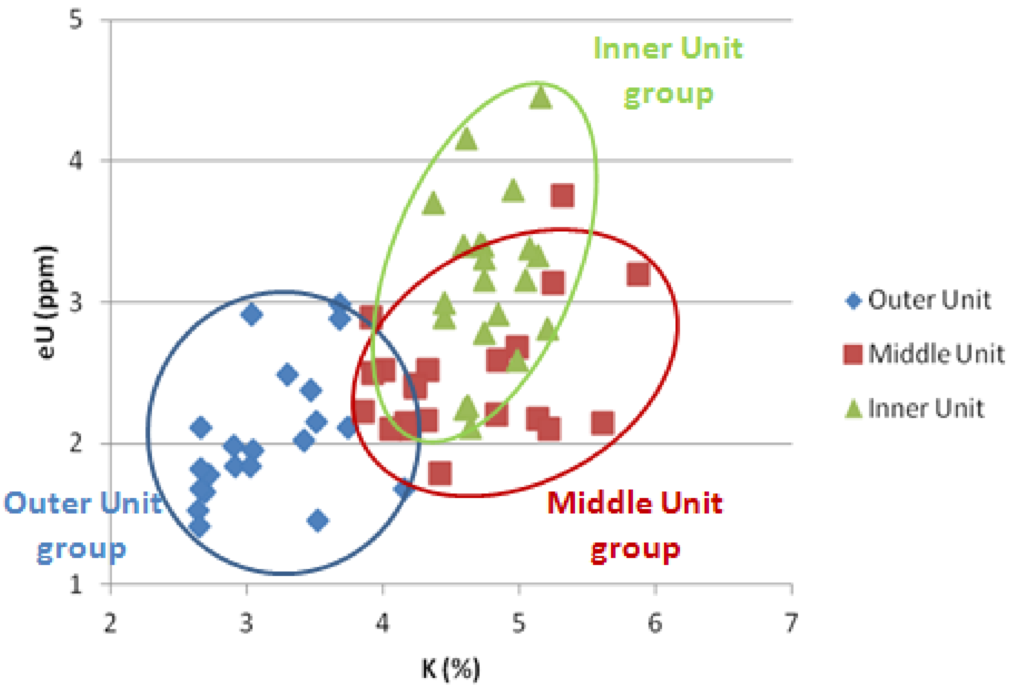

Figures 8.9, 8.10 and 8.11: *eTh vs. K, eTh vs. eU and eU vs. K graphs of the Buddusò Pluton.*

After analyzing cogenetic facies (belonging to the same pluton) of Buddusò intrusive complex, we compared these measurements with those of surrounding intrusions. The granodiorites and tonalites of the Pattada intrusive unit are very similar to and seems continuous with the Budduso intrusion; these show meaningful difference in terms of K/U and, particularly, K/Th ratios (Fig. 8.12, 8.13, 8.14). As for the monzogranites and the leuco-monzogranites, striking differences arise between the different terms of Buddusò and their petrographic equivalent in P.ta Tepilora, M.te Lerno, Concas and Benetutti granites which supposedly belong to different intrusive complexes.

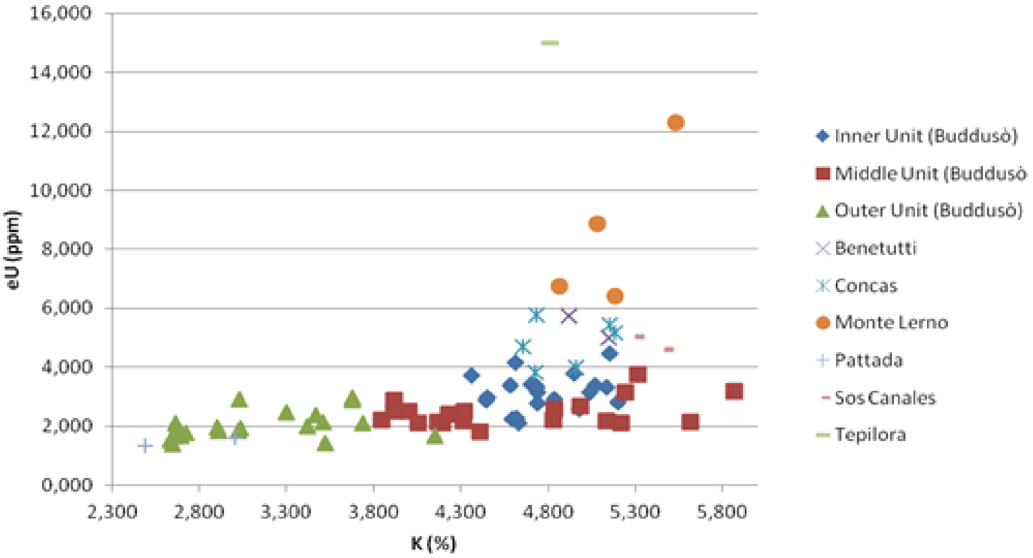

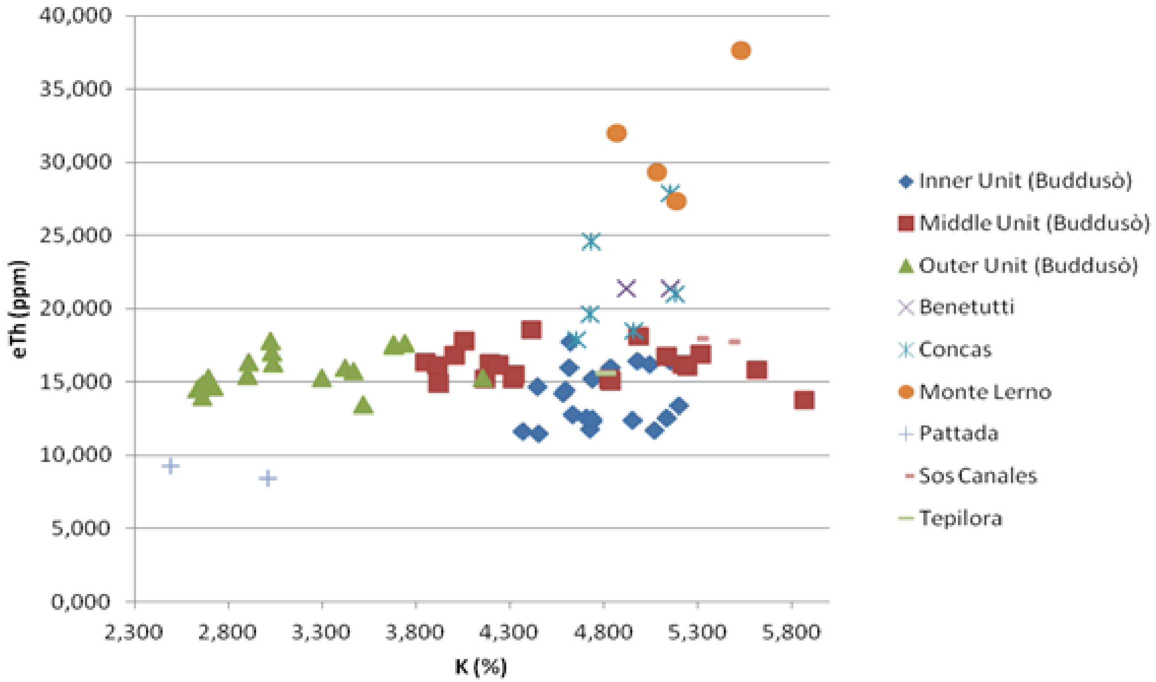

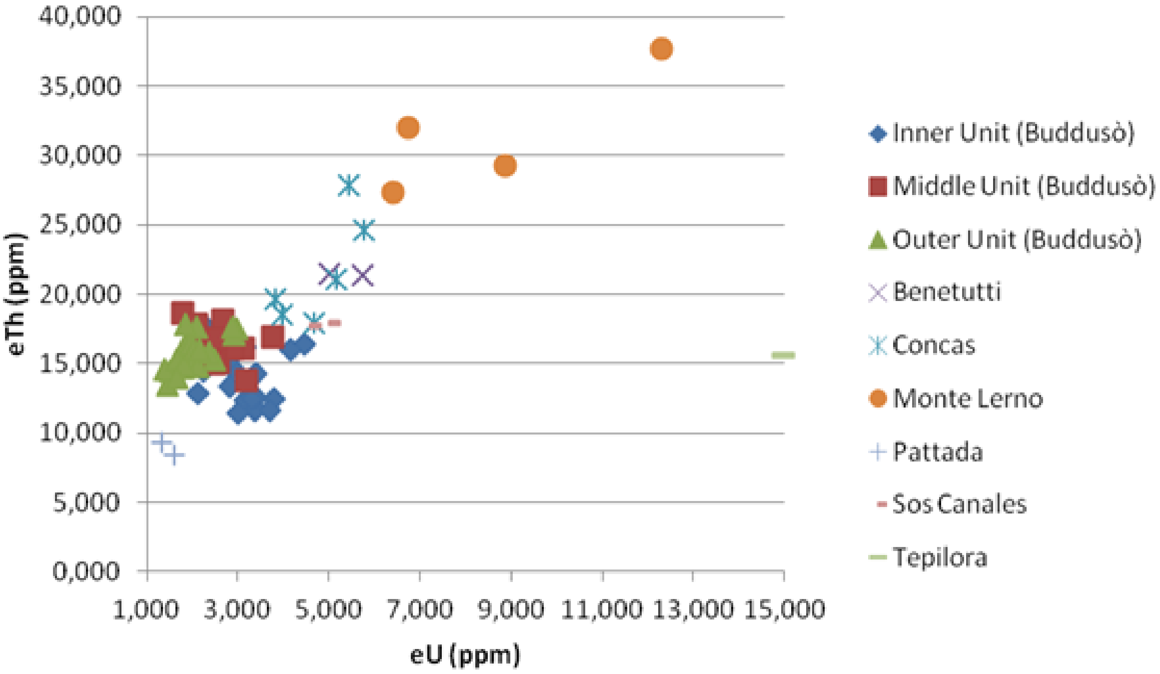

Figures 8.12, 8.13 and 8.14: *eU vs. K, eTh vs. K and eTh vs. eU graphs of the Buddusò Pluton and its neighbour intrusion*

8.4.2 The Arzachena Pluton and its adjacent intrusion

79 measurement were carried out on the Arzachena pluton (11, 31 and 37 for granodiorite, monzogranite and leucomonzogranite respectively). As for the Buddusò pluton, all acquired in-situ measurements were plotted as eTh vs. K, eTh vs. eU and eU vs. K graphs (Fig. 8.15, 8.16 and 8.17).

These results highlighted that:

- The pluton is internally heterogeneous and subdivided into three distinguishable terms, namely Granodiorite, Monzogranite and Leuco-monzogranite;
- The abundance of K, eTh and eU is directly correlated with increasing acidity of the pluton terms, except San Giacomo facies (leuco-monzogranite);
- Two different groups of leuco-monzogranite correspond to the different magmatic terms of AZN pluton: San Giacomo Facies (Cuccuru, 2009) and San Pantaleo facies (Oggiano *et al.*, 2005) with low and high abundances of eU respectively;
- The measurements taken close to the contacts between different facies of the intrusion show transitional values.

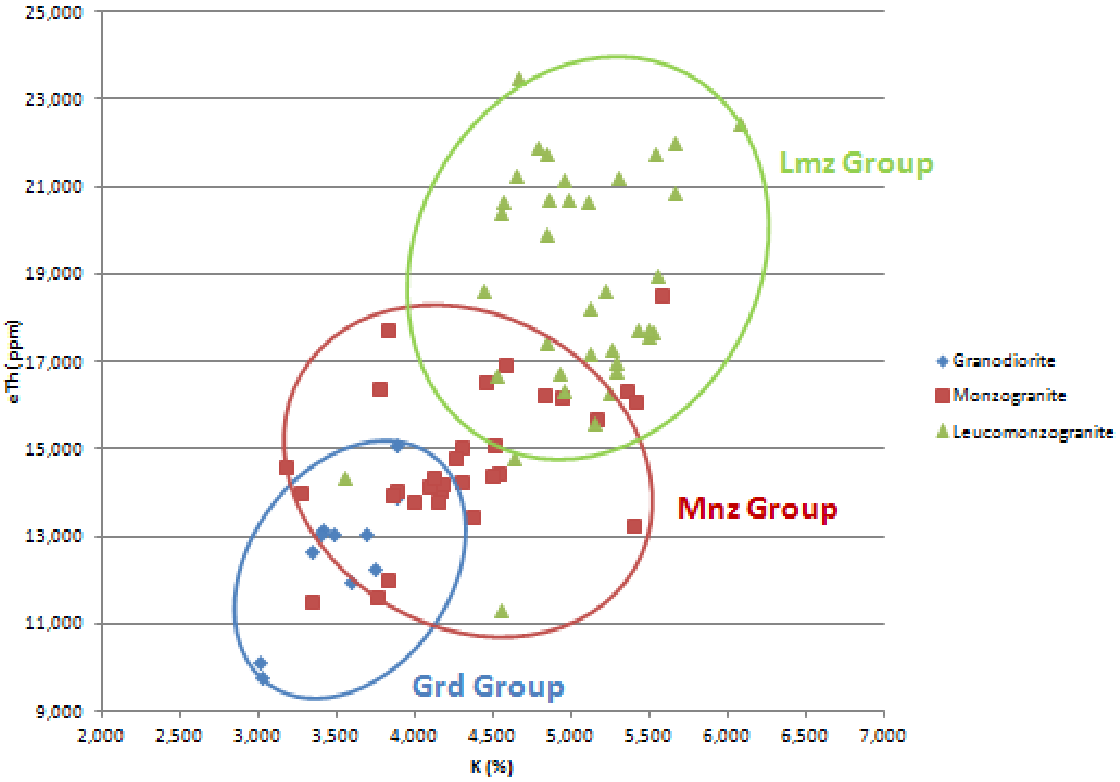

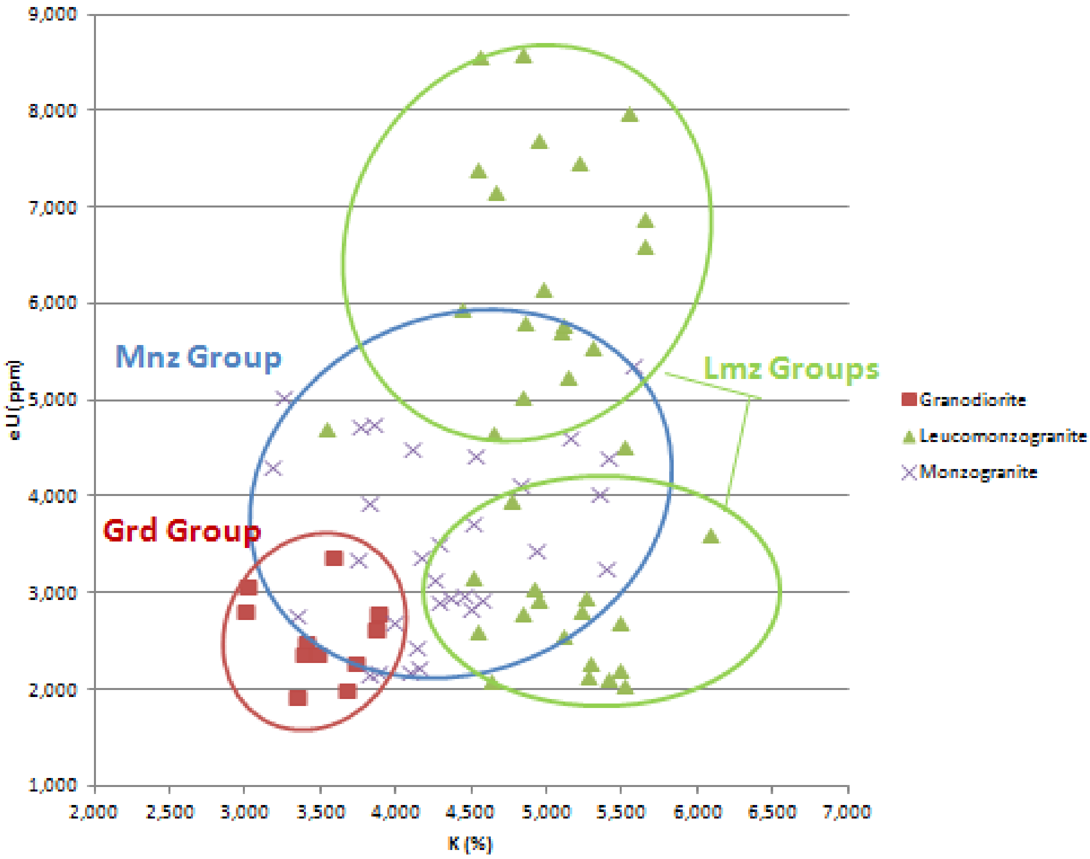

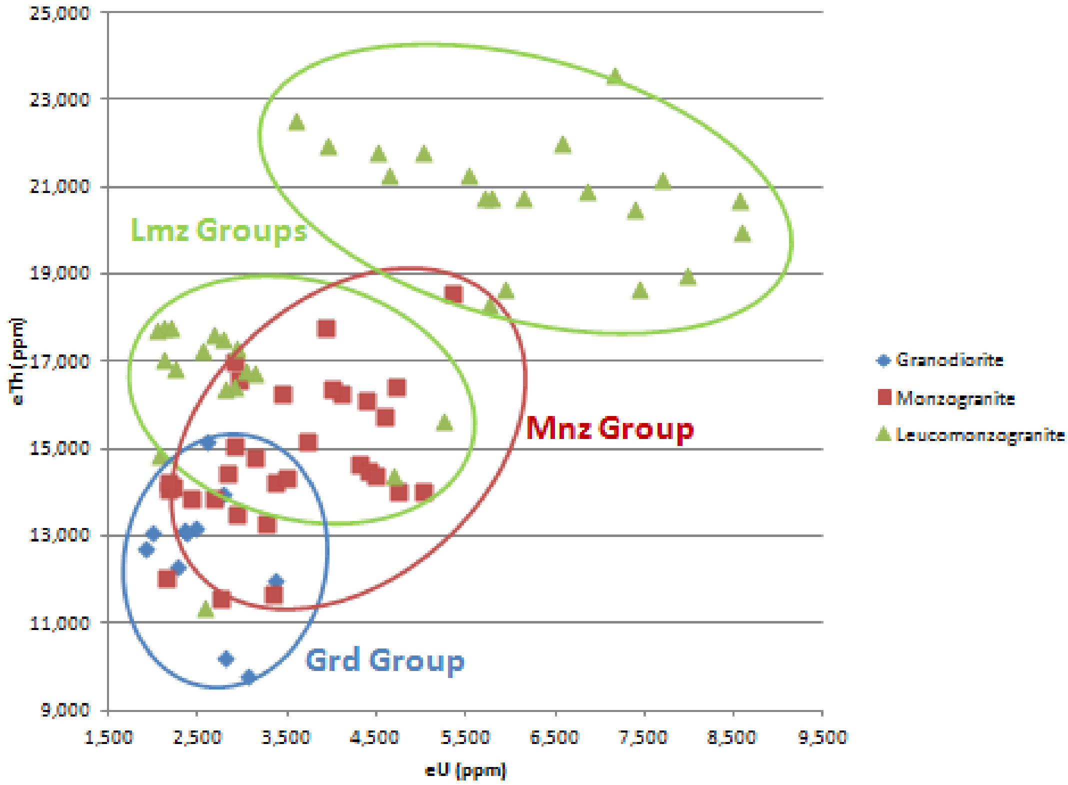

Figure 8.15, 8.16 and 8.17: *eTh vs. K, eU vs. K and eTh vs. eU graphs of the Arzachena pluton*

Figure 8.18 shows a comparison between the granodiorites of Arzachena and Barrabisa: we can see that the two group of rocks have important differences in terms of eTh/eU. Based on the eTh/eU ratio, these quite similar rocks can be easily divided into two distinct group (Fig. 8.18). This means that these granites are different, probably, belong to two different intrusive complexes.

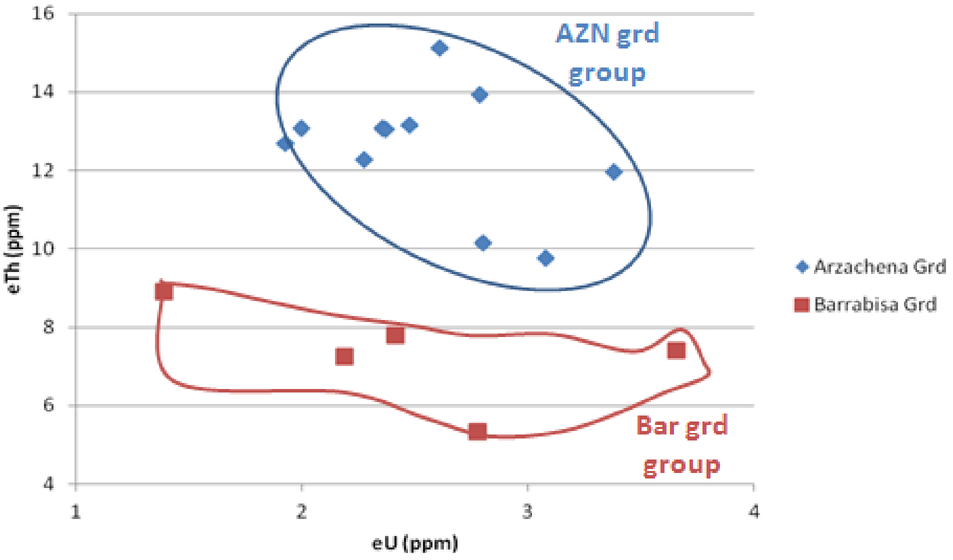

Figure 8.18: *Comparison between Arzachena granodiorites and Barrabisa granodiorites*

The Arzachena monzogranites (mnz) show very important differences in terms of eU/eTh relative to their neighboring rocks (Pulchiana belongs to Sant'Antonio intrusive complex), although all look very similar. We interpret this discrepancy as an effect of coalescence between different, possibly unrelated, intrusive complexes.

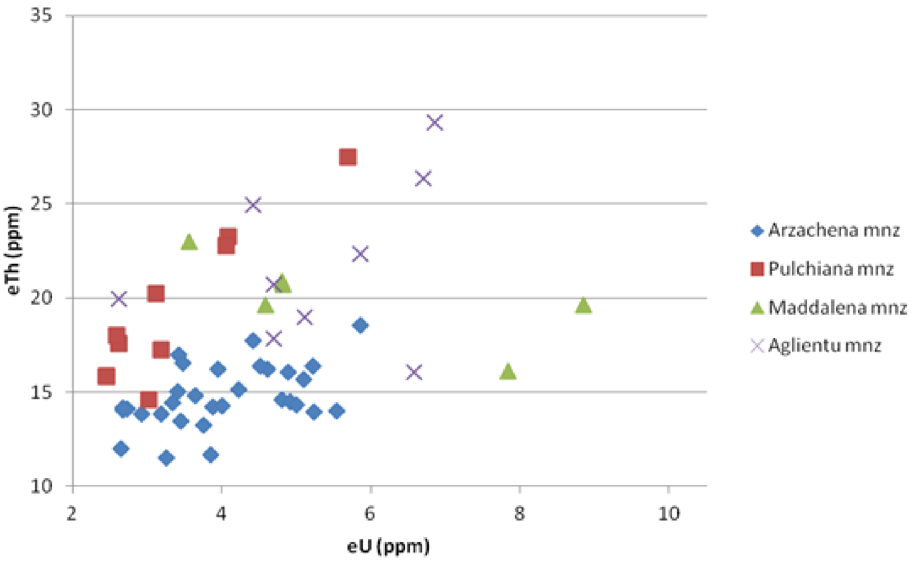

Figure 8.19: *Comparison between the Arzachena monzogranites (mnz) and its neighbour monzogranites (Aglientu, Maddalena, Pulchiana)*

Finally, we have compared the Arzachena leuco-monzogranites (lmz) with the Monte Pinu (belongs to Sant'Antonio plutons) leuco-monzogranites (lmz). Figure 8.20 shows that these two groups of leuco-monzogranites can be distinguished quite well. Then, as for other magmatic facies, we interpreted the two leuco-monzogranites as equivalent part of different plutons.

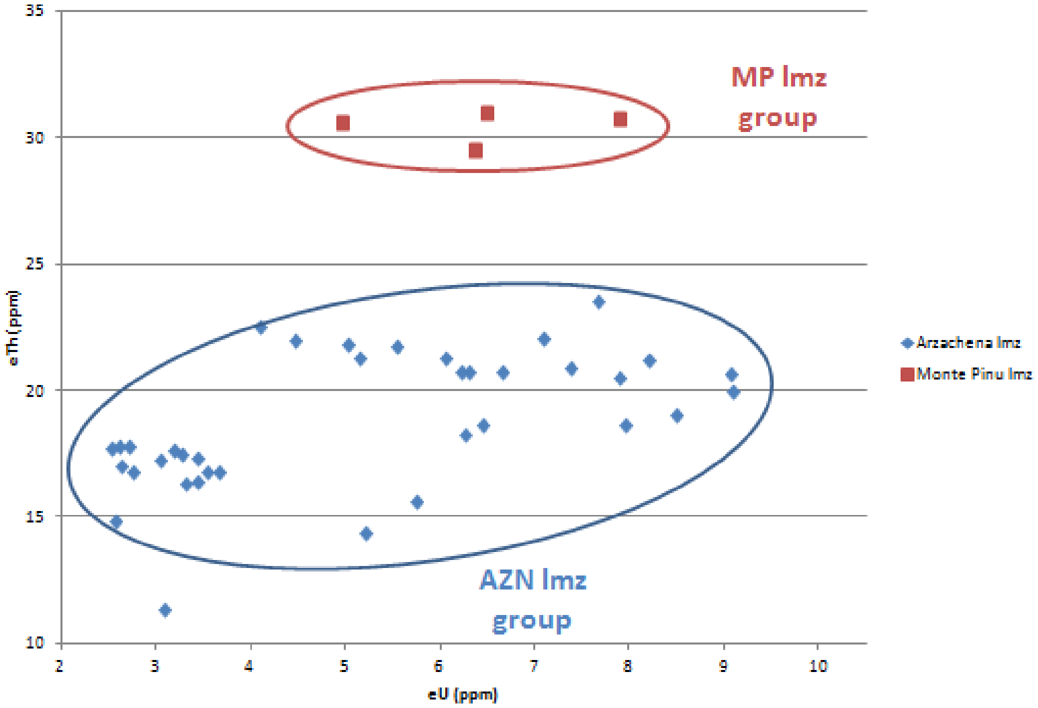

Figure 8.20: *Comparison between Arzachena and Monte Pinu leucomonzogranites (lmz)*

8.5 Conclusions

These results show that K, eU and eTh concentration in cogenetic facies (namely, to different rocks that belong to the same pluton) with different composition are generally different, whereas similar facies show similar values. On the other hand, granitoids of similar composition belonging to different plutons may show different K, eU and eTh concentrations, although this may be an ambiguous feature. This work demonstrated that the portable spectrometer may be an ideal tool for doing near real time geochemical analysis of granitoids, helping field-work.. In conclusion, this trial seems to encourage the employment of portable gamma-ray spectrometer for survey and mapping of the intrusive complexes. Indeed, in Appendix B, we have attached the geologic map of the Sardinian batholith that we renewed, and that we are completing, with the crucial help of the portable gamma-ray spectrometer.

Section 9: Thermal budget of the European Variscides

9.1 Introduction

The Variscan Belt (Fig. 9.1) is quoted as a reference example for hot collisional orogens where shallow gradients outstripping 30-40°K/km pave the way for the development of diagnostic sillimanite – andalusite - cordierite assemblages and anatexis at upper-crustal levels (Schulmann *et al.*, 2008). Hot geotherms were diffusely established around the Carboniferous-Permian boundary, ca. 300 Ma, after a period of crustal thickening characterized by much lower gradients. Three main sources would have contributed to the thermal budget: heat flowing out from the mantle, radiogenic heat production, and viscous shear heating (Burg & Gerya, 2005). Mantle is inferred to be the main contributor in the French Massif Central (Ledru *et al.*, 2001; Gébelin *et al.*, 2009; Faure *et al.*, 2010), Bohemian Massif (Janoušek & Holub, 2007; Klein *et al.*, 2008), and Iberian zone (Pin *et al.*, 2008; Martínez-Catalán *et al.*, 2009). In all these areas, a mechanism of slab break-off or thermal erosion is generally invoked to explain the strong attenuation of geotherms. However, Lexa *et al.* (2011) challenged this view demonstrating that temperature in excess of 900°C were reached in the lower crust of the Bohemian Massif because of radioactive decay. In this model there is no reason to assume an increment of heat flux across the Moho, whereas HT-metamorphism is a consequence of melt-induced rheological adjustments of thick orogenic roots. Shear heating was generally considered insignificant and never computed in previous works. Here we focus on the thermal budget of the Variscan crust by comparing one-dimensional numerical models with a literature database (Fig. 9.1) on PT conditions recorded at ca. 350 Ma and ca. 300 Ma. Most petrologic data at ca. 350 Ma, age of Barrowian-type metamorphism (Bellot & Roig, 2007; Giacomini *et al.*, 2008; Skrzypek *et al.*, 2011), can be well reproduced by a purely conductive geotherm, assuming realistic values of Moho heat flow. Subsequent attenuation of the thermal structure requires instead upward advection of heat by melts. These results are discussed in terms of different end-members tectonic models.

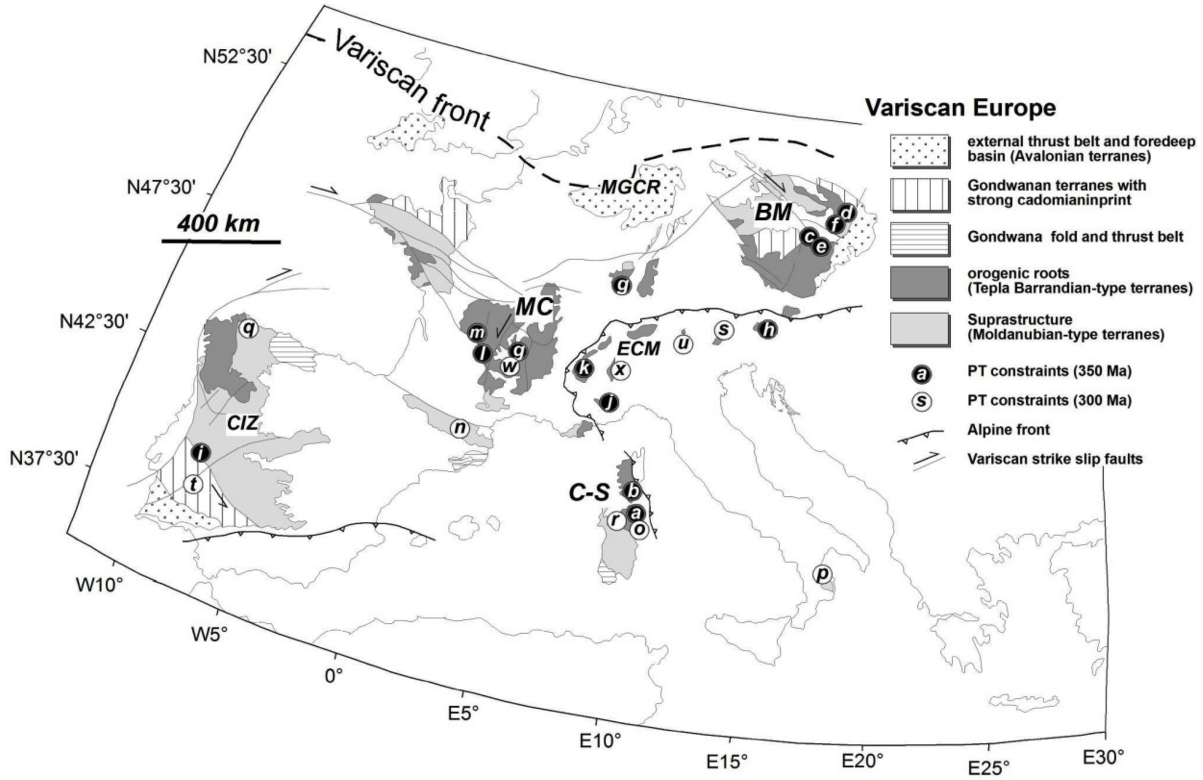

Figure 9.1: *The Variscan Europe. a = Giacomini et al. (2008); b = Giacomini et al. (2005); c = Kotkova et al. (1996); d = Stipska et al. (2004); e = Medaris et al. (1995); f = Szrypek et al. (2011); g = Pin & Vielzeuf (1983), Costa et al. (1993); h = Becker (1997), Cook et al. (2000); i = Pereira et al. (2010); j = Rubatto et al. (2010); k = Guillot & Menot (1999); l = Duguet et al. (2007); m = Bellot & Roig (2007); n = Vilà et al. (2007); o = Cruciani et al. (2008); p = Langone et al. (2010); q = Reche et al. (1998); r = Casini et al. (2010); s = Braga & Massonne (2008); t = Villaseca et al. (1999), Fernandez-Suarez et al. (2006); u = Braga et al. (2001); w = Ledru et al. (2001); x = Vavra et al. (1999).*

9.2 Numerical modeling

Unpredictability of thermal conductivity, Moho heat flow and, to some extent, crustal composition, makes two opposite approaches to numerical modeling equally valid: (1) deterministic, and (2) stochastic. Both strategies have several shortcomings that depends on the statistical accuracy of experimental inputs in the first case, and on the physical pertinence of the relevant variability functions in the latter.

Our simple numerical code uses an hybrid deterministic-stochastic method to solve the heat conduction equation expressed in the form:

$$T = T_0 + (Q_0 + L\Sigma_H)z/k - \Sigma_H z^2/2k. \quad (1)$$

Where T_0 is the surface temperature [K], Q_0 is the heat flowing out from the mantle [mW m^{-2}], k is thermal conductivity [W m^{-1}K^{-1}], z is depth [km], L is the thickness of the conductive layer [km], and Σ_H is a term that account for the heat produced in the crust [μW m^{-3}] as $\Sigma_H = (H_r+H_s)$, where H_r indicates radioactive heat production rate, and H_s is a term that accounts for viscous shear dissipation in the crust according to Burg & Gerya (2005). Thermal diffusivity (κ) and specific heat capacity of rocks (c_p) are related to k as $k = \kappa\rho c_p$. Both κ and c_p variables are not linear in T at constant pressure (Whittington *et al.*, 2009), so the code calculate iteratively the value of thermal conductivity by correcting an input value (k_0), arbitrarily taken as 3 ± 0.5 W m^{-1}K^{-1}, for temperature changes.

The models assume a stratified crust composed of sedimentary lid, metamorphic or granitic middle crust, and essentially granulitic lower crust (Table DR2). The composition and thickness of layers was determined from geologic constraints and geophysical data sets (Banka *et al.*, 2002; Finetti, 2005; Guy *et al.*, 2011; Palomeras *et al.*, 2011). Details of experimental parameters are given in Fig. 2. The database (Table 9.1 and 9.2) on heat-producing elements composition of the Moldanubian zone was compiled by adding 405 new data collected in the C-S massif to 215 measures, mainly granulites and sedimentary rocks, taken from the literature. Assuming compositional homogeneity, that is different rock types were smoothly distributed within the layers, average H_r is simply estimated by weighting rock type compositions to their relative abundance at the relevant times. Given a present-day crustal thickness of ≈ 40 km, of which ≈ 20 km of granulitic lower crust (i.e., Guy *et al.*, 2011), the sedimentary lid is drawn from the thickness of Carboniferous basins (Pochat & Van den Driessche, 2011). Assuming that melts for late Carboniferous batholiths were sourced in the lower crust (Orejana *et al.*, 2011; Lexa *et al.*, 2011), the middle crust at ca. 350 Ma and ca. 300 Ma is sized to balance the volume of post 350 Ma melts. Although this configuration would represent an oversimplification of the Variscan geometry, we choose to keep our models as simple as possible to emphasize the interaction between the heat potential of the crust and the variation of Q_0, which is a first-order approximation of mantle dynamics (Jaupart & Mareschal, 2007).

Lithotype	Measures number	Mean U (ppm)	Mean Th (ppm)	Mean K (%)	Mean A (μW m^{-3})	Composition (%)	Gross volumetric heat production (μW m^{-3})
Upper Crust							
Pelite[*,†]	22	12.1 ± 21.5	14.4 ± 4.2	2.9 ± 1.4	3.9 ± 5.1	0.678	
Sandstone[*, †]	14	7.6 ± 5.2	13.7 ± 4.7	2.3 ± 1.9	2.8 ± 1.2	0.322	
Total Upper Crust							3.54 ± 0.78
Middle Crust							
Metasediment[*, †]	48	3.4 ± 1	15.1 ± 4.1	3.4 ± 1.4	2.3 ± 0.5	0.175	
Metavolcanic[*, †, §]	53	7.8 ± 4.6	11.8 ± 4.5	5 ± 1.4	3.4 ± 1.3	0.113	
Metatexite[*, #]	36	2.6 ± 1.7	9.1 ± 5.8	3.4 ± 1.5	1.7 ± 0.9	0.552	
Orthogneiss[*, †, §, **]	56	5.2 ± 3.9	13.7 ± 7.2	4.7 ± 0.8	2.8 ± 1.2	0.098	
Amphibolite[††, §§, ##]	45	0.7 ± 0.7	1.5 ± 1.6	0.7 ± 0.3	0.4 ± 0.3	0.062	
Total Middle Crust							2.02 ± 1.15
Lower Crust							
Eclogite[†, ††]	6	0.9 ± 0.9	1.3 ± 2.1	0.3 ± 0.6	0.4 ± 0.5	0.2	
Felsic granulite[*, ***, †††, §§§, ###]	48	1.7 ± 1.5	4.6 ± 5.5	3.5 ± 1.2	1.2 ± 0.6	0.465	
Mafic granulite[*, †, ***, †††, ###, ****]	20	0.4 ± 0.3	3.7 ± 5.1	1.8 ± 1.5	0.6 ± 0.5	0.335	
Total Lower Crust							0.84 ± 0.42

*Measured using a portable gamma-ray spectrometer in-situ.
[†] Measured with a HPGe detector in laboratory.
[§] Siebel et al., 1997.
[#] Cruciani et al., 2008.
**Cortesogno et al., 1995.
[††] Giacomini et al., 2005.
[§§] Franceschelli et al., 2005.
[##] Gómez-Pugnaire et al., 2003.
***Cocherie et al., 1994.
[†††] Janoušek et al., 2004.
[§§§] Janoušek et al., 2007.
[###] Villaseca et al., 1999.
****Galán & Marcos, 1997.

Table 9.1: *Average radionuclides concentration and heat production at 350 Ma*

Lithotype	Measures number	Mean U (ppm)	Mean Th (ppm)	Mean K (%)	Mean A ($\mu W\ m^{-3}$)	Composition (%)	Gross volumetric heat production ($\mu W\ m^{-3}$)
Upper Crust							
Pelite[*,†]	22	12.0 ± 21.3	14.4 ± 4.2	2.8 ± 1.3	3.9 ± 5	0.678	
Sandstone[*, †]	14	7.5 ± 5.2	13.6 ± 4.7	2.3 ± 1.8	2.7 ± 1.2	0.322	
Total Upper Crust							3.51 ± 0.85
Middle Crust							
Metasediment[*, †]	48	3.4 ± 1	15.1 ± 4.1	3.3 ± 1.4	2.3 ± 0.5	0.175	
Metavolcanic[*, †, §]	53	7.7 ± 4.5	11.8 ± 4.5	4.9 ± 1.4	3.3 ± 1.3	0.112	
Metatexite[*, #]	36	2.6 ± 1.6	9 ± 5.8	3.3 ± 1.5	1.7 ± 0.9	0.13	
Orthogneiss[*, †, §, **]	56	5.2 ± 3.8	13.7 ± 7.2	4.6 ± 0.8	2.8 ± 1.2	0.098	
Leucogranite[*, †]	88	5 ± 2.4	18.6 ± 5.9	5.7 ± 0.7	3.2 ± 0.9	0.13	
Monzogranite[*, †]	122	4.1 ± 1.9	17.9 ± 4	5.1 ± 0.9	2.8 ± 0.7	0.195	
Granodiorite/Tonalite[*, †]	62	2.8 ± 1.3	13.7 ± 3.9	3.8 ± 0.8	2.1 ± 0.6	0.098	
Amphibolite[††, §§, ##]	45	0.7 ± 0.7	1.5 ± 1.6	0.6 ± 0.3	0.4 ± 0.3	0.062	
Total Middle Crust							2.46 ± 0.95
Lower Crust							
Eclogite[†, ††]	6	0.9 ± 0.9	1.3 ± 2.1	0.3 ± 0.6	0.4 ± 0.5	0.2	
Felsic granulite[*, ***, †††, §§§, ###]	48	1.7 ± 1.5	4.6 ± 5.5	3.4 ± 1.1	1.1 ± 0.5	0.465	
Mafic granulite[*, †, ***, †††, ###, ****]	20	0.4 ± 0.3	3.7 ± 5.1	1.8 ± 1.5	0.6 ± 0.5	0.335	
Total Lower Crust							0.79 ± 0.36

[*] Measured using a portable gamma-ray spectrometer in-situ.
[†] Measured with a HPGe detector in laboratory.
[§] Siebel et al., 1997.
[#] Cruciani et al., 2008.
[**] Cortesogno et al., 1995.
[††] Giacomini et al., 2005.
[§§] Franceschelli et al., 2005.
[##] Gómez-Pugnaire et al., 2003.
[***] Cocherie et al., 1994.
[†††] Janoušek et al., 2004.
[§§§] Janoušek et al., 2007.
[###] Villaseca et al., 1999.
[****] Galán & Marcos, 1997.

Table 9.2: *Average radionuclides concentration and heat production at 300 Ma*

9.3 Variscan geotherms compared with P-T-t data sets

The thermal structure of two model crusts constrained at 350 and 300 Ma was calculated by changing Q_0 and H_s within the range of geologically reasonable values. A basal temperature of 1523.15 K is considered equivalent to positioning the astenosphere directly at the base of the crust, therefore models that exceed this limit were not discussed. As shown in experiment 350-12 (Fig. 9.2C), early Carboniferous geotherms support a variation of Q_0 from 4.0 to 13.9 mW m^{-2} assuming that viscous shear dissipation contributes to 0.15 μW m^{-3} to Σ_H. Obviously, geotherms become hotter and their geometry more flat as Q_0 goes to its upper bound. Increasing the H_s contribution from 0 to 0.8 μW m^{-3} with 5.0 mW m^{-2} Q_0 (Fig. 9.2D) still gets hotter geotherms, however the net heating effect of viscous shear dissipation is smaller than Q_0. Yet, the shape of geotherms becomes rapidly steeper as H_s rise to its upper bound value of 1 μW m^{-3} (Burg & Gerya, 2005). Based on a set of experiments performed at variable Q_0 changing H_s over its bounds, we selected the run of experiment 350-17 as the one that best fit the set of thermobarometric constraints compiled from a literature data base (Fig. 9.2A). Importantly, the quadratic best fitting to P-T-t data gives a high-correlation regression curve (Fig. 9.2A) that is almost indistinguishable from the calculated geotherm and assures the points might represent a realistic snapshot on the 350 Ma Variscan thermal structure.

Late Carboniferous geotherms, instead, might support Q_0 ranging from 12.7 to about 23.5 mW m^{-2} for H_s lower than 0.3 μW m^{-3} (Fig. 9.2E). The effect of changing H_s is shown in the experiment 300-21: given the reduced crustal thickness, increasing H_s up to its upper bound does not modifies significantly the shape of the geotherm (Fig. 9.2F). It is immediately apparent from inspection of our preferred result shown in experiment 300-27 (Fig. 9.2B) that no reasonable conductive geotherm matches the ca. 300 Ma P-T-t data points, although the quadratic regression curve is geotherm-like shaped. Best-fitting the set of thermobarometric constraints on the middle crust would (Fig. 9.2E) requires, in fact, a mantle heat flow of 35 – 45 mW m^{-2}. These Q_0values fall within the range of extensional regions such as the Basin and Range and the Rhine Graben (Jaupart & Mareschal, 2007) but violate dramatically the limit of 1523.15 K at the Moho, reaching temperature well above the amphibolite solidus. Finally, it should be noted that for mantle heat flow higher than 23.5 mW m^{-2} there is no way to reproduce the PT conditions recorded by most lower crustal rocks at that time (Villaseca *et* *al*., 1999; Braga *et al*., 2001; Fernandez-Suarez *et al*., 2006; Vilà *et al*., 2007; Cruciani *et al*., 2008; Galli *et al*., 2011).

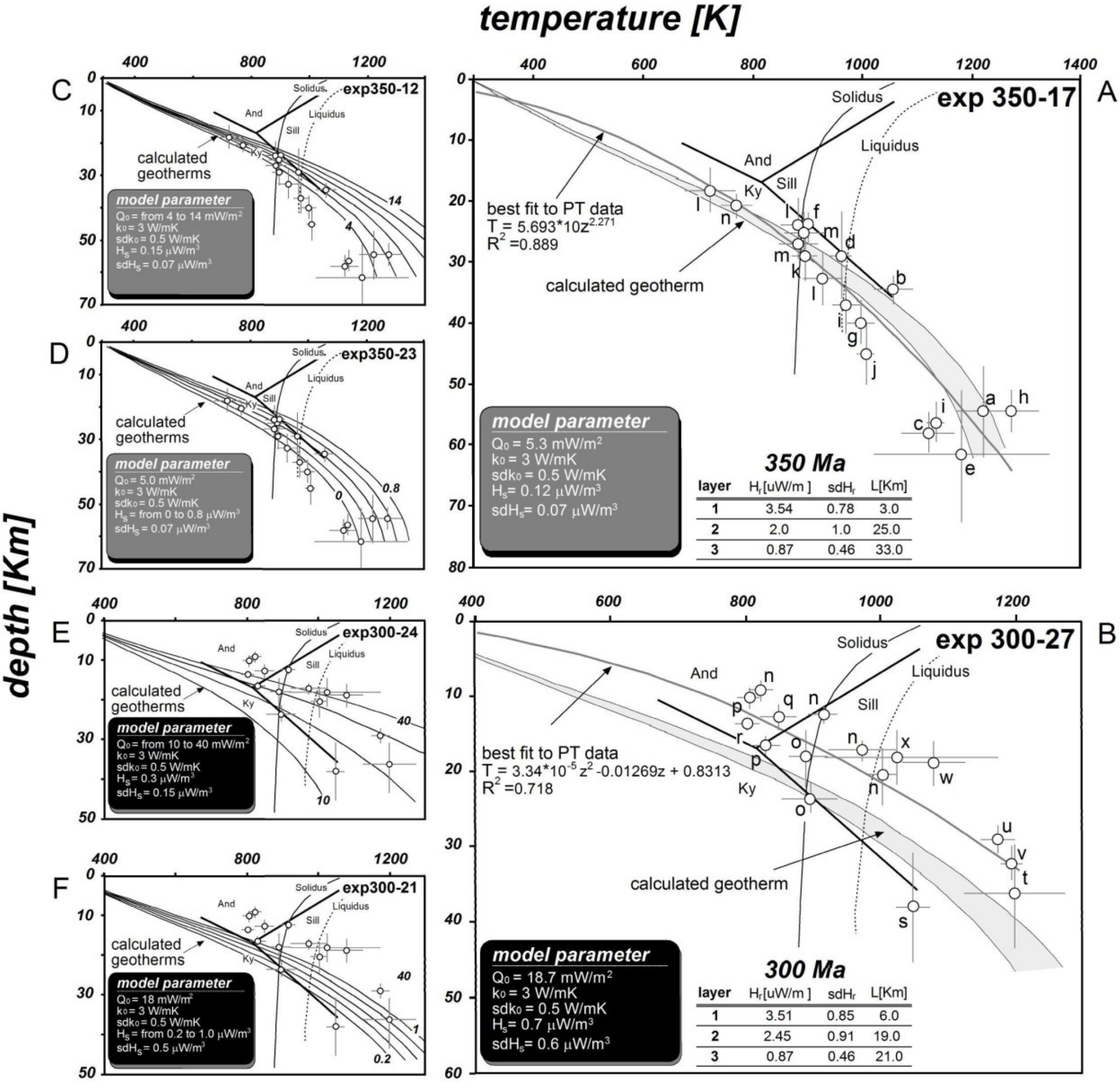

Figure 9.2: *The calculated geotherms at 350 and 300 Ma. a = Giacomini et al. (2008); b = Giacomini et al. (2005); c = Kotkova et al. (1996); d = Stipska et al. (2004); e = Medaris et al. (1995); f = Szrypek et al. (2011); g = Pin & Vielzeuf (1983), Costa et al. (1993); h = Becker (1997), Cook et al. (2000); i = Pereira et al. (2010); j = Rubatto et al. (2010); k = Guillot & Menot (1999); l = Duguet et al. (2007); m = Bellot & Roig (2007); n = Vilà et al. (2007); o = Cruciani et al. (2008); p = Langone et al. (2010); q = Reche et al. (1998); r = Casini et al. (2010); s = Braga & Massonne (2008); t = Villaseca et al. (1999), Fernandez-Suarez et al. (2006); u = Braga et al. (2001); w = Ledru et al. (2001); x = Vavra et al. (1999).*

9.4 Implications for geodynamic models

Understanding the geodynamic significance of the Variscan HT-LP metamorphism requires assessing the heat potential of the mantle in Carboniferous times. Temperature variation in the sub-continental mantle is likely controlled by heat conduction within lherzolites and thermal inflation from the convecting astenosphere. Because of lherzolites have negligible heat production rates and low thermal conductivity, the sub-continental mantle is actually an insulator rather than a source of heat. Therefore, the Moho heat flow may be roughly considered function of the lithospheric mantle thickness. The reference Moho heat flow in stable continental shields ranges between only 12-18 mW m^{-2} (Jaupart & Mareschal, 2007) although the upper bound might be extended to 24 mW m^{-2} depending on the models assumed for thermal conductivity, composition and thickness of the crust (Russell *et al.*, 2001). The permitted limit for Q_0 in regions characterized by steady-state conductive geotherms would be thus lower than 25 mW m^{-2}. Values as high as 60-75 mW m^{-2} are instead typical of extending regions such as the Basin and Range province (Ketcham, 1996) or hot spots like Hawaii (Harris *et al.*, 2000), because of transiently convective thermal regimes. This requires delamination and thinning of the sub-continental mantle or, for upper bound values, positioning the astenosphere directly at the base of the crust. In active compressional margins the geotherm is not in equilibrium because of crustal thickening and erosion (Jaupart & Mareschal, 2007). Disequilibrium of the thermal structure would be even more amplified by intervening slab break-off or stretching of the sub-continental mantle, yet models predict that the upper mantle will recover near steady-state conditions by less than 10 Ma (Davies & von Blanckenburg, 1995). Short timescales for thermal perturbation at the base of the crust are indeed confirmed by present-day low Q_0 values in the Alps or the Himalayan range, which are close to that of shield regions (Vosteen *et al.,* 2003). Our models calculated at ca. 350 Ma require Moho heat flow between only about 4 and 14 mW m^{-2} to reproduce the data set compiled from P-T-t paths of the Moldanubian zone (Fig. 2A). This argues for a purely conductive regime and near-equilibrium conditions in the sub-continental mantle at the time of eo-Variscan HP metamorphism. Interpretation of the predicted Moho heat flow during the HT event is less obvious. The high temperatures recorded across different crustal sections have been frequently explained in terms of increased mantle heat flow due to delamination of the lithosphere or slab breakoff. The timing of HT-LP metamorphism however does not match the likely age of slab break-off in the Variscan belt, bracketed between ca. 360-370 Ma (the oldest age of metamorphic minerals) and ca. 340-335 Ma (the oldest age of sin-collisional Mg-K plutons, Paquette *et al.*, 2003; Finger *et al.*, 2007). Possibly a tighter window could be proposed by emphasizing the exhumation age (ca. 340-345 Ma) of HP granulites (Štípská *et al.*, 2004; Giacomini *et al.*, 2008; Pereira *et al.*, 2010). Fast vertical extrusion of lower crustal slices is actually predicted as side effect of breakoff (Davies & von Blanckenburg, 1995). These early Carboniferous ages of these events rules out the slab breakoff model, as near-equilibrium Moho heat flow would be quickly recovered at least 25-30 Ma before the onset of HT metamorphism. Numerical results (Fig. 9.2B) are in good accordance with the geologic evidences. The predicted Moho heat flow should be in fact lower than 24 mW m^{-2}, surprisingly close to the mean value of a stable geotherm, to avoid unrealistically high temperatures never recorded in the lower crust (Orejana *et al.*, 2011). Any model supporting delamination of the lithospheric mantle would require at least 40-70 mW m^{-2} of basal heat flow (Polyak *et al.*, 1996); and still higher values are expected if ongoing breakoff places the hot astenospheric mantle directly at the base of the crust (Davies & von Blanckenburg, 1995). Based on these arguments, we propose that HT metamorphism in the Variscan belt is related to focused melting in the lower crust, softening of the orogenic roots and collapse of the upper crust. This interpretation best accommodates the sequence of petrologic events and provide a simple explanation for the role of late Carboniferous anatectic batholiths as hot geotherms in the middle crust and near-isothermal conditions in the lower crust require vigorous advection of melts (Depine *et al.*, 2008).

APPENDIX A

347 in-situ measurements have been made for the risk assessment

Samples label	Coordinates (UTM) N	Coordinates (UTM) E	K [%]	σK (%)	U [ppm]	σU (ppm)	Th [ppm]	σTh (ppm)	Act K (Bq/Kg)	σAct K (Bq/Kg)	Act U (Bq/Kg)	σAct U (Bq/Kg)	Act Th (Bq/Kg)	σAct Th (Bq/Kg)	Total Activity (Bq/kg)	I
Grt_64	4539552,080	489436,450	4,780	0,039	1,556	0,089	2,076	0,134	1496,140	12,207	19,217	1,099	8,429	0,544	1537,091	0,605
Grt_199	4554598,64	510305,97	0,984	0,02	1,323	0,079	3,298	0,129	307,992	6,26	16,339	0,976	13,390	0,52374	337,721	0,224
Grt_131	4543820,470	528979,700	1,098	0,023	0,894	0,071	3,576	0,135	343,674	7,199	11,041	0,877	14,519	0,548	377,309	0,224
Grt_63_a	4539653,020	489479,970	2,442	0,029	0,874	0,079	4,871	0,153	764,346	9,077	10,794	0,976	19,776	0,621	804,969	0,390
Grt_132	4542396,260	529722,800	5,500	0,050	4,414	0,131	5,031	0,213	1721,5	15,65	54,513	1,618	20,426	0,865	1813,707	0,858
Grt_423	4535502,79	490981,43	1,623	0,025	2,495	0,097	5,22	0,156	507,999	7,825	30,813	1,198	21,193	0,633	560,005	0,38
Grt_194	4561358,340	524428,890	2,747	0,031	2,779	0,108	5,323	0,166	859,811	9,703	34,321	1,334	21,611	0,674	915,743	0,509
Grt_100	4543756,690	528848,990	1,901	0,026	1,382	0,077	5,701	0,151	595,013	8,138	17,068	0,951	23,146	0,613	644,316	0,371
Grt_178	4526812,860	503783,700	1,399	0,024	2,855	0,099	5,759	0,160	437,887	7,512	35,259	1,223	23,382	0,650	496,528	0,380
Grt_195	4561730,210	524192,690	2,625	0,031	3,658	0,118	7,393	0,187	821,625	9,703	45,176	1,457	30,016	0,759	896,817	0,575
Grt_23	4494369,190	502681,960	5,676	0,060	12,247	0,175	7,443	0,279	1776,588	18,780	151,250	2,161	30,219	1,133	1978,998	1,247
Grt_258	4375719,61	466791,11	3,864	0,044	11,387	0,168	7,793	0,242	1209,43	13,77	140,63	2,07	31,64	0,98	1381,70	1,03
Grt_193	4560508,550	523974,510	2,215	0,030	2,413	0,116	7,804	0,190	693,295	9,390	29,801	1,433	31,684	0,771	754,780	0,489
Grt_266	4376443,36	463450,11	1,52	0,04	1,97	0,14	7,88	0,6	475,76	12,52	24,33	1,73	31,99	2,44	532,08	0,40
Grt_37	4492897,420	511284,950	3,010	0,034	1,617	0,098	8,401	0,192	942,130	10,642	19,970	1,210	34,108	0,780	996,208	0,551
Grt_388	4541366,34	518599,45	4,347	0,039	3,794	0,136	8,689	0,212	1360,611	12,207	46,856	1,68	35,277	0,861	1442,744	0,79
Grt_19	4540179,930	528714,560	3,795	0,042	4,412	0,125	9,488	0,233	1187,835	13,146	54,488	1,544	38,521	0,946	1280,844	0,770
Grt_392	4544011,26	520824,91	3,024	0,035	3,076	0,132	9,772	0,216	946,512	10,955	37,989	1,63	39,674	0,877	1024,175	0,64
Grt_44	4487614,880	517517,590	2,084	0,030	2,501	0,099	10,110	0,197	652,292	9,390	30,887	1,223	41,047	0,800	724,226	0,526
Grt_399	4544585,48	518827,64	3,005	0,033	2,801	0,127	10,154	0,208	940,565	10,329	34,592	1,568	41,225	0,844	1016,383	0,63
Grt_369	4372984,25	467241,04	4,532	0,04	6,237	0,144	10,444	0,222	1418,516	12,52	77,027	1,778	42,403	0,901	1537,946	0,94
Grt_63_b	4539615,990	489465,900	2,625	0,033	0,986	0,100	10,632	0,205	821,625	10,329	12,177	1,235	43,166	0,832	888,532	0,530

Grt_422	4534249,82	490741,23	2,56	0,033	2,98	0,131	10,855	0,218	801,28	10,329	36,803	1,618	44,071	0,885	882,154	0,61
Grt_371	4372797,16	465217,03	4,688	0,041	4,78	0,145	11,018	0,229	1467,344	12,833	59,033	1,79	44,733	0,93	1571,11	0,91
Grt_185	4537898,570	531578,770	4,545	0,039	2,588	0,135	11,315	0,222	1422,585	12,207	31,962	1,667	45,939	0,901	1500,486	0,810
Grt_334	4496499,11	523645,04	4,451	0,037	2,995	0,13	11,445	0,214	1393,163	11,581	36,988	1,605	46,467	0,869	1476,618	0,82
Grt_208	4550127,39	522669,73	3,345	0,035	2,758	0,133	11,513	0,221	1046,985	10,955	34,061	1,642	46,743	0,897	1127,789	0,696
Grt_434	4541587,3	490307,05	3,415	0,035	2,242	0,133	11,56	0,222	1068,895	10,955	27,689	1,642	46,934	0,901	1143,517	0,68
Grt_333	4496524,18	523647,6	4,365	0,038	3,707	0,136	11,594	0,222	1366,245	11,894	45,781	1,68	47,071	0,901	1459,098	0,84
Grt_424	4536958,89	493188,64	3,656	0,037	3,683	0,141	11,623	0,23	1144,328	11,581	45,485	1,741	47,189	0,934	1237,002	0,77
Grt_207	4550173,79	525747,98	3,749	0,037	3,357	0,136	11,648	0,224	1173,437	11,581	41,459	1,68	47,291	0,909	1262,187	0,766
Grt_312	4496880,68	523996,24	5,068	0,041	3,375	0,142	11,668	0,23	1586,284	12,833	41,681	1,754	47,372	0,934	1675,337	0,90
Grt_197	4552645,74	506309,36	3,067	0,035	3,473	0,135	11,739	0,223	959,971	10,955	42,891	1,667	47,660	0,905	1050,523	0,701
Grt_329	4496706,16	523646,15	4,728	0,041	3,4	0,147	11,745	0,238	1479,864	12,833	41,99	1,815	47,684	0,966	1569,539	0,87
Grt_283_b	4541712,9	513317,35	3,588	0,035	3,379	0,131	11,955	0,216	1123,044	10,955	41,731	1,618	48,537	0,877	1213,312	0,76
Grt_101	4548739,010	525121,870	3,824	0,040	2,143	0,119	12,015	0,238	1196,912	12,520	26,466	1,470	48,781	0,966	1286,149	0,731
Grt_427	4538957,12	490841,02	3,941	0,04	6,149	0,154	12,14	0,245	1233,533	12,52	75,94	1,902	49,288	0,995	1358,762	0,91
Bud_15	4501657,650	532880,430	4,404	0,046	4,736	0,138	12,212	0,261	1378,452	14,398	58,49	1,704	49,581	1,060	1486,522	0,902
Grt_394	4546486,65	518989,78	3,739	0,037	2,276	0,137	12,266	0,23	1170,307	11,581	28,109	1,692	49,8	0,934	1248,216	0,73
Grt_330	4496696,43	523660,13	4,952	0,043	3,792	0,153	12,402	0,248	1549,976	13,459	46,831	1,889	50,352	1,007	1647,159	0,92
Grt_332	4496589,24	523654,84	4,736	0,041	3,312	0,146	12,43	0,24	1482,368	12,833	40,903	1,803	50,466	0,974	1573,737	0,88
Grt_167	4528411,490	512340,340	2,757	0,033	2,908	0,131	12,546	0,220	862,941	10,329	35,914	1,618	50,937	0,893	949,792	0,662
Grt_310	4496874,77	523978,96	5,136	0,042	3,33	0,149	12,561	0,242	1607,568	13,146	41,125	1,84	50,998	0,982	1699,691	0,93
Grt_331	4496585,35	523656,04	4,706	0,04	3,408	0,146	12,569	0,238	1472,978	12,52	42,089	1,803	51,030	0,966	1566,097	0,89
Grt_97	4527462,820	508234,910	4,059	0,040	1,512	0,113	12,675	0,232	1270,467	12,520	18,673	1,396	51,461	0,942	1354,516	0,743
Grt_110	4547045,680	529425,110	3,345	0,038	1,925	0,115	12,686	0,234	1046,985	11,894	23,774	1,420	51,505	0,950	1135,578	0,686
Grt_307	4496833,37	523993,5	4,634	0,038	2,115	0,134	12,797	0,225	1450,442	11,894	26,12	1,655	51,956	0,9135	1528,518	0,83
Grt_393	4544349,7	518935,68	3,48	0,034	2,371	0,131	13,053	0,22	1089,24	10,642	29,282	1,618	52,995	0,893	1171,517	0,73
Grt_111	4547041,600	529211,730	3,682	0,039	1,998	0,116	13,064	0,238	1152,466	12,207	24,675	1,433	53,040	0,966	1243,821	0,732
Grt_282	4541795,95	513540,93	3,391	0,034	2,355	0,131	13,087	0,22	1061,383	10,642	29,084	1,618	53,133	0,893	1143,6	0,72
Grt_243	4531250,57	515059,63	2,901	0,035	2,662	0,14	13,091	0,237	908,013	10,955	32,876	1,729	53,149	0,962	994,038	0,678

Grt_108	4547342,550	529153,530	3,409	0,038	2,477	0,116	13,162	0,235	1067,017	11,894	30,591	1,433	53,438	0,954	1164,372	0,725
Grt_200	4557939,69	514259,36	3,383	0,036	1,575	0,137	13,265	0,233	1058,879	11,268	19,451	1,692	53,856	0,946	1132,186	0,687
Grt_71	4539018,650	529880,540	5,396	0,050	3,257	0,141	13,268	0,274	1688,948	15,650	40,224	1,741	53,868	1,112	1800,431	0,966
Bud_11	4496599,880	523666,240	5,201	0,046	2,808	0,133	13,363	0,260	1627,913	14,398	34,679	1,643	54,254	1,056	1716,846	0,930
Grt_116	4554154,760	532207,650	4,362	0,043	2,948	0,129	13,469	0,254	1365,306	13,459	36,408	1,593	54,684	1,031	1471,450	0,850
Grt_288	4492480,09	519572,74	3,52	0,034	1,451	0,128	13,482	0,219	1101,76	10,642	17,92	1,581	54,737	0,889	1174,417	0,70
Grt_305	4492377,29	522169,42	5,868	0,041	3,194	0,144	13,744	0,235	1836,684	12,833	39,446	1,778	55,801	0,954	1931,931	1,02
Grt_120	4548817,110	526914,640	3,986	0,042	2,691	0,125	13,817	0,251	1247,618	13,146	33,234	1,544	56,097	1,019	1351,639	0,807
Grt_119	4549084,940	532936,780	4,144	0,042	2,425	0,124	13,831	0,249	1297,072	13,146	29,949	1,531	56,154	1,011	1397,852	0,813
Grt_109	4547250,420	529428,070	3,886	0,041	2,787	0,125	13,929	0,250	1216,318	12,833	34,419	1,544	56,552	1,015	1321,666	0,803
Grt_155	4533842,720	533887,600	3,858	0,043	4,739	0,136	13,972	0,264	1207,554	13,459	58,527	1,680	56,726	1,072	1337,946	0,881
Grt_78	4562749,010	531845,670	4,534	0,051	6,497	0,160	13,986	0,302	1419,142	15,963	80,238	1,976	56,783	1,226	1574,102	1,024
Grt_298	4492012,92	519462,55	2,66	0,032	1,68	0,13	13,988	0,224	832,58	10,016	20,748	1,6055	56,791	0,909	910,119	0,63
Grt_69	4566013,530	516124,610	4,091	0,041	3,018	0,123	13,991	0,246	1280,483	12,833	37,272	1,519	56,803	0,999	1388,911	0,835
Grt_217	4525952,36	539770,11	3,265	0,037	5,038	0,148	14,005	0,243	1021,945	11,581	62,219	1,828	56,860	0,987	1141,025	0,832
Grt_58	4552488,760	520003,140	3,883	0,043	2,172	0,128	14,043	0,260	1215,379	13,459	26,824	1,581	57,015	1,056	1314,258	0,780
Grt_102	4548232,970	522466,430	4,161	0,043	2,228	0,128	14,087	0,257	1302,393	13,459	27,516	1,581	57,193	1,043	1402,142	0,812
Grt_406	4550455,66	517894,15	4,094	0,04	2,183	0,149	14,174	0,251	1281,422	12,52	26,96	1,84	57,546	1,019	1365,928	0,80
Grt_161	4554170,120	521325,860	4,172	0,038	3,375	0,144	14,218	0,240	1305,836	11,894	41,681	1,778	57,725	0,974	1405,242	0,863
Grt_315	4496876,44	523999,31	4,584	0,039	3,395	0,142	14,254	0,236	1434,792	12,207	41,928	1,7537	57,871	0,958	1534,591	0,91
Grt_257	4545832,78	514794,96	4,291	0,039	3,507	0,148	14,276	0,244	1343,083	12,207	43,311	1,828	57,96	0,991	1444,355	0,882
Grt_407	4548806,59	516465,05	4,111	0,041	4,499	0,156	14,347	0,257	1286,743	12,833	55,563	1,927	58,249	1,043	1400,554	0,91
Grt_188	4534890,770	534229,870	3,550	0,038	4,706	0,148	14,363	0,243	1111,150	11,894	58,119	1,828	58,314	0,987	1227,583	0,856
Grt_59	4554018,920	520379,250	4,494	0,043	2,843	0,128	14,425	0,254	1406,622	13,459	35,111	1,581	58,566	1,031	1515,338	0,879
Grt_166	4541773,700	536171,780	4,529	0,041	4,414	0,153	14,470	0,251	1417,577	12,833	54,513	1,890	58,748	1,019	1530,838	0,948
Grt_306	4496830,98	524024,87	4,597	0,041	2,246	0,15	14,487	0,252	1438,861	12,833	27,738	1,852	58,817	1,023	1525,416	0,87
Grt_136	4535339,010	523281,740	4,118	0,042	2,867	0,126	14,497	0,253	1288,934	13,146	35,407	1,556	58,858	1,027	1397,901	0,842
Grt_289	4492034,36	519431,85	2,635	0,032	1,529	0,132	14,499	0,23	824,755	10,016	18,883	1,63	58,866	0,934	902,504	0,63
Grt_192	4559679,340	513583,400	3,600	0,041	4,892	0,161	14,579	0,265	1126,8	12,833	60,416	1,988	59,191	1,076	1246,407	0,873

Grt_145	4528235,750	533322,320	3,177	0,038	4,310	0,123	14,591	0,246	994,401	11,894	53,229	1,519	59,239	0,999	1120,282	0,805
Grt_295	4492017,94	519418,08	2,65	0,033	1,408	0,134	14,598	0,234	829,45	10,329	17,389	1,655	59,268	0,95	906,107	0,63
Grt_88	4537468,100	509080,100	4,690	0,045	2,526	0,130	14,613	0,262	1467,97	14,085	31,196	1,606	59,329	1,064	1574,185	0,890
Grt_292	4492005,17	519431,19	2,723	0,033	1,78	0,132	14,703	0,23	852,299	10,329	21,983	1,6302	59,694	0,934	933,976	0,66
Grt_308	4496887,99	523994,24	4,445	0,039	2,888	0,145	14,708	0,242	1391,285	12,207	35,667	1,791	59,714	0,982	1486,666	0,88
Grt_12	4514562,090	503956,190	4,665	0,047	3,267	0,141	14,710	0,278	1460,145	14,711	40,347	1,741	59,723	1,129	1560,215	0,920
Grt_198	4553066,15	509531,78	4,182	0,038	4,644	0,146	14,77	0,238	1308,966	11,894	57,353	1,803	59,966	0,966	1426,286	0,927
Grt_293	4492028,14	519410,01	2,664	0,033	2,111	0,136	14,775	0,236	833,832	10,329	26,071	1,68	59,9865	0,958	919,889	0,66
Grt_205	4551783	528731,19	4,259	0,04	3,146	0,149	14,791	0,249	1333,067	12,52	38,853	1,84	60,051	1,011	1431,972	0,874
Grt_361	4537818,45	532968,38	4,633	0,039	2,074	0,142	14,821	0,239	1450,129	12,207	25,614	1,754	60,173	0,97	1535,916	0,87
Grt_297	4492020,86	519452,62	2,665	0,031	1,813	0,127	14,855	0,221	834,145	9,703	22,391	1,568	60,311	0,897	916,847	0,65
Grt_374	4370558	461474,08	4,926	0,042	6,387	0,158	14,936	0,253	1541,838	13,146	78,879	1,951	60,64	1,027	1681,358	1,08
Grt_328	4492271,16	523136,09	3,919	0,039	2,501	0,148	14,937	0,251	1226,647	12,207	30,887	1,828	60,644	1,019	1318,179	0,82
Grt_51	4496557,740	523798,830	4,738	0,048	3,161	0,137	12,342	0,266	1268,700	15,024	42,400	1,692	60,700	1,080	1371,800	0,868
Grt_57	4552150,950	520503,660	4,291	0,042	2,909	0,127	15,048	0,256	1343,083	13,146	35,926	1,568	61,095	1,039	1454,818	0,873
Grt_304	4492220,59	522081,46	4,838	0,042	2,585	0,154	15,079	0,258	1514,294	13,146	31,925	1,902	61,221	1,048	1607,439	0,92
Grt_283	4541732,98	513306,72	3,874	0,039	2,611	0,148	15,119	0,25	1212,562	12,207	32,246	1,828	61,383	1,015	1306,191	0,82
Grt_103	4557778,900	522422,100	4,512	0,044	3,720	0,132	15,130	0,261	1412,256	13,772	45,942	1,630	61,428	1,060	1535,028	0,931
Grd_bor	4526549,070	502864,700	3,893	0,041	3,731	0,127	15,133	0,254	1218,509	12,833	46,078	1,568	61,440	1,031	1340,428	0,867
Grt_277	4540973,27	509554,04	5,017	0,041	3,314	0,149	15,149	0,248	1570,321	12,833	40,928	1,84	61,505	1,007	1672,754	0,97
Grt_65_c	4556322,340	512839,030	1,996	0,019	0,686	0,081	15,176	0,144	624,748	5,947	8,472	1,000	61,615	0,585	701,782	0,545
Grt_314	4496879,64	524003,79	4,738	0,041	2,777	0,152	15,178	0,254	1482,994	12,833	34,296	1,877	61,623	1,031	1578,913	0,92
Grt_52	4499246,460	525671,430	3,680	0,040	2,879	0,126	17,565	0,260	1269,7	12,520	43,4	1,556	61,7	1,056	1374,8	0,876
Grt_65_b	4556322,340	512839,030	1,997	0,019	0,639	0,082	15,211	0,145	625,061	5,947	7,892	1,013	61,757	0,589	701,669	0,543
Grt_272	4528492,74	508070,86	3,922	0,037	2,673	0,143	15,221	0,242	1227,586	11,581	33,011	1,766	61,797	0,982	1322,395	0,83
Grt_28	4495515,860	522303,460	4,830	0,048	2,199	0,139	15,237	0,282	1511,790	15,024	27,158	1,717	61,862	1,145	1617,551	0,904
Grt_92	4545206,820	509549,620	5,759	0,063	11,604	0,198	15,238	0,358	1802,567	19,719	143,309	2,445	61,866	1,453	2029,907	1,388
Grt_25	4491501,920	520503,810	4,316	0,044	2,166	0,129	15,239	0,262	1350,908	13,772	26,750	1,593	61,870	1,064	1454,894	0,849
Grt_323	4492037,48	522482,59	4,168	0,04	2,143	0,149	15,25	0,253	1304,584	12,52	26,466	1,84	61,915	1,027	1392,965	0,83

Grt_300	4491862,77	519246,8	3,298	0,037	2,486	0,146	15,26	0,25	1032,274	11,581	30,702	1,8031	61,956	1,015	1124,932	0,76
Grt_9	4514652,600	503695,420	3,949	0,044	4,244	0,136	15,275	0,270	1236,037	13,772	52,413	1,680	62,017	1,096	1350,467	0,897
Bud_8	4492451,000	520912,750	4,153	0,041	1,679	0,121	15,286	0,251	1299,889	12,833	20,736	1,494	62,061	1,019	1382,686	0,813
Grt_296	4492017,26	519457,85	2,694	0,033	1,659	0,134	15,296	0,233	843,222	10,329	20,489	1,655	62,101	0,946	925,812	0,66
Grt_259	4375659,2	467073,88	5,173	0,043	5,14	0,157	15,357	0,254	1619,15	13,46	63,48	1,94	62,35	1,03	1744,98	1,06
Grt_209	4519082,14	557487,2	3,625	0,039	5,009	0,156	15,378	0,257	1134,625	12,207	61,861	1,927	62,435	1,043	1258,921	0,897
Grt_260	4375461,83	466983,09	3,864	0,043	4,697	0,169	15,395	0,28	1209,43	13,46	58,01	2,09	62,50	1,14	1329,94	0,91
Grt_53	4492455,420	510162,470	2,491	0,031	1,331	0,093	9,288	0,190	1270,7	9,703	44,4	1,149	62,7	0,771	1377,8	0,885
Grt_290	4491980,94	519468,56	2,904	0,036	1,98	0,148	15,465	0,254	908,952	11,268	24,453	1,828	62,788	1,031	996,193	0,70
Grt_265	4375755,51	462169,49	3,544	0,038	4,619	0,151	15,526	0,251	1109,27	11,89	57,04	1,86	63,04	1,02	1229,35	0,88
Grt_322	4491988,55	522492,9	4,321	0,039	2,513	0,148	15,551	0,25	1352,473	12,207	31,035	1,828	63,137	1,015	1446,646	0,87
Grt_31	4499358,970	541547,500	4,809	0,056	14,988	0,186	15,567	0,332	1505,217	17,528	185,102	2,297	63,202	1,348	1773,346	1,435
Grt_17	4536354,320	531180,470	5,142	0,049	5,248	0,149	15,599	0,287	1609,446	15,337	64,813	1,840	63,332	1,165	1737,591	1,069
Grt_177	4532296,880	517912,070	3,488	0,041	6,239	0,166	15,645	0,271	1091,744	12,833	77,052	2,050	63,519	1,100	1232,314	0,938
Grt_156	4533529,700	535064,790	5,161	0,049	4,598	0,147	15,691	0,286	1615,393	15,337	56,785	1,815	63,705	1,161	1753,036	1,046
Grt_372	4372062,43	460286,78	4,433	0,042	4,698	0,152	15,724	0,265	1387,529	13,146	58,02	1,877	63,839	1,076	1509,389	0,98
Grt_301	4491519,19	519395,99	3,467	0,035	2,376	0,138	15,777	0,236	1085,171	10,955	29,344	1,704	64,055	0,958	1178,569	0,78
Grt_318	4491253,08	521807,48	5,613	0,043	2,144	0,151	15,833	0,254	1756,869	13,459	26,478	1,865	64,282	1,031	1847,629	1,00
Grt_247	4537913.75	514106.42	4,535	0,042	1,95	0,153	15,835	0,261	1419,455	13,146	24,082	1,889	64,29	1,06	1507,828	0,875
Bud_14	4499878,340	532465,220	4,340	0,044	2,246	0,130	15,897	0,267	1358,420	13,772	27,738	1,606	64,542	1,084	1450,700	0,868
Grt_262	4375639	467447,94	5,075	0,042	6,263	0,159	15,912	0,256	1588,48	13,15	77,35	1,96	64,60	1,04	1730,43	1,11
Grt_313	4496888,47	524001,73	4,837	0,042	2,911	0,156	15,952	0,262	1513,981	13,146	35,951	1,927	64,765	1,064	1614,697	0,95
Grt_302	4491500,4	519400.71	3,51	0,036	2,157	0,142	15,954	0,243	1098,63	11,268	26,639	1,754	64,773	0,986	1190,042	0,78
Grt_141	4524301,520	529501,040	3,493	0,038	3,185	0,121	15,968	0,246	1093,309	11,894	39,335	1,494	64,830	0,999	1210,862	0,820
Grt_299	4491853,82	519262,71	3,421	0,036	2,023	0,141	15,992	0,243	1070,773	11,268	24,984	1,741	64,927	0,986	1160,685	0,76
Grt_317	4497200,67	524254,86	4,613	0,042	4,156	0,159	16	0,264	1443,869	13,146	51,327	1,964	64,96	1,072	1560,156	0,98
Grt_128	4547770,020	508926,530	4,838	0,048	6,082	0,150	16,055	0,288	1514,294	15,024	75,113	1,853	65,183	1,169	1671,467	1,081
Grt_183	4538122,180	529349,770	5,407	0,044	4,390	0,162	16,082	0,264	1692,391	13,772	54,217	2,001	65,293	1,072	1811,9	1,071
Grt_147	4527415,470	542041,980	3,766	0,041	4,718	0,132	16,400	0,262	1034,5	12,833	61	1,63	65,3	1,064	1175,263	0,875

Grt_30	4497623,540	525330,740	5,244	0,047	3,137	0,137	16,088	0,273	1641,372	14,711	38,742	1,692	65,317	1,108	1761,834	1,003
Grt_325	4492273,99	523150,34	4,231	0,039	2,399	0,148	16,097	0,251	1324,303	12,207	29,628	1,828	65,354	1,019	1419,284	0,87
Grt_320	4491981,09	522479,71	3,916	0,038	2,889	0,147	16,099	0,249	1225,708	11,894	35,679	1,815	65,362	1,011	1326,749	0,85
Grt_80	4562725,920	537545,460	4,590	0,048	7,346	0,152	16,130	0,290	1436,670	15,024	90,723	1,877	65,488	1,177	1609,782	1,109
Grt_324	4492272,96	523143,01	4,238	0,04	2,42	0,15	16,178	0,256	1326,494	12,52	29,887	1,852	65,683	1,04	1422,064	0,87
Grt_27	4495515,860	522303,460	5,218	0,047	2,106	0,137	16,186	0,278	1633,234	14,711	26,009	1,692	65,715	1,129	1741,361	0,960
Grt_311	4496872.43	523989,45	5,042	0,042	3,159	0,154	16,187	0,256	1578,146	13,146	39,014	1,902	65,719	1,039	1682,879	0,98
Grt_261	4375452,75	467022,93	5,255	0,047	8,006	0,179	16,197	0,285	1644,82	14,71	98,87	2,21	65,76	1,16	1809,45	1,21
Grt_206	4551454,47	527311,98	4,936	0,041	3,444	1,152	16,227	0,253	1544,968	12,833	42,533	14,2272	65,882	1,027	1653,383	0,986
Grt_60	4553318,470	519428,640	4,829	0,045	4,118	0,137	16,233	0,270	1511,477	14,085	50,857	1,692	65,906	1,096	1644,017	1,003
Grt_319	4492006,16	522485,93	4,193	0,039	2,097	0,147	16,271	0,252	1312,409	12,207	25,898	1,81545	66,06	1,023	1404,367	0,85
Grt_291	4491976,17	519439,56	3,04	0,035	1,95	0,142	16,294	0,247	951,52	10,955	24,082	1,7537	66,154	1,003	1041,756	0,73
Grt_360	4537775,75	533036,96	5,238	0,043	2,802	0,155	16,318	0,26	1639,494	13,459	34,605	1,914	66,251	1,055	1740,35	0,99
Grt_139	4528937,000	532113,060	2,485	0,037	5,455	0,133	16,321	0,267	777,805	11,581	67,369	1,643	66,263	1,084	924,661	0,815
Grt_148	4520919,780	539314,810	4,323	0,046	5,231	0,147	18,553	0,292	1035,500	14,398	62	1,815	66,3	1,186	1180,013	0,883
Bud_7	4492305,630	520180,470	2,909	0,029	1,839	0,095	16,347	0,199	910,517	9,077	22,712	1,173	66,369	0,808	999,597	0,711
Bud_9	4491848,150	522581,870	3,847	0,039	2,220	0,118	16,348	0,243	1204,111	12,207	27,417	1,457	66,373	0,987	1297,901	0,825
Grt_143	4525416,250	528536,280	4,118	0,047	5,301	0,148	16,351	0,288	1288,934	14,711	65,467	1,828	66,385	1,169	1437,325	0,980
Grt_157	4533951,890	544886,460	5,352	0,048	4,015	0,141	16,357	0,277	1675,176	15,024	49,585	1,741	66,409	1,125	1807,936	1,056
Grt_184	4536848,650	530249,170	4,950	0,043	2,923	0,159	16,368	0,266	1549,350	13,459	36,099	1,964	66,454	1,080	1651,903	0,969
Grt_309	4496883,32	523986,48	4,979	0,044	2,589	0,161	16,403	0,271	1558,427	13,772	31,974	1,988	66,596	1,1	1656,997	0,96
Bud_12	4497040,840	524383,460	5,155	0,048	4,451	0,144	16,413	0,283	1613,515	15,024	54,970	1,778	66,637	1,149	1735,122	1,054
Grt_204	4551647,9	529057,58	4,454	0,04	2,976	0,149	16,564	0,253	1394,102	12,52	36,754	1,84	67,25	1,027	1498,105	0,923
Grt_149	4522591,420	534969,040	4,019	0,043	4,364	0,130	12,657	0,250	1036,500	13,459	63	1,606	67,3	1,015	1181,865	0,892
Grt_7	4513900,380	505243,270	4,564	0,047	4,469	0,144	16,632	0,283	1428,532	14,711	55,192	1,778	67,526	1,149	1551,250	0,998
Grt_83	4532001,250	506527,080	3,824	0,042	4,064	0,133	16,693	0,267	1196,912	13,146	50,19	1,643	67,774	1,084	1329,665	0,905
Grt_171	4539661,300	532616,990	4,518	0,041	3,150	0,156	16,715	0,262	1414,134	12,833	38,903	1,927	67,863	1,064	1520,899	0,940
Bud_10	4492260,970	523217,540	5,136	0,044	2,171	0,128	16,736	0,263	1607,568	13,772	26,812	1,581	67,948	1,068	1702,328	0,965
Grt_212	4523290,84	554488,99	4,533	0,047	9,421	0,186	16,749	0,295	1418,829	14,711	116,349	2,297	68,001	1,198	1603,179	1,201

Grt_357	4537547,5	532906,56	4,916	0,041	3,038	0,151	16,756	0,253	1538,708	12,833	37,519	1,865	68,029	1,027	1644,257	0,98
Grt_362	4537806,69	532960,06	5,288	0,044	2,261	0,16	16,784	0,271	1655,144	13,772	27,923	1,976	68,143	1,1	1751,21	0,99
Grt_326	4492274,86	523156,12	4,004	0,04	2,514	0,153	16,807	0,261	1253,252	12,52	31,048	1,889	68,236	1,06	1352,536	0,86
Grt_76	4539046,110	546587,560	4,909	0,047	6,133	0,148	16,820	0,286	1536,517	14,711	75,743	1,828	68,289	1,161	1697,088	1,106
Grt_150	4523399,190	533122,990	4,139	0,045	5,050	0,141	16,882	0,280	1037,500	14,085	64	1,741	68,3	1,137	1185,626	0,901
Grt_174	4537519,160	532776,880	5,037	0,044	5,182	0,165	16,855	0,271	1576,581	13,772	63,998	2,038	68,431	1,1	1709,01	1,081
Grt_138	4531692,450	530361,130	3,754	0,043	5,117	0,141	16,885	0,289	1175,002	13,459	63,195	1,741	68,553	1,173	1321,95	0,945
Bud_13	4497400,250	526727,290	5,313	0,048	3,750	0,144	16,891	0,286	1662,969	15,024	46,313	1,778	68,577	1,161	1777,859	1,052
Grt_72	4550528,170	538360,590	4,574	0,046	2,919	0,139	16,961	0,283	1431,662	14,398	36,050	1,717	68,862	1,149	1552,688	0,942
Grt_363	4537796,12	532954,68	5,28	0,042	2,119	0,152	16,996	0,259	1652,64	13,146	26,17	1,877	69,004	1,051	1747,813	0,98
Grt_24	4492004,810	519415,650	3,033	0,040	2,910	0,131	17,066	0,270	949,329	12,520	35,939	1,618	69,288	1,096	1068,693	0,783
Grt_43	4487335,150	515737,420	3,537	0,043	2,619	0,137	17,079	0,283	1107,081	13,459	32,345	1,692	69,341	1,149	1208,766	0,824
Grt_244	4535524,05	4531250,57	3,961	0,039	3,577	0,155	17,088	0,261	1239,793	12,207	44,176	1,914	69,377	1,06	1353,346	0,907
Grt_107	4560909,510	516297,580	4,533	0,047	4,502	0,145	17,154	0,287	1418,829	14,711	55,600	1,791	69,645	1,165	1560,576	1,007
Grt_187	4537816,960	534551,720	5,113	0,043	2,551	0,157	17,202	0,264	1600,369	13,459	31,505	1,939	69,840	1,072	1701,714	0,988
Grt_338	4524929,9	506668,83	4,646	0,041	3,782	0,156	17,251	0,261	1454,198	12,833	46,708	1,927	70,039	1,06	1570,945	0,99
Grt_279	4539214,91	513039,49	4,835	0,042	2,685	0,157	17,275	0,267	1513,355	13,146	33,16	1,939	70,136	1,084	1616,651	0,97
Grt_54	4534590,520	507652,440	4,486	0,045	3,890	0,140	17,293	0,280	1404,118	14,085	48,042	1,729	70,210	1,137	1538,183	0,979
Grt_358	4537767,71	533060,35	5,259	0,045	2,937	0,164	17,297	0,275	1646,067	14,085	36,272	2,0254	70,226	1,1165	1752,565	1,02
Grt_8	4514692,970	503669,990	5,606	0,053	7,733	0,162	17,323	0,308	1754,678	16,589	95,503	2,001	70,331	1,250	1920,512	1,255
Grt_140	4526540,590	531854,000	3,971	0,043	4,342	0,137	17,374	0,274	1242,923	13,459	53,624	1,692	70,538	1,112	1382,236	0,946
Grt_186	4538156,260	533589,100	4,841	0,040	2,775	0,152	17,462	0,256	1515,233	12,520	34,271	1,877	70,896	1,039	1620,4	0,974
Bud_6	4491498,920	519307,180	3,681	0,031	2,986	0,100	17,468	0,205	1152,153	9,703	36,877	1,235	70,92	0,832	1259,95	0,862
Grt_340	4524856,51	506615,74	4,668	0,042	3,227	0,159	17,533	0,269	1461,084	13,146	39,853	1,964	71,184	1,092	1572,121	0,98
Grt_90	4537939,270	507599,760	5,088	0,046	2,116	0,133	17,572	0,274	1592,544	14,398	26,133	1,643	71,342	1,112	1706,059	0,975
Grt_359	4537761,24	533067,62	5,493	0,045	2,688	0,163	17,576	0,274	1719,309	14,085	33,197	2,013	71,358	1,112	1823,864	1,04
Grt_267	4376373,52	465569,35	3,673	0,04	5,191	0,164	17,632	0,272	1149,65	12,52	64,11	2,03	71,59	1,10	1285,34	0,95
Grt_33	4499240,460	526574,840	3,740	0,042	2,107	0,129	17,650	0,271	1170,620	13,146	26,021	1,593	71,659	1,100	1283,040	0,835
Grt_408	4530269,26	507783,01	3,766	0,038	2,367	0,148	17,657	0,255	1178,758	11,894	29,232	1,828	71,687	1,035	1279,678	0,85

Grt_271	4526786,87	505527,89	4,32	0,039	2,872	0,153	17,668	0,259	1352,16	12,207	35,469	1,889	71,732	1,0515	1459,361	0,93
Grt_364	4537774,16	532915	5,516	0,044	2,035	0,16	17,676	0,271	1726,508	13,772	25,132	1,976	71,764	1,1	1823,405	1,02
Grt_316	4497218,92	524224,18	4,621	0,041	2,269	0,154	17,724	0,262	1446,373	12,833	28,022	1,902	71,959	1,064	1546,355	0,94
Grt_46	4489831,520	526227,170	5,470	0,051	4,597	0,153	17,724	0,303	1712,110	15,963	56,773	1,890	71,959	1,230	1840,842	1,120
Grt_189	4535487,860	532298,650	5,420	0,043	2,114	0,157	17,735	0,266	1696,460	13,459	26,108	1,939	72,004	1,080	1794,572	1,013
Grt_79	4563226,280	531857,450	5,178	0,056	8,747	0,176	17,735	0,333	1620,714	17,528	108,025	2,174	72,004	1,352	1820,445	1,260
Grt_146	4529142,590	539867,050	3,829	0,042	3,927	0,136	17,751	0,274	1198,477	13,146	48,498	1,680	72,069	1,112	1333,870	0,921
Grt_365	4537766,54	532921,29	5,489	0,044	2,205	0,162	17,759	0,274	1718,057	13,772	27,232	2,001	72,101	1,112	1817,39	1,02
Grt_127	4544789,340	509408,460	4,374	0,046	4,203	0,143	17,822	0,288	1369,062	14,398	51,907	1,766	72,357	1,169	1509,490	0,991
Grt_294	4491976,41	519429,16	3,026	0,034	1,841	0,143	17,827	0,25	947,138	10,642	22,736	1,766	72,378	1,015	1042,252	0,75
Grt_327	4492273,62	523147,38	4,057	0,041	2,098	0,158	17,837	0,272	1269,841	12,833	25,91	1,951	72,418	1,104	1368,17	0,87
Grt_35	4493408,070	528707,370	4,653	0,049	4,682	0,151	17,872	0,300	1456,389	15,337	57,823	1,865	72,56	1,218	1603,974	1,041
Grt_45	4489709,430	526225,880	5,302	0,051	5,023	0,155	17,936	0,305	1659,526	15,963	62,034	1,914	72,82	1,238	1794,38	1,124
Grt_349	4524800,32	506169,43	4,905	0,041	3,288	0,154	17,942	0,259	1535,265	12,833	40,607	1,902	72,844	1,051	1648,716	1,01
Grt_122	4537762,650	508256,240	4,830	0,048	2,087	0,142	17,990	0,293	1511,790	15,024	25,774	1,754	73,039	1,190	1627,382	0,955
Grt_336	4524930,26	506675,95	4,922	0,045	4,319	0,17	18,002	0,282	1540,586	14,085	53,34	2,099	73,088	1,145	1667,014	1,06
Grt_169	4527180,090	508685,280	4,145	0,039	3,544	0,152	18,043	0,257	1297,385	12,207	43,768	1,877	73,255	1,043	1414,408	0,945
Grt_26	4491501,920	520503,810	4,985	0,045	2,678	0,134	18,075	0,273	1560,305	14,085	33,073	1,655	73,385	1,108	1682,503	0,997
Grt_337	4524932,61	506665,69	4,73	0,043	3,989	0,165	18,079	0,275	1480,49	13,459	49,264	2,038	73,401	1,116	1603,155	1,02
Grt_86	4535156,970	502073,480	4,245	0,044	3,140	0,136	18,082	0,278	1328,685	13,772	38,779	1,680	73,413	1,129	1456,329	0,939
Grt_117	4553877,710	533983,810	5,120	0,048	5,767	0,150	18,254	0,293	1602,560	15,024	71,222	1,853	74,111	1,190	1764,770	1,142
Grt_339	4524899,73	506661,74	4,624	0,043	5,832	0,168	18,258	0,275	1447,312	13,459	72,025	2,075	74,127	1,116	1593,465	1,09
Grt_351	4524802,53	506177,09	4,983	0,043	2,915	0,162	18,26	0,275	1559,679	13,459	36	2,001	74,136	1,116	1669,815	1,01
Grt_137	4532244,400	525602,860	4,183	0,046	5,205	0,149	18,274	0,296	1309,279	14,398	64,282	1,840	74,192	1,202	1463,991	1,022
Grt_182	4524795,280	506383,560	4,834	0,044	3,568	0,168	18,292	0,282	1513,042	13,772	44,065	2,075	74,266	1,145	1631,372	1,023
Grt_180	4524795,280	506383,560	4,777	0,042	3,016	0,160	18,364	0,270	1495,201	13,146	37,248	1,976	74,558	1,096	1607,006	0,995
Grt_48	4490964,450	529505,770	4,961	0,047	3,980	0,142	18,486	0,286	1552,793	14,711	49,153	1,754	75,053	1,161	1676,999	1,057
Grt_350	4524806,24	506171,91	4,784	0,043	4,109	0,164	18,523	0,274	1497,392	13,459	50,746	2,0254	75,203	1,112	1623,342	1,04
Grt_162	4544383,490	536669,630	5,571	0,045	5,356	0,171	18,524	0,280	1743,723	14,085	66,147	2,112	75,207	1,137	1885,077	1,178

Grt_345	4524768,25	506281,35	4,913	0,044	3,164	0,167	18,548	0,282	1537,769	13,772	39,075	2,062	75,305	1,145	1652,149	1,02
Grt_84	4533395,720	505109,530	4,048	0,043	3,617	0,137	18,566	0,280	1267,024	13,459	44,670	1,692	75,378	1,137	1402,223	0,948
Grt_321	4491995,03	522471,87	4,412	0,04	1,79	0,151	18,6	0,261	1380,956	12,52	22,106	1,865	75,516	1,06	1478,579	0,91
Grt_105	4559325,090	518662,820	5,265	0,053	4,777	0,162	18,613	0,319	1647,945	16,589	58,996	2,001	75,569	1,295	1801,099	1,124
Grt_158	4538954,250	538684,090	5,212	0,051	7,455	0,159	18,642	0,308	1631,356	15,963	92,069	1,964	75,687	1,250	1817,038	1,229
Grt_202	4556971,85	530684,09	4,438	0,042	5,937	0,168	18,645	0,278	1389,094	13,146	73,322	2,075	75,699	1,129	1538,115	1,086
Grt_153	4531632,610	531189,740	4,312	0,046	4,667	0,146	18,931	0,293	1349,656	14,398	57,637	1,803	76,860	1,190	1500,354	1,026
Grt_181	4524795,280	506383,560	5,270	0,044	3,191	0,166	18,950	0,280	1649,510	13,772	39,409	2,050	76,937	1,137	1765,856	1,066
Grt_164	4543891,770	539992,170	5,545	0,047	7,980	0,184	18,965	0,296	1735,585	14,711	98,553	2,272	76,998	1,202	1911,136	1,292
Grt_344	4524840,73	506560,4	4,905	0,043	4,143	0,166	18,969	0,278	1535,265	13,459	51,166	2,05	77,014	1,129	1663,445	1,07
Grt_125	4546384,510	510000,720	4,643	0,045	4,609	0,141	18,999	0,283	1453,259	14,085	56,921	1,741	77,136	1,149	1603,142	1,060
Grt_249	4537161,96	507262,47	4,198	0,045	6,904	0,184	19,277	0,303	1313,974	14,085	85,264	2,272	78,265	1,23	1477,503	1,114
Grt_179	4525507,150	506684,580	4,336	0,042	2,282	0,162	19,289	0,280	1357,168	13,146	28,183	2,001	78,313	1,137	1463,664	0,938
Grt_94	4553968,280	504252,590	5,028	0,048	4,218	0,149	19,336	0,299	1573,764	15,024	52,092	1,840	78,504	1,214	1721,225	1,091
Grt_343	4524854,67	506555,89	4,923	0,043	2,915	0,165	19,468	0,281	1540,899	13,459	36	2,038	79,04	1,141	1655,939	1,03
Grt_342	4524856,17	506563,1	4,871	0,043	3,984	0,166	19,481	0,28	1524,623	13,459	49,202	2,05	79,093	1,137	1652,918	1,07
Grt_214	4526993,39	550398,68	5,223	0,05	7,303	0,196	19,547	0,318	1634,799	15,650	90,192	2,421	79,361	1,291	1804,352	1,242
Grt_341	4524843,32	506611,92	4,963	0,044	4,382	0,172	19,604	0,288	1553,419	13,772	54,118	2,124	79,592	1,169	1687,129	1,10
Grt_384	4539975,17	517459,18	5,312	0,045	3,326	0,169	19,637	0,285	1662,656	14,085	41,076	2,087	79,726	1,157	1783,458	1,09
Grt_82	4559119,690	532234,190	5,799	0,050	4,090	0,149	19,640	0,298	1815,087	15,650	50,512	1,840	79,738	1,210	1962,827	1,172
Grt_81	4561861,930	538577,990	4,711	0,052	8,355	0,171	19,657	0,331	1474,543	16,276	103,184	2,112	79,807	1,344	1675,923	1,234
Grt_47	4490921,820	527387,190	4,728	0,048	3,826	0,147	19,672	0,298	1479,864	15,024	47,251	1,815	79,868	1,210	1606,983	1,050
Grt_106	4560121,610	518121,260	4,833	0,047	4,939	0,147	19,683	0,292	1512,729	14,711	60,997	1,815	79,913	1,186	1670,165	1,107
Grt_348	4524799,16	506171,51	5,181	0,046	3,86	0,174	19,72	0,292	1621,653	14,398	47,671	2,149	80,063	1,185	1749,387	1,10
Grt_21	4535413,070	521366,650	4,676	0,046	4,061	0,146	19,731	0,293	1463,588	14,398	50,153	1,803	80,108	1,190	1593,849	1,056
Grt_65_a	4556322,340	512839,030	2,163	0,035	1,490	0,124	19,738	0,269	677,019	10,955	18,402	1,531	80,136	1,092	788,043	0,688
Grt3	4532172,42	504466	4,106	0,037	4,500	0,118	19,768	0,239	1285,178	11,581	55,575	1,457	80,258	0,970	1421,011	1,015
Grt_96	4553973,360	504057,990	4,392	0,047	3,498	0,147	19,784	0,301	1374,696	14,711	43,200	1,815	80,323	1,222	1514,746	1,004
Grt_335	4524923,14	506667,71	4,783	0,042	4,166	0,164	19,841	0,277	1497,079	13,146	51,45	2,025	80,554	1,125	1629,084	1,07

Grt_368	4539869,47	537753,72	4,838	0,046	8,586	0,184	19,917	0,299	1514,294	14,398	106,037	2,272	80,863	1,214	1701,194	1,26
Grt_93	4552359,300	506384,240	4,547	0,047	2,125	0,143	19,968	0,300	1423,211	14,711	26,244	1,766	81,070	1,218	1547,002	0,967
Grt_196	4550119,45	504479,47	5,068	0,043	3,616	0,165	19,975	0,278	1586,284	13,459	44,656	2,038	81,098	1,129	1712,04	1,083
Grt_346	4524787,66	506205,61	5,266	0,043	2,68	0,164	20,127	0,279	1648,258	13,459	33,098	2,025	81,716	1,133	1763,072	1,07
Grt_273	4538135,39	508309,52	5,051	0,043	2,614	0,162	20,218	0,277	1580,963	13,459	32,283	2,001	82,085	1,125	1695,331	1,05
Grt_160	4554473,190	518714,090	4,548	0,045	7,391	0,180	20,444	0,295	1423,524	14,085	91,279	2,223	83,003	1,198	1597,805	1,194
Grt_13	4524795,280	506383,560	5,481	0,054	5,082	0,206	20,557	0,340	1715,553	16,902	62,763	2,544	83,461	1,380	1861,777	1,198
Grt_347	4524804,22	506175,19	5,499	0,045	3,804	0,172	20,575	0,29	1721,187	14,085	46,979	2,124	83,534	1,177	1851,701	1,15
Grt_400	4544169,51	517419,94	4,563	0,048	8,558	0,195	20,668	0,318	1428,219	15,024	105,691	2,408	83,912	1,291	1617,822	1,25
Grt_99	4529630,480	517020,960	4,998	0,050	6,724	0,159	20,673	0,313	1564,374	15,650	83,041	1,964	83,932	1,271	1748,961	1,218
Grt_113	4552271,800	536700,040	5,104	0,052	5,715	0,166	20,695	0,331	1597,552	16,276	70,580	2,050	84,022	1,344	1770,480	1,188
Grt_165	4543639,920	540316,870	4,974	0,046	6,157	0,182	20,702	0,302	1556,862	14,398	76,039	2,248	84,050	1,226	1716,951	1,193
Grt_77	4546474,550	542666,880	4,858	0,050	5,802	0,161	20,707	0,319	1520,554	15,650	71,655	1,988	84,070	1,295	1693,917	1,166
Grt_73	4553698,880	540072,950	4,659	0,050	4,329	0,160	20,717	0,324	1458,267	15,650	53,463	1,976	84,111	1,315	1613,467	1,085
Grt_126	4544379,900	507316,980	4,860	0,046	4,203	0,143	20,735	0,289	1521,180	14,398	51,907	1,766	84,184	1,173	1673,435	1,101
Grt_144	4525152,310	530929,020	3,911	0,042	3,210	0,133	20,742	0,277	1224,143	13,146	39,644	1,643	84,213	1,125	1362,788	0,961
Grt_355	4524831,02	509930,96	5,138	0,044	3,372	0,17	20,755	0,288	1608,194	13,772	41,644	2,099	84,265	1,169	1734,104	1,10
Grt_176	4531601,500	522425,330	4,189	0,045	5,545	0,183	20,813	0,307	1311,157	14,085	68,481	2,260	84,501	1,246	1464,139	1,088
Grt_18	4539423,690	533403,140	5,660	0,055	6,870	0,173	20,858	0,338	1771,580	17,215	84,845	2,137	84,683	1,372	1941,108	1,297
Grt_75	4553820,890	543263,900	5,171	0,051	4,314	0,160	20,859	0,322	1618,523	15,963	53,278	1,976	84,688	1,307	1774,427	1,141
Grt_433	4539594,18	492571,27	4,483	0,041	3,913	0,163	20,872	0,277	1403,179	12,833	48,325	2,013	84,740	1,125	1536,245	1,05
Grt_438	4539144,68	493913,72	4,521	0,046	5,834	0,184	20,905	0,306	1415,073	14,398	72,05	2,272	84,874	1,242	1571,997	1,14
Grt_2	4525178,89	503678,56	5,810	0,043	2,971	0,127	20,965	0,259	1818,530	13,459	36,692	1,568	85,118	1,052	1940,340	1,154
Grt_210	4521564,51	558687,36	4,303	0,043	6,781	0,179	20,998	0,297	1346,839	13,459	83,745	2,211	85,252	1,206	1515,836	1,154
Grt_34	4492372,540	525457,800	5,181	0,049	5,157	0,154	21,027	0,308	1621,653	15,337	63,689	1,902	85,370	1,250	1787,950	1,180
Grt_85	4534395,000	501861,630	4,965	0,050	4,794	0,159	21,120	0,319	1554,045	15,650	59,206	1,964	85,747	1,295	1716,612	1,144
Grt_366	4539015,22	534384,71	4,954	0,048	7,689	0,192	21,155	0,315	1550,602	15,024	94,959	2,371	85,889	1,279	1731,45	1,26
Grt_115	4556200,800	533133,330	5,303	0,051	5,544	0,160	21,231	0,319	1659,839	15,963	68,468	1,976	86,198	1,295	1832,444	1,212
Grt_201	4557496,68	516074,81	4,649	0,046	4,651	0,184	21,256	0,31	1455,137	14,398	57,44	2,272	86,299	1,259	1598,876	1,108

Grt_175	4532254,460	523165,000	4,168	0,042	4,859	0,170	21,292	0,288	1304,584	13,146	60,009	2,1	86,446	1,169	1451,038	1,067
Grt_42	4489133,520	513444,440	4,918	0,050	5,740	0,159	21,371	0,318	1539,334	15,650	70,889	1,964	86,766	1,291	1696,989	1,183
Grt_41	4488977,440	513193,230	5,150	0,049	5,012	0,153	21,415	0,307	1611,950	15,337	61,898	1,890	86,945	1,246	1760,793	1,178
Grt_241	4536259,05	521691,38	4,179	0,041	3,093	0,164	21,509	0,282	1308,027	12,833	38,198	2,025	87,326	1,145	1433,552	1,000
Grt_402	4543301,95	518216,99	4,84	0,046	5,034	0,182	21,746	0,306	1514,92	14,398	62,17	2,248	88,289	1,242	1665,379	1,15
Grt_112	4549358,000	535711,430	5,526	0,049	4,513	0,150	21,783	0,303	1729,638	15,337	55,736	1,853	88,439	1,230	1891,002	1,205
Grt_172	4539240,770	533159,340	4,777	0,042	3,957	0,167	21,943	0,283	1495,201	13,146	48,869	2,062	89,089	1,149	1633,159	1,107
Grt_95	4553971,250	504081,710	4,913	0,050	4,317	0,158	21,956	0,322	1537,769	15,650	53,315	1,951	89,141	1,307	1697,827	1,136
Grt_367	4540860,78	537442,67	5,654	0,05	6,586	0,193	21,998	0,319	1769,702	15,65	81,337	2,383	89,312	1,295	1940,351	1,31
Grt_436	4539336,9	494135,04	5,227	0,047	5,615	0,183	22,007	0,307	1636,051	14,711	69,345	2,26	89,348	1,246	1794,745	1,22
Grt_383	4541602,12	515723,5	5,447	0,046	3,705	0,179	22,099	0,303	1704,911	14,398	45,757	2,21	89,722	1,23	1840,39	1,17
Grt_213	4525543,11	551684,3	5,087	0,047	5,58	0,184	22,185	0,307	1592,231	14,711	68,913	2,272	90,071	1,246	1751,215	1,211
Grt_268	4375369,98	468240,02	5,999	0,049	6,091	0,187	22,276	0,309	1877,69	15,34	75,22	2,31	90,44	1,25	2043,35	1,33
Grt_91	4541614,620	508345,800	4,650	0,048	5,356	0,156	22,348	0,315	1455,450	15,024	66,147	1,927	90,733	1,279	1629,280	1,159
Grt_215	4527636,36	552078,72	5,142	0,047	4,757	0,185	22,447	0,311	1609,446	14,711	58,749	2,285	91,135	1,263	1759,330	1,188
Grt_356	4537025,7	530307,84	6,081	0,049	3,602	0,183	22,486	0,309	1903,353	15,337	44,485	2,26	91,293	1,254	2039,131	1,24
Grt_375	4371300,3	468888,83	4,454	0,045	6,675	0,185	22,596	0,31	1394,102	14,085	82,436	2,285	91,74	1,259	1568,278	1,20
Grt_168	4523148,960	510682,350	4,077	0,044	8,028	0,186	22,743	0,309	1276,101	13,772	99,146	2,297	92,337	1,255	1467,583	1,218
Grt_121	4537007,740	510159,130	5,198	0,050	3,565	0,154	22,792	0,318	1626,974	15,650	44,028	1,902	92,536	1,291	1781,089	1,152
Grt_74	4553007,520	540295,780	5,207	0,050	3,066	0,153	23,009	0,318	1629,791	15,650	37,865	1,890	93,417	1,291	1778,612	1,137
Grt_154	4531783,700	532059,780	5,559	0,054	4,979	0,169	23,069	0,340	1739,967	16,902	61,491	2,087	93,660	1,380	1914,107	1,253
Grt_278	4541022,52	509807,97	5,088	0,046	3,594	0,18	23,262	0,308	1592,544	14,398	44,386	2,223	94,444	1,25	1731,374	1,15
Grt_276	4539910.81	509002,37	4,953	0,046	4,215	0,183	23,514	0,311	1550,289	14,398	52,055	2,26	95,467	1,263	1697,811	1,17
Grt_163	4544033,840	540018,130	4,663	0,047	7,161	0,192	23,525	0,320	1459,519	14,711	88,438	2,371	95,512	1,299	1643,469	1,259
Grt_353	4523117,84	504292,54	4,831	0,045	4,13	0,18	23,866	0,306	1512,103	14,085	51,005	2,223	96,896	1,242	1660,004	1,16
Grt_429	4540022,32	491239,03	5,079	0,047	4,074	0,189	23,933	0,322	1589,727	14,711	50,314	2,334	97,168	1,307	1737,209	1,18
Grt_49	4491095,220	531195,200	4,732	0,047	5,783	0,156	24,589	0,315	1481,116	14,711	71,420	1,927	99,831	1,279	1652,367	1,231
Grt_211	4521184,22	559602,98	4,585	0,062	16,301	0,271	24,728	0,433	1435,105	19,406	201,317	3,347	100,39	1,758	1736,818	1,651
Grt_253	4545028,96	510466,7	5,444	0,047	3,925	0,186	24,912	0,316	1703,972	14,711	48,474	2,297	101,143	1,283	1853,588	1,235

Grt_430	4540881,01	490722,82	1,047	0,028	2,985	0,157	24,966	0,285	327,711	8,764	36,865	1,939	101,362	1,1571	465,938	0,74
Grt_435	4542352,61	492662,47	4,532	0,032	2,76	0,173	25,265	0,301	1418,516	10,016	34,086	2,136	102,576	1,222	1555,178	1,10
Grt_32	4500404,940	540465,240	4,961	0,050	4,033	0,161	25,496	0,335	1552,793	15,650	49,808	1,988	103,514	1,360	1723,753	1,201
Grt_442	4542876,77	497488,61	4,184	0,046	6,566	0,195	25,671	0,331	1309,592	14,398	81,09	2,408	104,224	1,344	1494,906	1,23
Grt_124	4543878,630	504546,900	4,476	0,051	6,203	0,169	26,342	0,346	1400,988	15,963	76,607	2,087	106,949	1,405	1602,594	1,257
Grt_443	4544363,31	494813,43	5,011	0,051	10,914	0,216	26,723	0,355	1568,443	15,963	134,788	2,668	108,495	1,441	1811,726	1,51
Grt_6	4511838,800	506552,440	5,298	0,054	4,261	0,172	27,019	0,356	1658,274	16,902	52,623	2,124	109,697	1,445	1820,594	1,277
Grt_39	4493190,540	512663,880	5,185	0,054	6,402	0,177	27,347	0,360	1622,905	16,902	79,065	2,186	111,029	1,462	1812,999	1,360
Grt_274	4538619,56	508658,35	3,932	0,043	5,188	0,187	27,478	0,322	1230,716	13,459	64,072	2,309	111,561	1,307	1406,348	1,18
Grt_50	4492138,790	530410,880	5,151	0,053	5,435	0,172	27,858	0,353	1612,263	16,589	67,122	2,124	113,103	1,433	1792,489	1,327
Grt_4	4531574,03	504748,38	5,458	0,048	8,422	0,159	28,517	0,319	1708,354	15,024	104,012	1,964	115,779	1,295	1928,145	1,495
Grt_441	4541127,52	498509,47	4,958	0,05	4,613	0,207	28,762	0,357	1551,854	15,65	56,97	2,556	116,774	1,449	1725,598	1,29
Grt_1	4526790,26	490940,36	5,018	0,045	5,789	0,150	29,214	0,308	1570,634	14,085	71,494	1,853	118,609	1,250	1760,737	1,355
Grt_38	4493196,920	512558,850	5,079	0,056	8,872	0,192	29,291	0,386	1589,727	17,528	109,569	2,371	118,921	1,567	1818,218	1,490
Grt_123	4541907,810	506070,210	4,746	0,051	6,351	0,171	29,317	0,353	1485,498	15,963	78,435	2,112	119,027	1,433	1701,035	1,352
Grt_151	4532378,160	529823,470	4,624	0,052	5,867	0,174	29,506	0,359	1447,312	16,276	72,457	2,149	119,794	1,458	1657,989	1,323
Grt_191	4534099,000	530474,160	4,597	0,046	4,451	0,195	30,570	0,339	1438,861	14,398	54,970	2,408	124,114	1,376	1617,945	1,283
Grt_190	4534791,140	531486,060	4,623	0,050	7,384	0,216	30,747	0,368	1446,999	15,650	91,192	2,668	124,833	1,494	1663,024	1,410
Grt_98	4529547,600	517114,490	5,477	0,058	9,271	0,198	30,771	0,398	1714,301	18,154	114,497	2,445	124,930	1,616	1974,327	1,578
Grt_152	4533661,580	529844,190	5,331	0,053	5,994	0,176	30,991	0,363	1668,603	16,589	74,026	2,174	125,823	1,474	1887,215	1,432
Grt_216	4528868,64	544124,79	5,467	0,052	7,088	0,218	31,086	0,369	1711,171	16,276	87,537	2,692	126,209	1,498	1924,917	1,493
Grt_11	4515588,820	504134,860	5,372	0,055	5,762	0,183	31,539	0,378	1681,436	17,215	71,161	2,260	128,048	1,535	1880,645	1,438
Grt_10	4515729,840	502368,480	5,348	0,054	7,560	0,182	31,925	0,373	1673,924	16,902	93,366	2,248	129,616	1,514	1896,906	1,517
Grt_287	4494632,89	519717,08	4,866	0,049	6,748	0,212	31,999	0,363	1523,058	15,337	83,338	2,618	129,916	1,474	1736,312	1,44
Grt_87	4537635,970	501145,970	5,817	0,062	7,601	0,205	32,359	0,417	1820,721	19,406	93,872	2,532	131,378	1,693	2067,909	1,577
Grt_446	4539193,09	500755,37	4,951	0,05	10,49	0,219	32,383	0,367	1549,663	15,65	129,551	2,705	131,475	1,49	1810,689	1,61
Grt_286	4540636,39	512633,18	5,362	0,05	3,015	0,21	35,751	0,372	1678,306	15,65	37,235	2,593	145,149	1,51	1860,69	1,41
Grt_40	4493488,930	513013,260	5,530	0,061	12,298	0,214	37,666	0,431	1730,89	19,093	151,88	2,643	152,924	1,750	2035,694	1,848
Grt_376	4368804,02	476392,04	6,486	0,058	11,615	0,248	38,565	0,417	2030,118	18,154	143,445	3,063	156,574	1,693	2330,137	1,94

Grt_284	4541210,03	512857,1	5,743	0,054	1,637	0,224	38,612	0,4	1797,559	16,902	20,217	2,766	156,765	1,624	1974,541	1,45
Grt_378	4363749,95	473222,94	5,486	0,063	14,244	0,282	40,273	0,474	1717,118	19,719	175,913	3,483	163,508	1,924	2056,54	1,98
Grt_285	4540646,42	512725,96	5,095	0,052	2,514	0,226	40,471	0,402	1594,735	16,276	31,048	2,791	164,312	1,632	1790,095	1,46
Grt_379	4368540,98	476489,55	5,542	0,065	13,39	0,3	46,67	0,511	1734,646	20,345	165,366	3,705	189,48	2,075	2089,493	2,08
Grt_380	4368587,73	476497,5	5,443	0,06	10,915	0,274	47,136	0,472	1703,659	18,78	134,8	3,384	191,372	1,916	2029,831	1,97
Grt_377	4364762,09	472273,65	6,07	0,064	11,113	0,287	48,699	0,493	1899,91	20,032	137,245	3,544	197,718	2,001	2234,873	2,08

APPENDIX B

Geological map of the Sardinian batholith

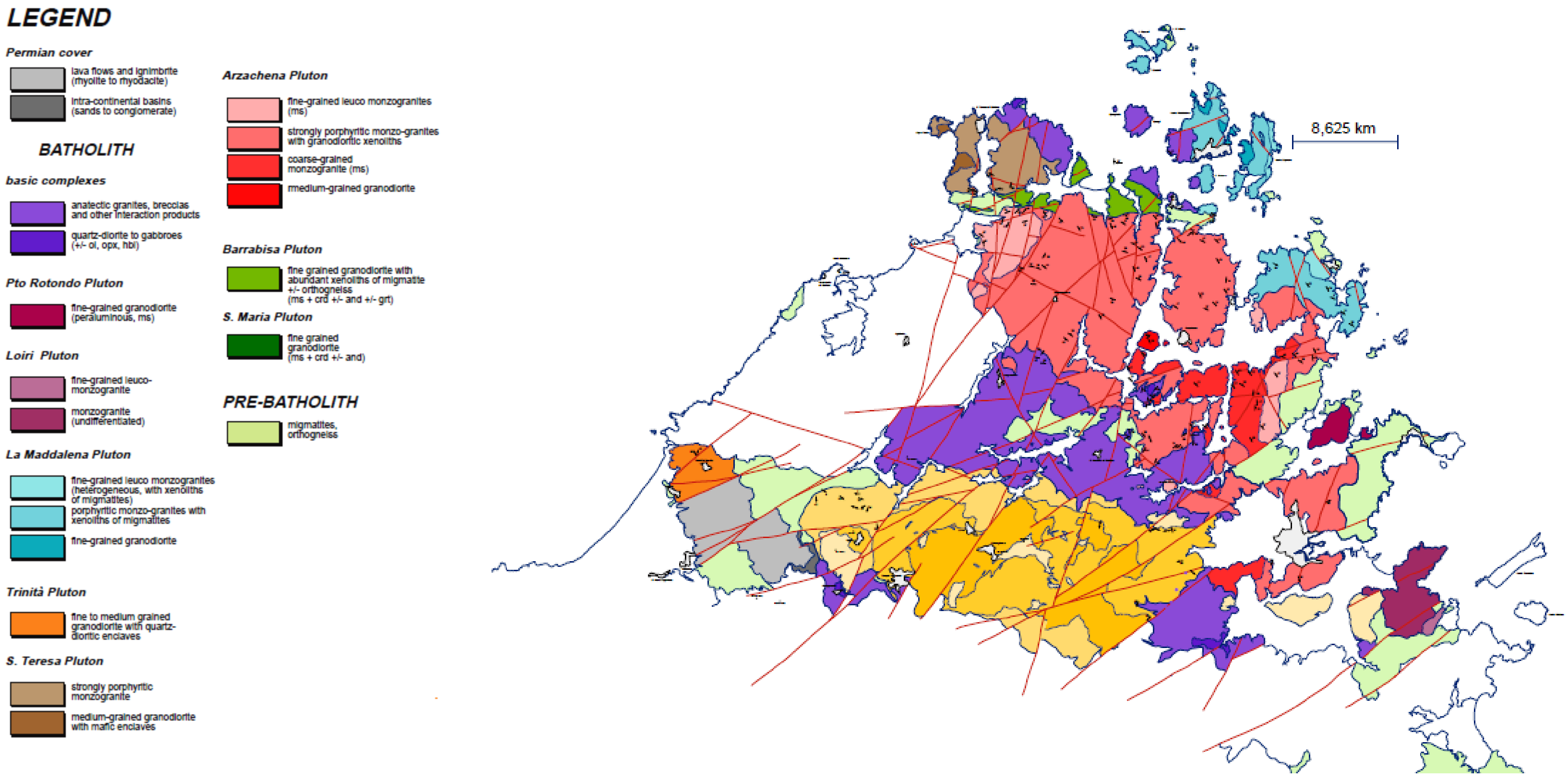
8,625 km
LEGEND
Permian cover
lava flows and ignimbrite (rhyolite to rhyodacite)
intra-continental basins (sands to conglomerate)
BATHOLITH
basic complexes
anatectic granites, breccias and other interaction products
quartz-diorite to gabbroes (+/- ol, opx, hbl)
Pto Rotondo Pluton
fine-grained granodiorite (peraluminous, ms)
Loiri Pluton
fine-grained leuco-monzogranite
monzogranite (undifferentiated)
La Maddalena Pluton
fine-grained leuco monzogranites (heterogeneous, with xenoliths of migmatites)
porphyritic monzo-granites with xenoliths of migmatites
fine-grained granodiorite
Trinità Pluton
fine to medium grained granodiorite with quartz-dioritic enclaves
S. Teresa Pluton
strongly porphyritic monzogranite
medium-grained granodiorite with mafic enclaves
Arzachena Pluton
fine-grained leuco monzogranites (ms)
strongly porphyritic monzo-granites with granodioritic xenoliths
coarse-grained monzogranite (ms)
rmedium-grained granodiorite
Barrabisa Pluton
fine grained granodiorite with abundant xenoliths of migmatite +/- orthogneiss (ms + crd +/- and +/- grt)
S. Maria Pluton
fine grained granodiorite (ms + crd +/- and)
PRE-BATHOLITH
migmatites, orthogneiss

APPENDIX C

Database of the heat production in the Variscan crust at 350 Ma and 300 Ma

*Measured with a HPGe detector in laboratory.
[a]Cruciani et al., 2008.
[b]Cortesogno et al., 1995.
[c]Giacomini et al., 2005.
[d]Franceschelli et al., 2005.
[e]Cocherie et al., 1994.
[f]Janoušek et al., 2004.
[g]Janoušek et al., 2007.
[h]Galán & Marcos, 1997.
[i]Siebel et al., 1997.
[l]Villaseca et al., 1999.
[m]Gómez-Pugnaire et al., 2003.

UPPER CRUST (LAYER 1)

Samples label	Rock type	Location		K_{350Ma} (%)	cU_{350Ma} (ppm)	cTh_{350Ma} (ppm)	K_{300Ma} (%)	eU_{300ma} (ppm)	cTh_{300Ma} (ppm)	ρ (Kg m^{-3})	H_{350Ma} (μW m^{-3})	H_{300Ma} (μW m^{-3})
		N (UTM-WGS84)	E (UTM-WGS 84)									
Teg5	Pelite	4505557,7	432634,0	3,43	26,95	15,38	3,34	26,74	15,35	2400	7,4	7,3
Teg6	Pelite	4505557,7	432634,0	4,58	17,76	12,44	4,46	17,62	12,41	2400	5,2	5,2
Teg7	Pelite	4505550,3	432651,9	3,79	19,86	14,20	3,69	19,71	14,17	2400	5,7	5,7
Camp_13Cp1*	Pelite	4506303,3	434667,9	5,81	103,16	20,04	5,65	102,36	19,99	2400	25,3	25,1
Ord_Bac	Pelite	4378960,2	537134,9	6,71	3,68	18,42	6,53	3,65	18,37	2400	2,5	2,5
1_Ge*	Pelite	4505563,02	432572,23	3,18	11,15	17,44	3,10	11,06	17,40	2400	3,9	3,9
2_Ge*	Pelite	4505563,02	432572,23	1,59	4,40	7,20	1,54	4,37	7,19	2400	1,6	1,6
3_Ge*	Pelite	4505563,02	432572,23	2,02	1,21	7,24	1,97	1,20	7,23	2400	0,9	0,9
4_Ge*	Pelite	4505563,03	432572,23	2,02	1,62	6,60	1,97	1,60	6,59	2400	0,9	0,9
4a_Ge*	Pelite	4505563,03	432572,23	4,10	2,90	14,62	3,99	2,88	14,59	2400	1,9	1,9
5_Ge*	Pelite	4505563,03	432572,23	2,01	4,94	14,99	1,96	4,90	14,95	2400	2,2	2,2
Siltiti_2_Ge*	Pelite	4506605,89	430664,65	1,61	4,02	14,15	1,57	3,99	14,12	2400	1,9	1,9
Siltiti_3	Pelite	4506604,36	430661,22	2,86	4,94	16,34	2,79	4,90	16,30	2400	2,4	2,4

Siltiti_4_Ge*	Pelite	4506602,02	430660,6	2,91	5,46	19,08	2,83	5,42	19,03	2400	2,7	2,6
Siltiti_5_Ge*	Pelite	4506600,58	430658,32	1,69	2,10	13,41	1,65	2,08	13,38	2400	1,4	1,4
Siltiti_6_Ge*	Pelite	4506598,98	430656,16	2,09	4,56	6,20	2,04	4,53	6,18	2400	1,6	1,6
Siltiti_7	Pelite	4506598,04	430655,07	2,00	2,71	13,88	1,95	2,69	13,85	2400	1,6	1,6
Siltiti_8_Ge*	Pelite	4506599,55	430661,47	1,37	7,94	15,76	1,33	7,88	15,72	2400	2,9	2,9
Siltiti_9	Pelite	4506593,79	430653,54	3,15	7,30	18,70	3,06	7,25	18,65	2400	3,1	3,1
Siltiti_10_Ge*	Pelite	4506614,22	430738,92	2,52	19,31	19,87	2,45	19,16	19,82	2400	5,8	5,8
Siltiti_11	Pelite	4506618,35	430748,21	2,31	4,43	13,66	2,25	4,40	13,63	2400	2,0	2,0
Siltiti_12	Pelite	4506617,96	430755,08	2,52	5,83	17,44	2,45	5,78	17,39	2400	2,6	2,6
Tcg 12	Sandstone	4529389,4	501782,2	4,02	9,94	17,98	3,92	9,86	17,94	2400	3,7	3,7
Camp_11*	Sandstone	4597139,1	503300,1	5,33	5,39	19,84	5,18	5,34	19,79	2400	2,9	2,9
Camp_11a*	Sandstone	4598693,5	503512,6	4,96	9,61	18,42	4,83	9,53	18,37	2400	3,7	3,7
Camp_11b*	Sandstone	4598693,5	503512,6	4,48	2,64	17,40	4,36	2,62	17,36	2400	2,0	2,0
Camp_11c*	Sandstone	4598693,5	503512,6	4,36	5,91	19,23	4,24	5,87	19,18	2400	2,9	2,9
Camp_13Cp2*	Sandstone	4506303,3	434667,9	1,82	7,07	18,72	1,77	7,02	18,68	2400	2,9	2,9
Cong_1	Sandstone	4505575,55	432579,6	0,98	19,70	11,50	0,95	19,55	11,47	2400	5,3	5,3
Cong_2	Sandstone	4505593,83	432583,61	0,54	15,33	7,46	0,52	15,21	7,44	2400	4,0	4,0
Cong_3	Sandstone	4506691,75	431621,79	0,97	4,75	10,23	0,95	4,71	10,20	2400	1,8	1,8
Cong_3_Ge*	Sandstone	4506691,75	431621,79	0,29	2,80	10,26	0,28	2,78	10,23	2400	1,3	1,3
Cong_4	Sandstone	4506595,94	430691,12	1,45	2,17	11,14	1,41	2,16	11,11	2400	1,3	1,3
Cong_5	Sandstone	4506598,9	430706,41	1,96	12,52	13,16	1,91	12,42	13,12	2400	3,8	3,8
Cong_5_Ge*	Sandstone	4506598,9	430706,41	1,27	4,47	7,87	1,24	4,43	7,85	2400	1,6	1,6
Cong_7_Ge*	Sandstone	4506609,08	430767,23	0,27	3,98	8,32	0,26	3,95	8,30	2400	1,4	1,4

MIDDLE CRUST (LAYER 2)

Samples label	Rock type	Location		K_{350Ma} (%)	eU_{350Ma} (ppm)	eTh_{350Ma} (ppm)	K_{300Ma} (%)	eU_{300Ma} (ppm)	eTh_{300Ma} (ppm)	ρ (Kg m^{-3})	H_{350Ma} (μW m^{-3})	H_{300Ma} (μW m^{-3})
		N (UTM-WGS84)	E (UTM-WGS 84)									
OS_1	Metasediment	4514120,030	436642,380	0,43	5,56	20,08	0,42	5,52	20,03	2750	2,9	2,9
Disc_OS_2	Metasediment	4515173,430	435079,350	4,13	3,59	21,61	4,01	3,56	21,56	2750	2,9	2,8
OS_3	Metasediment	4514531,360	430215,580	0,61	2,68	13,77	0,59	2,66	13,74	2750	1,7	1,7
Ord_Bac_2	Metasediment	4378960,2	537134,9	2,26	5,58	12,01	2,20	5,54	11,98	2750	2,5	2,5
BL_9	Metasediment	4376885,4	547409,3	3,65	4,33	17,43	3,55	4,30	17,38	2750	2,7	2,7
BL_10	Metasediment	4376885,4	547409,3	3,74	5,00	18,10	3,64	4,96	18,05	2750	2,9	2,9
BL_11	Metasediment	4376885,4	547409,3	4,40	3,85	14,87	4,28	3,82	14,84	2750	2,5	2,5
Fil_1	Metasediment	4506771,37	430914,25	4,01	4,21	17,28	3,91	4,18	17,24	2750	2,7	2,7
Fil_2	Metasediment	4511279,44	428827,34	4,95	3,15	22,66	4,81	3,13	22,60	2750	2,9	2,9
Fil_2_Ge	Metasediment	4511279,44	428827,34	3,79	4,40	17,97	3,69	4,37	17,92	2750	2,8	2,8
Fil_3	Metasediment	4511318,27	428788,91	4,62	1,71	20,15	4,49	1,70	20,10	2750	2,3	2,3
Fil_4	Metasediment	4509691,34	429121,45	4,91	4,10	20,63	4,78	4,06	20,58	2750	3,0	3,0
Meta_grov	Metasediment	4515846,12	432645,99	5,36	1,14	16,86	5,21	1,13	16,82	2750	2,0	2,0
Para_gneiss	Metasediment	4535575,92	433212,07	3,78	3,41	13,46	3,68	3,39	13,43	2750	2,2	2,2
PGP_1_Ge*	Metasediment	4535575,92	433212,07	4,15	3,76	16,34	4,04	3,73	16,30	2750	2,5	2,5
Para_gneiss_2	Metasediment	4535576,03	433235,86	4,14	2,38	13,50	4,03	2,36	13,47	2750	2,0	2,0
PGP_2_Ge*	Metasediment	4535576,03	433235,86	2,86	3,00	12,26	2,78	2,98	12,23	2750	1,9	1,9
Quarz_1	Metasediment	4510057,42	427737,92	2,83	2,70	11,82	2,76	2,68	11,79	2750	1,8	1,8
Quarz_1_Ge*	Metasediment	4510057,42	427737,92	1,55	1,67	7,98	1,51	1,66	7,96	2750	1,1	1,1
Quarz_2	Metasediment	4509713,66	429109,81	5,25	4,02	19,66	5,11	3,99	19,61	2750	2,9	2,9
Quarz_2_Ge*	Metasediment	4509713,66	429109,81	1,38	2,27	10,10	1,34	2,25	10,08	2750	1,4	1,4
A1*	Metasediment			2,92	2,03	9,93	2,84	2,02	9,91	2750	1,5	1,5
A2*	Metasediment			2,85	2,39	10,81	2,77	2,37	10,78	2750	1,7	1,6
A3*	Metasediment			5,42	3,65	15,78	5,27	3,62	15,74	2750	2,6	2,6
A4*	Metasediment			6,38	4,12	17,03	6,21	4,09	16,99	2750	2,9	2,9

A5*	Metasediment			5,82	3,58	12,13	5,66	3,55	12,10	2750	2,3	2,3
Q1*	Metasediment			2,26	3,69	13,49	2,20	3,66	13,45	2750	2,1	2,1
Q2*	Metasediment			1,41	3,07	19,16	1,37	3,04	19,11	2750	2,3	2,3
Q3*	Metasediment			2,46	2,31	9,19	2,40	2,29	9,17	2750	1,5	1,5
Q4*	Metasediment			2,41	4,90	23,72	2,34	4,87	23,66	2750	3,2	3,2
Q5*	Metasediment			2,69	2,62	13,76	2,62	2,60	13,72	2750	1,9	1,9
Q6*	Metasediment			1,59	3,19	13,48	1,55	3,16	13,44	2750	1,9	1,9
Q7*	Metasediment			1,68	1,71	3,76	1,63	1,70	3,75	2750	0,9	0,9
Q8*	Metasediment			1,59	4,42	15,84	1,55	4,39	15,80	2750	2,4	2,4
Q9*	Metasediment			2,72	4,35	15,47	2,65	4,32	15,43	2750	2,5	2,5
Q10*	Metasediment			2,01	1,67	9,11	1,96	1,66	9,09	2750	1,3	1,3
Q11*	Metasediment			2,27	2,89	8,49	2,21	2,87	8,46	2750	1,6	1,6
S10*	Metasediment			4,34	3,91	18,01	4,22	3,88	17,96	2750	2,7	2,7
S11*	Metasediment			4,36	3,73	17,15	4,24	3,70	17,11	2750	2,6	2,6
S12*	Metasediment			4,59	4,03	19,52	4,47	4,00	19,47	2750	2,9	2,8
S13*	Metasediment			4,50	4,53	17,39	4,38	4,50	17,35	2750	2,8	2,8
S14*	Metasediment			4,16	4,32	16,49	4,05	4,29	16,45	2750	2,7	2,7
S15*	Metasediment			3,79	3,81	15,78	3,68	3,78	15,74	2750	2,5	2,5
S16*	Metasediment			2,67	3,08	11,63	2,60	3,05	11,60	2750	1,9	1,9
S17*	Metasediment			4,97	2,80	17,34	4,84	2,78	17,30	2750	2,4	2,4
S18*	Metasediment			3,39	3,10	12,14	3,30	3,08	12,11	2750	2,0	2,0
S19*	Metasediment			2,28	3,82	14,60	2,21	3,79	14,57	2750	2,2	2,2
S20*	Metasediment			4,63	3,94	16,72	4,50	3,91	16,68	2750	2,7	2,6
BL_1	Metavolcanic	4376980,5	546682,3	7,72	11,32	15,25	7,51	11,23	15,21	2750	4,8	4,7
BL_2	Metavolcanic	4376986,4	546549,1	5,36	4,94	14,91	5,22	4,90	14,87	2750	2,9	2,8
BL_3	Metavolcanic	4377070,4	546479,6	4,60	6,38	12,12	4,48	6,33	12,09	2750	3,0	2,9
BL_4	Metavolcanic	4377186,4	546441,3	6,11	6,12	16,79	5,95	6,08	16,75	2750	3,4	3,3
BL_5	Metavolcanic	4377263,3	546338,4	4,59	17,25	14,09	4,47	17,11	14,06	2750	5,9	5,9
BL_6	Metavolcanic	4376885,4	547409,3	6,50	4,83	14,08	6,33	4,80	14,05	2750	2,9	2,9

BL_7	Metavolcanic	4376885,4	547409,3	3,64	3,46	9,55	3,55	3,44	9,53	2750	1,9	1,9
BL_8	Metavolcanic	4376885,4	547409,3	4,33	5,56	12,21	4,21	5,52	12,18	2750	2,7	2,7
BL_12	Metavolcanic	4376885,4	547409,3	4,92	3,56	12,55	4,78	3,53	12,52	2750	2,3	2,3
P1*	Metavolcanic			4,02	3,08	11,01	3,91	3,06	10,99	2750	2,0	1,9
P2*	Metavolcanic			4,00	4,23	11,54	3,90	4,20	11,51	2750	2,3	2,3
P3*	Metavolcanic			3,39	3,47	11,30	3,30	3,44	11,27	2750	2,0	2,0
P4*	Metavolcanic			4,16	4,63	11,30	4,04	4,59	11,27	2750	2,4	2,4
P5*	Metavolcanic			4,27	3,63	12,10	4,16	3,60	12,07	2750	2,2	2,2
P6*	Metavolcanic			1,96	4,76	9,58	1,90	4,73	9,55	2750	2,1	2,1
P7*	Metavolcanic			3,85	3,69	14,13	3,75	3,66	14,10	2750	2,3	2,3
P8*	Metavolcanic			4,40	5,49	13,16	4,29	5,44	13,13	2750	2,8	2,8
527^{i}	Metavolcanic			2,88	0,00	19,33	2,80	0,00	19,28	2750	1,6	1,6
529^{i}	Metavolcanic			4,81	5,28	15,26	4,68	5,24	15,22	2750	2,9	2,9
642^{i}	Metavolcanic			4,99	11,61	8,14	4,86	11,52	8,12	2750	4,1	4,1
644^{i}	Metavolcanic			4,98	10,56	12,21	4,85	10,48	12,18	2750	4,1	4,1
646^{i}	Metavolcanic			6,41	5,28	16,28	6,24	5,24	16,24	2750	3,1	3,1
643^{i}	Metavolcanic			4,59	14,78	11,19	4,47	14,67	11,16	2750	5,1	5,1
637^{i}	Metavolcanic			7,08	9,50	0,00	6,89	9,43	0,00	2750	3,2	3,1
640^{i}	Metavolcanic			7,13	10,56	0,00	6,94	10,48	0,00	2750	3,4	3,4
533^{i}	Metavolcanic			5,76	16,89	13,23	5,60	16,76	13,19	2750	5,9	5,9
758^{i}	Metavolcanic			6,03	0,00	12,21	5,87	0,00	12,18	2750	1,4	1,4
639^{i}	Metavolcanic			6,36	10,56	6,10	6,19	10,48	6,09	2750	3,8	3,8
638^{i}	Metavolcanic			6,35	14,78	9,16	6,18	14,67	9,13	2750	5,1	5,1
759^{i}	Metavolcanic			5,79	0,00	0,00	5,63	0,00	0,00	2750	0,6	0,5
761^{i}	Metavolcanic			4,86	0,00	8,14	4,73	0,00	8,12	2750	1,0	1,0
525^{i}	Metavolcanic			4,55	0,00	11,19	4,43	0,00	11,16	2750	1,2	1,2
760^{i}	Metavolcanic			4,83	0,00	0,00	4,70	0,00	0,00	2750	0,5	0,5
572^{i}	Metavolcanic			7,42	10,56	15,26	7,22	10,48	15,22	2750	4,5	4,5
565^{i}	Metavolcanic			7,86	13,73	15,26	7,65	13,62	15,22	2750	5,4	5,4

566[i]	Metavolcanic			7,91	9,50	15,26	7,70	9,43	15,22	2750	4,3	4,3
568[i]	Metavolcanic			4,54	10,56	11,19	4,42	10,48	11,16	2750	4,0	4,0
564[i]	Metavolcanic			3,89	9,50	13,23	3,79	9,43	13,19	2750	3,8	3,8
578[i]	Metavolcanic			5,90	11,61	9,16	5,74	11,52	9,13	2750	4,2	4,2
576[i]	Metavolcanic			7,01	13,73	8,14	6,82	13,62	8,12	2750	4,8	4,8
567[i]	Metavolcanic			5,24	8,45	8,14	5,09	8,38	8,12	2750	3,3	3,3
575[i]	Metavolcanic			6,80	12,67	9,16	6,62	12,57	9,13	2750	4,6	4,6
570[i]	Metavolcanic			2,27	9,50	8,14	2,21	9,43	8,12	2750	3,3	3,3
659[i]	Metavolcanic			2,14	12,67	15,26	2,08	12,57	15,22	2750	4,6	4,6
627[i]	Metavolcanic			5,48	8,45	16,28	5,33	8,38	16,24	2750	3,9	3,8
660[i]	Metavolcanic			4,16	10,56	10,17	4,05	10,48	10,15	2750	3,9	3,8
661[i]	Metavolcanic			4,11	11,61	15,26	4,00	11,52	15,22	2750	4,5	4,5
656[i]	Metavolcanic			4,59	12,67	16,28	4,47	12,57	16,24	2750	4,9	4,9
624[i]	Metavolcanic			4,65	8,45	16,28	4,53	8,38	16,24	2750	3,8	3,8
657[i]	Metavolcanic			4,94	8,45	16,28	4,81	8,38	16,24	2750	3,8	3,8
655[i]	Metavolcanic			4,28	5,28	13,23	4,17	5,24	13,19	2750	2,7	2,7
628[i]	Metavolcanic			4,63	9,50	16,28	4,51	9,43	16,24	2750	4,1	4,0
630[i]	Metavolcanic			4,11	9,50	19,33	4,00	9,43	19,28	2750	4,2	4,2
Met1	Metatexite	4535560,3	501568,9	4,08	4,86	11,14	3,97	4,82	11,11	2900	2,6	2,6
Met2	Metatexite	4536465,0	501601,3	4,73	6,60	20,15	4,60	6,55	20,10	2900	3,8	3,8
Grt_62	Metatexite	4559159,170	530525,350	6,23	3,96	17,45	6,07	3,93	17,41	2900	3,0	3,0
Met_7	Metatexite	4557748,670	533746,240	4,36	5,39	17,46	4,25	5,35	17,41	2900	3,2	3,2
Grt_66	Metatexite	4558988,770	513745,960	4,99	4,10	11,30	4,86	4,07	11,27	2900	2,5	2,5
Grt_67	Metatexite	4559076,470	513652,060	5,43	4,68	14,80	5,28	4,65	14,76	2900	2,9	2,9
Met_8	Metatexite	4536867,930	502492,650	5,20	3,22	6,65	5,06	3,19	6,63	2900	1,9	1,9
Met_10	Metatexite	4551245,330	442536,700	6,51	6,59	3,78	6,34	6,54	3,77	2900	2,8	2,7
Met_12	Metatexite	4558915,150	514030,960	4,11	1,15	18,29	4,00	1,14	18,24	2900	2,1	2,1
Met_20	Metatexite	4510379,69	560369,51	4,12	2,94	11,43	4,01	2,91	11,40	2900	2,1	2,1
Met_21	Metatexite	4510513,1	560402,05	4,68	4,44	12,02	4,55	4,40	11,99	2900	2,6	2,6

Met_22	Metatexite	4510602,26	560328,1	5,82	4,29	10,02	5,66	4,26	9,99	2900	2,5	2,5
B70[a]	Metatexite			2,47	1,27	5,89	2,40	1,26	5,88	2900	1,0	1,0
B71[a]	Metatexite			2,28	4,22	22,59	2,21	4,19	22,53	2900	3,1	3,1
B73[a]	Metatexite			2,92	1,97	3,95	2,84	1,96	3,94	2900	1,1	1,1
B74[a]	Metatexite			2,35	2,46	16,94	2,29	2,44	16,90	2900	2,2	2,2
B83[a]	Metatexite			2,43	0,84	9,16	2,37	0,84	9,13	2900	1,2	1,1
B91[a]	Metatexite			2,53	1,80	8,33	2,46	1,78	8,31	2900	1,4	1,4
B93[a]	Metatexite			1,54	2,96	18,31	1,50	2,93	18,27	2900	2,3	2,3
B97[a]	Metatexite			2,81	2,06	7,25	2,73	2,04	7,24	2900	1,4	1,4
B295[a]	Metatexite			3,32	3,08	10,38	3,23	3,06	10,35	2900	2,0	1,9
B296[a]	Metatexite			2,81	3,24	11,09	2,73	3,22	11,06	2900	2,0	2,0
B325[a]	Metatexite			3,41	0,78	5,12	3,32	0,78	5,11	2900	0,9	0,9
B326[a]	Metatexite			2,68	1,36	6,82	2,60	1,35	6,80	2900	1,2	1,1
B82[a]	Metatexite			1,67	1,06	7,12	1,63	1,05	7,10	2900	1,0	1,0
B84[a]	Metatexite			0,62	0,90	2,72	0,60	0,89	2,71	2900	0,5	0,5
B85[a]	Metatexite			1,45	1,11	5,79	1,41	1,10	5,78	2900	0,9	0,9
B86[a]	Metatexite			1,02	0,62	1,73	0,99	0,62	1,73	2900	0,4	0,4
B92[a]	Metatexite			0,94	1,28	3,86	0,92	1,27	3,85	2900	0,7	0,7
B251[a]	Metatexite			1,49	1,51	2,78	1,45	1,50	2,77	2900	0,8	0,8
B246[a]	Metatexite			3,64	1,37	3,05	3,55	1,36	3,04	2900	1,0	1,0
B247[a]	Metatexite			3,91	1,56	4,47	3,80	1,55	4,46	2900	1,2	1,1
B248[a]	Metatexite			3,53	1,47	3,57	3,44	1,46	3,56	2900	1,0	1,0
B249[a]	Metatexite			4,37	1,37	2,03	4,25	1,36	2,03	2900	1,0	1,0
B250[a]	Metatexite			3,45	2,41	6,49	3,36	2,39	6,48	2900	1,5	1,5
B252[a]	Metatexite			3,91	1,43	2,52	3,80	1,41	2,52	2900	1,0	1,0
Met_6	Orthogneiss	4557695,360	532764,670	5,26	6,38	13,57	5,12	6,33	13,54	2750	3,1	3,1

Met_9	Orthogneiss	4550090,600	442206,580	6,03	6,00	23,14	5,87	5,95	23,08	2750	3,8	3,7
Met_11	Orthogneiss	4552052,590	442613,400	4,93	4,96	18,33	4,79	4,92	18,28	2750	3,1	3,0
Met_13	Orthogneiss	4559368,140	513348,500	6,05	4,81	17,52	5,89	4,77	17,48	2750	3,1	3,0
Met_14	Orthogneiss	4562523,800	524170,940	5,86	6,93	13,74	5,71	6,87	13,71	2750	3,3	3,3
Met_15	Orthogneiss	4562526,940	524175,510	5,32	3,97	11,30	5,18	3,94	11,27	2750	2,3	2,3
Met_16	Orthogneiss	4492775,61	556126,8	6,64	4,43	17,03	6,47	4,40	16,98	2750	3,0	3,0
Met_17	Orthogneiss	4492780,19	553289,58	3,58	3,98	12,44	3,48	3,95	12,41	2750	2,3	2,2
Met_18	Orthogneiss	4493762,23	546091,74	6,08	9,92	37,91	5,91	9,84	37,82	2750	5,8	5,8
Met_19	Orthogneiss	4510232,65	560166,15	4,13	2,70	9,90	4,02	2,67	9,88	2750	1,8	1,8
Met_23_Ge*	Orthogneiss	4541102,38	516920,48	2,75	3,75	12,76	2,67	3,72	12,73	2750	2,1	2,1
2693[b]	Orthogneiss			4,98	2,75	17,30	4,84	2,72	17,25	2750	2,4	2,4
2694[b]	Orthogneiss			4,36	2,22	16,28	4,24	2,20	16,24	2750	2,1	2,1
2699[b]	Orthogneiss			4,55	4,96	21,37	4,43	4,92	21,31	2750	3,2	3,2
2710[b]	Orthogneiss			4,47	3,59	19,33	4,35	3,56	19,28	2750	2,7	2,7
2737[b]	Orthogneiss			4,82	9,19	19,33	4,69	9,12	19,28	2750	4,2	4,2
2738[b]	Orthogneiss			5,40	4,33	22,38	5,25	4,30	22,33	2750	3,2	3,2
2746[b]	Orthogneiss			3,66	10,14	21,37	3,56	10,06	21,31	2750	4,5	4,5
2750[b]	Orthogneiss			4,32	4,54	21,37	4,21	4,51	21,31	2750	3,1	3,1
2751[b]	Orthogneiss			4,73	4,33	18,31	4,61	4,30	18,27	2750	2,9	2,9
685[i]	Orthogneiss			4,12	10,56	17,30	4,01	10,48	17,25	2750	4,4	4,3
683[i]	Orthogneiss			4,26	11,61	10,17	4,15	11,52	10,15	2750	4,2	4,1
739[i]	Orthogneiss			4,19	0,00	16,28	4,08	0,00	16,24	2750	1,5	1,5
548[i]	Orthogneiss			4,91	4,22	8,14	4,78	4,19	8,12	2750	2,1	2,1
510[i]	Orthogneiss			5,18	7,39	11,19	5,05	7,33	11,16	2750	3,2	3,2
547[i]	Orthogneiss			4,57	8,45	9,16	4,45	8,38	9,13	2750	3,3	3,3
556[i]	Orthogneiss			5,17	10,56	6,10	5,04	10,48	6,09	2750	3,7	3,7
707[i]	Orthogneiss			4,96	9,50	0,00	4,83	9,43	0,00	2750	3,0	2,9

741^{i}	Orthogneiss	5,95	6,34	6,10	5,79	6,29	6,09	2750	2,7	2,6
744^{i}	Orthogneiss	4,72	0,00	5,09	4,60	0,00	5,07	2750	0,8	0,8
742^{i}	Orthogneiss	6,19	0,00	0,00	6,02	0,00	0,00	2750	0,6	0,6
555^{i}	Orthogneiss	4,94	8,45	7,12	4,81	8,38	7,10	2750	3,2	3,2
745^{i}	Orthogneiss	4,54	0,00	6,10	4,42	0,00	6,09	2750	0,9	0,9
738^{i}	Orthogneiss	5,72	0,00	0,00	5,56	0,00	0,00	2750	0,5	0,5
706^{i}	Orthogneiss	4,65	9,50	12,21	4,53	9,43	12,18	2750	3,8	3,8
551^{i}	Orthogneiss	5,21	11,61	0,00	5,07	11,52	0,00	2750	3,5	3,5
740^{i}	Orthogneiss	5,65	0,00	0,00	5,49	0,00	0,00	2750	0,5	0,5
587^{i}	Orthogneiss	4,62	10,56	14,24	4,50	10,48	14,21	2750	4,2	4,2
586^{i}	Orthogneiss	4,45	9,50	17,30	4,33	9,43	17,25	2750	4,1	4,1
589^{i}	Orthogneiss	5,10	4,22	9,16	4,97	4,19	9,13	2750	2,2	2,2
582^{i}	Orthogneiss	5,14	6,34	12,21	5,01	6,29	12,18	2750	3,0	3,0
584^{i}	Orthogneiss	4,68	10,56	7,12	4,56	10,48	7,10	2750	3,7	3,7
603^{i}	Orthogneiss	1,71	12,67	11,19	1,67	12,57	11,16	2750	4,3	4,2
515^{i}	Orthogneiss	4,54	5,28	20,35	4,42	5,24	20,30	2750	3,2	3,2
559^{i}	Orthogneiss	4,47	4,22	18,31	4,35	4,19	18,27	2750	2,8	2,8
732^{i}	Orthogneiss	4,19	0,00	16,28	4,08	0,00	16,24	2750	1,5	1,5
730^{i}	Orthogneiss	4,65	5,28	11,19	4,53	5,24	11,16	2750	2,6	2,6
733^{i}	Orthogneiss	4,39	0,00	10,17	4,27	0,00	10,15	2750	1,1	1,1
729^{i}	Orthogneiss	4,45	0,00	12,21	4,33	0,00	12,18	2750	1,3	1,3
726^{i}	Orthogneiss	4,04	0,00	17,30	3,93	0,00	17,25	2750	1,6	1,6
731^{i}	Orthogneiss	4,18	0,00	17,30	4,07	0,00	17,25	2750	1,6	1,6
728^{i}	Orthogneiss	4,61	7,39	28,49	4,49	7,33	28,42	2750	4,4	4,4
734^{i}	Orthogneiss	4,28	4,22	14,24	4,17	4,19	14,21	2750	2,5	2,5

737[i]	Orthogneiss			4,78	0,00	17,30	4,65	0,00	17,25	2750	1,7	1,7
736[i]	Orthogneiss			3,55	0,00	14,24	3,45	0,00	14,21	2750	1,3	1,3
560[i]	Orthogneiss			4,63	10,56	19,33	4,51	10,48	19,28	2750	4,6	4,5
Camp_12bar*	Granodiorite/Tonalite	4575803,7	545262,7				2,59	1,78	9,13	2750	1,4	1,4
BUD6	Granodiorite/Tonalite	4491498,920	519307,180				4,34	3,13	17,73	2750	2,5	2,5
BUD7	Granodiorite/Tonalite	4492305,630	520180,470				3,43	1,93	16,59	2750	2,0	2,0
BUD8	Granodiorite/Tonalite	4492451,000	520912,750				4,89	1,76	15,51	2750	2,0	2,0
Grt_24	Granodiorite/Tonalite	4492004,810	519415,650				3,57	3,05	17,32	2750	2,4	2,4
Grt_33	Granodiorite/Tonalite	4499240,460	526574,840				4,41	2,21	17,91	2750	2,3	2,3
Grt_34	Granodiorite/Tonalite	4492372,540	525457,800				6,10	5,40	21,34	2750	3,5	3,5
Grt_35	Granodiorite/Tonalite	4493408,070	528707,370				5,48	4,91	18,14	2750	3,1	3,1
Grt_37	Granodiorite/Tonalite	4492897,420	511284,950				3,55	1,69	8,53	2750	1,4	1,4
Grt_43	Granodiorite/Tonalite	4487335,150	515737,420				4,17	2,74	17,33	2750	2,4	2,3
Grt_52	Granodiorite/Tonalite	4499246,460	525671,430				4,33	3,02	17,83	2750	2,5	2,5
Grt_53	Granodiorite/Tonalite	4492455,420	510162,470				2,93	1,39	9,43	2750	1,3	1,3
Grt_61	Granodiorite/Tonalite	4560548,930	526675,420				3,41	2,29	7,36	2750	1,5	1,4
Grt_63_a	Granodiorite/Tonalite	4539653,020	489479,970				2,88	0,92	4,94	2750	0,9	0,9
Grt_63_b	Granodiorite/Tonalite	4539615,990	489465,900				3,09	1,03	10,79	2750	1,3	1,3
Grt_68	Granodiorite/Tonalite	4560649,370	524203,370				3,26	1,46	9,03	2750	1,3	1,3
Grt_108	Granodiorite/Tonalite	4547342,550	529153,530				4,02	2,60	13,36	2750	2,0	2,0
Grt_109	Granodiorite/Tonalite	4547250,420	529428,070				4,58	2,92	14,14	2750	2,2	2,2
Grt_110	Granodiorite/Tonalite	4547045,680	529425,110				3,94	2,02	12,88	2750	1,8	1,8
Grt_111	Granodiorite/Tonalite	4547041,600	529211,730				4,34	2,09	13,26	2750	1,9	1,9
Grt_193	Granodiorite/Tonalite	4560508,550	523974,510				2,61	2,53	7,92	2750	1,5	1,5
Grt_194	Granodiorite/Tonalite	4561358,340	524428,890				3,24	2,91	5,40	2750	1,5	1,5
Grt_195	Granodiorite/Tonalite	4561730,210	524192,690				3,09	3,83	7,50	2750	1,8	1,8
Grt_260	Granodiorite/Tonalite	4375461,83	466983,09				4,55	4,92	15,63	2750	2,8	2,8
Grt_263_Ge*	Granodiorite/Tonalite	4376894,31	465939,09				3,39	3,88	13,08	2750	2,3	2,3
Grt_264_Ge*	Granodiorite/Tonalite	4374704,14	462800,96				4,26	3,97	16,28	2750	2,6	2,6

Grt_265	Granodiorite/Tonalite	4375755,51	462169,49	4,17	4,84	15,76	2750	2,8	2,8
Grt_267	Granodiorite/Tonalite	4376373,52	465569,35	4,33	5,44	17,90	2750	3,1	3,1
Grt_282	Granodiorite/Tonalite	4541795,95	513540,93	3,99	2,47	13,28	2750	2,0	2,0
Grt_282_a_Ge*	Granodiorite/Tonalite	4541795,95	513540,93	3,49	2,48	10,97	2750	1,8	1,8
Grt_282_b_Ge*	Granodiorite/Tonalite	4541795,95	513540,93	3,33	2,00	11,94	2750	1,7	1,7
Grt_283	Granodiorite/Tonalite	4541732,98	513306,72	4,56	2,74	15,35	2750	2,3	2,2
Grt_283_b	Granodiorite/Tonalite	4541712,9	513317,35	4,23	3,54	12,13	2750	2,2	2,2
Grt_283_a_Ge*	Granodiorite/Tonalite	4541712,9	513317,35	3,50	3,17	11,21	2750	2,0	2,0
Grt_283_b_Ge*	Granodiorite/Tonalite	4541712,9	513317,35	3,31	3,52	12,99	2750	2,2	2,2
Grt_283_c_Ge*	Granodiorite/Tonalite	4541712,9	513317,35	3,52	2,06	10,59	2750	1,6	1,6
Grt_288	Granodiorite/Tonalite	4492480,09	519572,74	4,15	1,52	13,68	2750	1,8	1,8
Grt_289	Granodiorite/Tonalite	4492034,36	519431,85	3,10	1,60	14,72	2750	1,8	1,8
Grt_290	Granodiorite/Tonalite	4491980,94	519468,56	3,42	2,07	15,70	2750	2,0	2,0
Grt_291	Granodiorite/Tonalite	4491976,17	519439,56	3,58	2,04	16,54	2750	2,1	2,0
Grt_292	Granodiorite/Tonalite	4492005,17	519431,19	3,21	1,86	14,92	2750	1,9	1,8
Grt_293	Granodiorite/Tonalite	4492028,14	519410,01	3,14	2,21	15,00	2750	2,0	1,9
Grt_294	Granodiorite/Tonalite	4491976,41	519429,16	3,56	1,93	18,09	2750	2,1	2,1
Grt_295	Granodiorite/Tonalite	4492017,94	519418,08	3,12	1,48	14,82	2750	1,7	1,7
Grt_296	Granodiorite/Tonalite	4492017,26	519457,85	3,17	1,74	15,52	2750	1,9	1,9
Grt_297	Granodiorite/Tonalite	4492020,86	519452,62	3,14	1,90	15,08	2750	1,9	1,9
Grt_298	Granodiorite/Tonalite	4492012,92	519462,55	3,13	1,76	14,20	2750	1,8	1,8
Grt_299	Granodiorite/Tonalite	4491853,82	519262,71	4,03	2,12	16,23	2750	2,1	2,1
Grt_300	Granodiorite/Tonalite	4491862,77	519246,8	3,88	2,60	15,49	2750	2,2	2,1
Grt_301	Granodiorite/Tonalite	4491519,19	519395,99	4,08	2,49	16,01	2750	2,2	2,2
Grt_302	Granodiorite/Tonalite	4491500,4	519400,71	4,13	2,26	16,19	2750	2,1	2,1
Grt_372	Granodiorite/Tonalite	4372062,43	460286,78	5,22	4,92	15,96	2750	2,9	2,9
Grt_375	Granodiorite/Tonalite	4371300,3	468888,83	5,25	6,99	22,93	2750	4,0	3,9
Grt_392	Granodiorite/Tonalite	4544011,26	520824,91	3,56	3,22	9,92	2750	1,9	1,9
Grt_393	Granodiorite/Tonalite	4544349,7	518935,68	4,10	2,48	13,25	2750	2,0	2,0

Grt_394	Granodioritc/Tonalitc	4546486,65	518989,78	4,40	2,38	12,45	2750	1,9	1,9
Grt_398_Ge*	Granodiorite/Tonalite	4545177,94	518858,26	2,83	2,24	12,43	2750	1,7	1,7
Grt_399	Granodiorite/Tonalite	4544585,48	518827,64	3,54	2,93	10,31	2750	1,8	1,8
Grt_401_Ge*	Granodioritc/Tonalitc	4543215,6	517954,83	5,02	7,60	22,21	2750	4,1	4,0
Grt_422	Granodiorite/Tonalite	4534249,82	490741,23	3,02	3,12	11,02	2750	1,9	1,9
Grt_423	Granodioritc/Tonalitc	4535502,79	490981,43	1,91	2,61	5,30	2750	1,3	1,2
Grt_424	Granodiorite/Tonalite	4536958,89	493188,64	4,31	3,86	11,80	2750	2,3	2,3
Grt2	Monzogranite	4525178,9	503678,6	6,84	3,11	21,28	2750	3,0	3,0
Grt3	Monzogranite	4532172,4	504466,0	4,84	4,71	20,06	2750	3,1	3,1
Camp_9*	Monzogranite	4554126,0	521374,0	4,00	3,14	13,80	2750	2,2	2,2
BUD9	Monzogranitc	4491848,150	522581,870	4,53	2,33	16,59	2750	2,2	2,2
BUD10	Monzogranitc	4492260,970	523217,540	6,05	2,27	16,99	2750	2,4	2,4
BUD13	Monzogranite	4497400,250	526727,290	6,26	3,93	17,14	2750	2,9	2,8
GRT13	Monzogranitc	4524795,280	506383,560	6,46	5,32	20,86	2750	3,5	3,5
GRT21	Monzogranite	4535413,070	521366,650	5,51	4,25	20,03	2750	3,1	3,1
Grt_25	Monzogranite	4491501,920	520503,810	5,08	2,27	15,47	2750	2,2	2,2
Grt_26	Monzogranite	4491501,920	520503,810	5,87	2,81	18,35	2750	2,6	2,6
Grt_27	Monzogranite	4495515,860	522303,460	6,15	2,21	16,43	2750	2,3	2,3
Grt_28	Monzogranitc	4495515,860	522303,460	5,69	2,30	15,46	2750	2,3	2,2
Grt_30	Monzogranite	4497623,540	525330,740	6,18	3,29	16,33	2750	2,6	2,6
Grt_31	Monzogranite	4499358,970	541547,500	5,66	15,70	15,80	2750	5,8	5,8
Grt_32	Monzogranitc	4500404,940	540465,240	5,84	4,23	25,88	2750	3,5	3,5
Grt_41	Monzogranite	4488977,440	513193,230	6,07	5,25	21,74	2750	3,5	3,5
Grt_42	Monzogranite	4489133,520	513444,440	5,79	6,01	21,69	2750	3,7	3,7
Grt_45	Monzogranite	4489709,430	526225,880	6,25	5,26	18,20	2750	3,3	3,3
Grt_46	Monzogranite	4489831,520	526227,170	6,44	4,82	17,99	2750	3,2	3,1
Grt_47	Monzogranitc	4490921,820	527387,190	5,57	4,01	19,97	2750	3,0	3,0
Grt_48	Monzogranite	4490964,450	529505,770	5,84	4,17	18,76	2750	3,0	3,0
Grt_49	Monzogranite	4491095,220	531195,200	5,57	6,06	24,96	2750	3,9	3,9

Grt_50	Monzogranite	4492138,790	530410,880	6,07	5,69	28,27	2750	4,1	4,1
Grt_54	Monzogranite	4534590,520	507652,440	5,28	4,08	17,55	2750	2,8	2,8
Grt_57	Monzogranite	4552150,950	520503,660	5,05	3,05	15,27	2750	2,4	2,4
Grt_58	Monzogranite	4552488,760	520003,140	4,57	2,28	14,25	2750	2,1	2,0
Grt_59	Monzogranite	4554018,920	520379,250	5,29	2,98	14,64	2750	2,3	2,3
Grt_60	Monzogranite	4553318,470	519428,640	5,69	4,31	16,48	2750	2,9	2,8
Grt_65_a	Monzogranite	4556322,340	512839,030	2,55	1,56	20,03	2750	2,1	2,1
Grt_65_b	Monzogranite	4556322,340	512839,030	2,35	0,67	15,44	2750	1,5	1,5
Grt_65_c	Monzogranite	4556322,340	512839,030	2,35	0,72	15,40	2750	1,5	1,5
Grt_83	Monzogranite	4532001,250	506527,080	4,50	4,26	16,94	2750	2,8	2,7
Grt_84	Monzogranite	4533395,720	505109,530	4,77	3,79	18,84	2750	2,8	2,8
Grt_85	Monzogranite	4534395,000	501861,630	5,85	5,02	21,44	2750	3,4	3,4
Grt_86	Monzogranite	4535156,970	502073,480	5,00	3,29	18,35	2750	2,7	2,6
Grt_91	Monzogranite	4541614,620	508345,800	5,48	5,61	22,68	2750	3,6	3,6
Grt_92	Monzogranite	4545206,820	509549,620	6,78	12,16	15,47	2750	5,0	4,9
Grt_93	Monzogranite	4552359,300	506384,240	5,36	2,23	20,27	2750	2,5	2,5
Grt_94	Monzogranite	4553968,280	504252,590	5,92	4,42	19,63	2750	3,1	3,1
Grt_95	Monzogranite	4553971,250	504081,710	5,79	4,52	22,28	2750	3,3	3,3
Grt_96	Monzogranite	4553973,360	504057,990	5,17	3,66	20,08	2750	2,9	2,9
Grt_99	Monzogranite	4529630,480	517020,960	5,89	7,04	20,98	2750	3,9	3,9
Grt_101	Monzogranite	4548739,010	525121,870	4,50	2,25	12,19	2750	1,9	1,9
Grt_102	Monzogranite	4548232,970	522466,430	4,90	2,33	14,30	2750	2,1	2,1
Grt_103	Monzogranite	4557778,900	522422,100	5,31	3,90	15,36	2750	2,6	2,6
Grt_105	Monzogranite	4559325,090	518662,820	6,20	5,00	18,89	2750	3,3	3,2
Grt_106	Monzogranite	4560121,610	518121,260	5,69	5,17	19,98	2750	3,3	3,3
Grt_107	Monzogranite	4560909,510	516297,580	5,34	4,72	17,41	2750	3,0	3,0
Grt_116	Monzogranite	4554154,760	532207,650	5,14	3,09	13,67	2750	2,3	2,3
Grt_119	Monzogranite	4549084,940	532936,780	4,88	2,54	14,04	2750	2,1	2,1
Grt_120	Monzogranite	4548817,110	526914,640	4,70	2,82	14,02	2750	2,2	2,2

Grt_123	Monzogranite	4541907,810	506070,210		5,59	6,65	29,76	2750	4,4	4,4
Grt_124	Monzogranite	4543878,630	504546,900		5,27	6,50	26,74	2750	4,1	4,1
Grt_125	Monzogranite	4546384,510	510000,720		5,47	4,83	19,28	2750	3,2	3,1
Grt_126	Monzogranite	4544379,900	507316,980		5,72	4,40	21,05	2750	3,2	3,2
Grt_127	Monzogranite	4544789,340	509408,460		5,15	4,40	18,09	2750	2,9	2,9
Grt_128	Monzogranite	4547770,020	508926,530		5,70	6,37	16,30	2750	3,4	3,4
Grt_137	Monzogranite	4532244,400	525602,860		4,93	5,45	18,55	2750	3,2	3,2
Grt_138	Monzogranite	4531692,450	530361,130		4,42	5,36	17,14	2750	3,1	3,0
Grt_139	Monzogranite	4528937,000	532113,060		2,93	5,72	16,57	2750	3,0	2,9
Grt_141	Monzogranite	4524301,520	529501,040		4,11	3,34	16,21	2750	2,4	2,4
Grt_143	Monzogranite	4525416,250	528536,280		4,85	5,55	16,60	2750	3,1	3,1
Grt_145	Monzogranite	4528235,750	533322,320		3,74	4,52	14,81	2750	2,6	2,6
Grt_146	Monzogranite	4529142,590	539867,050		4,51	4,11	18,02	2750	2,8	2,8
Grt_147	Monzogranite	4527415,470	542041,980		4,44	4,94	16,65	2750	2,9	2,9
Grt_153	Monzogranite	4531632,610	531189,740		5,08	4,89	19,21	2750	3,1	3,1
Grt_154	Monzogranite	4531783,700	532059,780		6,55	5,22	23,41	2750	3,7	3,6
Grt_155	Monzogranite	4533842,720	533887,600		4,54	4,97	14,18	2750	2,8	2,7
Grt_156	Monzogranite	4533529,700	535064,790		6,08	4,82	15,93	2750	3,0	3,0
Grt_157	Monzogranite	4533951,890	544886,460		6,30	4,21	16,60	2750	2,9	2,9
Grt_161	Monzogranite	4554170,120	521325,860		4,91	3,54	14,43	2750	2,4	2,4
Grt_162	Monzogranite	4544383,490	536669,630		6,56	5,61	18,80	2750	3,5	3,4
Grt_166	Monzogranite	4541773,700	536171,780		5,33	4,62	14,69	2750	2,8	2,8
Grt_167	Monzogranite	4528411,490	512340,340		3,25	3,05	12,73	2750	2,0	2,0
Grt_169	Monzogranite	4527180,090	508685,280		4,88	3,71	18,31	2750	2,8	2,7
Grt_175	Monzogranite	4532254,460	523165,000		4,91	5,09	21,61	2750	3,4	3,3
Grt_176	Monzogranite	4531601,500	522425,330		4,93	5,81	21,12	2750	3,5	3,5
Grt_177	Monzogranite	4532296,880	517912,070		4,11	6,54	15,88	2750	3,2	3,2
Grt_183	Monzogranite	4538122,180	529349,770		6,37	4,60	16,32	2750	3,0	3,0
Grt_192	Monzogranite	4559679,340	513583,400		4,24	5,13	14,80	2750	2,8	2,8

Grt_196	Monzogranite	4550119,45	504479,47	5,97	3,79	20,27	2750	3,0	3,0
Grt_197	Monzogranite	4552645,74	506309,36	3,61	3,64	11,91	2750	2,2	2,1
Grt_198	Monzogranite	4553066,15	509531,78	4,93	4,87	14,99	2750	2,8	2,8
Grt_200	Monzogranite	4557939,69	514259,36	3,98	1,65	13,46	2750	1,8	1,8
Grt_204	Monzogranite	4551647,9	529057,58	5,25	3,12	16,81	2750	2,5	2,5
Grt_205	Monzogranite	4551783	528731,19	5,02	3,30	15,01	2750	2,4	2,4
Grt_206	Monzogranite	4551454,47	527311,98	5,81	3,61	16,47	2750	2,7	2,7
Grt_207	Monzogranite	4550173,79	525747,98	4,42	3,52	11,82	2750	2,2	2,2
Grt_208	Monzogranite	4550127,39	522669,73	3,94	2,89	11,69	2750	2,0	2,0
Grt_217	Monzogranite	4525952,36	539770,11	3,85	5,28	14,21	2750	2,8	2,8
Grt_231_Ge*	Monzogranite	4531862,42	533673.26	4,95	4,69	25,10	2750	3,5	3,5
Grt_232_Ge*	Monzogranite	4532083,03	533819,31	4,66	6,44	23,72	2750	3,8	3,8
Grt_233_Ge*	Monzogranite	4532432,96	533960,57	5,05	7,31	28,59	2750	4,4	4,4
Grt_236_Ge*	Monzogranite	4532385,11	532484,28	4,78	5,07	34,63	2750	4,3	4,2
Grt_239_Ge*	Monzogranite	4527235,78	505366,27	4,66	1,90	14,19	2750	2,0	1,9
Grt_243	Monzogranite	4531250,57	515059,63	3,42	2,79	13,29	2750	2,0	2,0
Grt_244	Monzogranite	4535524,05	4531250,57	4,67	3,75	17,34	2750	2,7	2,6
Grt_251_Ge*	Monzogranite	4540411,26	507683,05	4,97	8,14	23,88	2750	4,3	4,3
Grt_252_Ge*	Monzogranite	4543345,48	508966,05	5,75	5,27	23,04	2750	3,6	3,6
Grt_253	Monzogranite	4545028,96	510466,7	6,41	4,11	25,28	2750	3,5	3,5
Grt_254_Ge*	Monzogranite	4544766,21	511974,82	4,95	5,09	23,17	2750	3,5	3,4
Grt_255_Ge*	Monzogranite	4545185,76	512189,62	4,83	6,15	21,00	2750	3,6	3,6
Grt_256_Ge*	Monzogranite	4545511,78	512715,97	3,99	3,04	13,14	2750	2,1	2,1
Grt_257	Monzogranite	4545832,78	514794,96	5,05	3,67	14,49	2750	2,5	2,5
Grt_272	Monzogranite	4528492,74	508070,86	4,62	2,80	15,45	2750	2,3	2,3
Grt_304	Monzogranite	4492220,59	522081,46	5,70	2,71	15,30	2750	2,4	2,3
Grt_305	Monzogranite	4492377,29	522169,42	6,91	3,35	13,95	2750	2,5	2,5
Grt_318	Monzogranite	4491253,08	521807,48	6,61	2,25	16,07	2750	2,4	2,4
Grt_319	Monzogranite	4492006,16	522485,93	4,94	2,20	16,51	2750	2,2	2,2

Grt_320	Monzogranite	4491981,09	522479,71	4,61	3,03	16,34	2750	2,4	2,4
Grt_321	Monzogranite	4491995,03	522471,87	5,20	1,88	18,88	2750	2,3	2,3
Grt_322	Monzogranite	4491988,55	522492,9	5,09	2,63	15,78	2750	2,3	2,3
Grt_323	Monzogranite	4492037,48	522482,59	4,91	2,25	15,48	2750	2,2	2,1
Grt_324	Monzogranite	4492272,96	523143,01	4,99	2,54	16,42	2750	2,3	2,3
Grt_325	Monzogranite	4492273,99	523150,34	4,98	2,51	16,34	2750	2,3	2,3
Grt_326	Monzogranite	4492274,86	523156,12	4,72	2,63	17,06	2750	2,4	2,3
Grt_327	Monzogranite	4492273,62	523147,38	4,78	2,20	18,10	2750	2,3	2,3
Grt_328	Monzogranite	4492271,16	523136,09	4,62	2,62	15,16	2750	2,2	2,2
Grt_405_Ge*	Monzogranite	4550121,07	520258,26	3,24	2,27	12,73	2750	1,8	1,8
Grt_406	Monzogranite	4550455,66	517894,15	4,82	2,29	14,39	2750	2,1	2,1
Grt_407	Monzogranite	4548806,59	516465,05	4,84	4,71	14,56	2750	2,7	2,7
Grt_408	Monzogranite	4530269,26	507783,01	4,44	2,48	17,92	2750	2,4	2,3
Grt_4	Leucogranite	4531574,0	504748,4	6,43	8,82	28,94	2750	5,0	5,0
Camp_8g*	Leucogranite	4539392,7	533335,3	4,71	4,51	23,14	2750	3,3	3,3
Camp_8b*	Leucogranite	4537737,3	532913,9	4,95	2,72	15,63	2750	2,3	2,3
Bud_11	Leucogranite	4496599,880	523666,240	6,13	2,94	13,56	2750	2,3	2,3
Bud_12	Leucogranite	4497040,840	524383,460	6,07	4,66	16,66	2750	3,0	3,0
Bud_14	Leucogranite	4499878,340	532465,220	5,11	2,35	16,13	2750	2,3	2,2
Bud15	Leucogranite	4501657,650	532880,430	5,19	4,96	12,39	2750	2,7	2,7
Grt_17	Leucogranite	4536354,320	531180,470	6,06	5,50	15,83	2750	3,2	3,1
Grt_18	Leucogranite	4539423,690	533403,140	6,67	7,20	21,17	2750	4,0	4,0
Grt_23	Leucogranite	4494369,190	502681,960	6,69	12,83	7,55	2750	4,6	4,5
Grt_38	Leucogranite	4493196,920	512558,850	5,98	9,30	29,73	2750	5,1	5,1
Grt_39	Leucogranite	4493190,540	512663,880	6,11	6,71	27,76	2750	4,3	4,3
Grt_40	Leucogranite	4493488,930	513013,260	6,51	12,88	38,23	2750	6,7	6,7
Grt_51	Leucogranite	4496557,740	523798,830	5,58	3,31	12,53	2750	2,3	2,3
Grt_77	Leucogranite	4546474,550	542666,880	5,72	6,08	21,02	2750	3,6	3,6
Grt_98	Leucogranite	4529547,600	517114,490	6,45	9,71	31,23	2750	5,4	5,4

Grt_112	Leucogranite	4549358,000	535711,430	6,51	4,73	22,11	2750	3,4	3,4
Grt_113	Leucogranite	4552271,800	536700,040	6,01	5,99	21,00	2750	3,7	3,6
Grt_115	Leucogranite	4556200,800	533133,330	6,25	5,81	21,55	2750	3,7	3,6
Grt_121	Leucogranite	4537007,740	510159,130	6,12	3,74	23,13	2750	3,2	3,2
Grt_122	Leucogranite	4537762,650	508256,240	5,69	2,19	18,26	2750	2,4	2,4
Grt_151	Leucogranite	4532378,160	529823,470	5,45	6,15	29,95	2750	4,3	4,2
Grt_152	Leucogranite	4533661,580	529844,190	6,28	6,28	31,45	2750	4,5	4,5
Grt_158	Leucogranite	4538954,250	538684,090	6,14	7,81	18,92	2750	4,0	4,0
Grt_160	Leucogranite	4554473,190	518714,090	5,36	7,74	20,75	2750	4,0	4,0
Grt_163	Leucogranite	4544033,840	540018,130	5,49	7,50	23,88	2750	4,2	4,2
Grt_164	Leucogranite	4543891,770	539992,170	6,53	8,36	19,25	2750	4,2	4,2
Grt_165	Leucogranite	4543639,920	540316,870	5,86	6,45	21,01	2750	3,8	3,7
Grt_171	Leucogranite	4539661,300	532616,990	5,32	3,30	16,97	2750	2,6	2,6
Grt_172	Leucogranite	4539240,770	533159,340	5,63	4,15	22,27	2750	3,2	3,2
Grt_174	Leucogranite	4537519,160	532776,880	5,93	5,43	17,11	2750	3,2	3,2
Grt_184	Leucogranite	4536848,650	530249,170	5,83	3,06	16,61	2750	2,6	2,5
Grt_185	Leucogranite	4537898,570	531578,770	5,35	2,71	11,48	2750	2,1	2,0
Grt_186	Leucogranite	4538156,260	533589,100	5,70	2,91	17,72	2750	2,6	2,6
Grt_187	Leucogranite	4537816,960	534551,720	6,02	2,67	17,46	2750	2,5	2,5
Grt_188	Leucogranite	4534890,770	534229,870	4,18	4,93	14,58	2750	2,7	2,7
Grt_189	Leucogranite	4535487,860	532298,650	6,38	2,21	18,00	2750	2,5	2,5
Grt_190	Leucogranite	4534791,140	531486,060	5,45	7,74	31,21	2750	4,8	4,7
Grt_191	Leucogranite	4534099,000	530474,160	5,41	4,66	31,03	2750	4,0	3,9
Grt_201	Leucogranite	4557496,68	516074,81	5,48	4,87	21,57	2750	3,3	3,3
Grt_202	Leucogranite	4556971,85	530684,09	5,23	6,22	18,92	2750	3,5	3,5
Grt_230_Ge*	Leucogranite	4522686,01	534904,72	2,19	2,45	12,89	2750	1,8	1,8
Grt_234_Ge*	Leucogranite	4532721,98	533985	5,67	8,60	22,44	2750	4,4	4,4
Grt_235_Ge*	Leucogranite	4533261,22	532745,02	4,64	5,01	25,71	2750	3,6	3,6
Grt_261	Leucogranite	4375452,75	467022,93	6,19	8,39	16,44	2750	4,0	3,9

Grt_262	Leucogranite	4375639	467447,94	5,98	6,56	16,15	2750	3,5	3,4
Grt_268	Leucogranite	4375369,98	468240,02	7,07	6,38	22,61	2750	4,0	3,9
Grt_269_Gc*	Leucogranite	4375248,93	468261,71	4,96	6,42	16,68	2750	3,4	3,3
Grt_287	Leucogranite	4494632,89	519717,08	5,73	7,07	32,48	2750	4,7	4,7
Grt_306	Leucogranite	4496830,98	524024,87	5,41	2,35	14,70	2750	2,2	2,2
Grt_307	Leucogranite	4496833,37	523993,5	5,46	2,22	12,99	2750	2,0	2,0
Grt_308	Leucogranite	4496887,99	523994,24	5,24	3,03	14,93	2750	2,4	2,3
Grt_309	Leucogranite	4496883,32	523986,48	5,86	2,71	16,65	2750	2,5	2,4
Grt_310	Leucogranite	4496874,77	523978,96	6,05	3,49	12,75	2750	2,4	2,4
Grt_311	Leucogranite	4496872.43	523989,45	5,94	3,31	16,43	2750	2,6	2,6
Grt_312	Leucogranite	4496880,68	523996,24	5,97	3,54	11,84	2750	2,4	2,3
Grt_313	Leucogranite	4496888,47	524001,73	5,70	3,05	16,19	2750	2,5	2,5
Grt_314	Leucogranite	4496879,64	524003,79	5,58	2,91	15,41	2750	2,4	2,4
Grt_315	Leucogranite	4496876,44	523999,31	5,40	3,56	14,47	2750	2,5	2,5
Grt_316	Leucogranite	4497218,92	524224,18	5,44	2,38	17,99	2750	2,4	2,4
Grt_317	Leucogranite	4497200,67	524254,86	5,43	4,35	16,24	2750	2,8	2,8
Grt_329	Leucogranite	4496706,16	523646,15	5,57	3,56	11,92	2750	2,3	2,3
Grt_330	Leucogranite	4496696,43	523660,13	5,83	3,97	12,59	2750	2,5	2,5
Grt_331	Leucogranite	4496585,35	523656,04	5,54	3,57	12,76	2750	2,4	2,4
Grt_332	Leucogranite	4496589,24	523654,84	5,58	3,47	12,62	2750	2,4	2,3
Grt_333	Leucogranite	4496524,18	523647,6	5,14	3,88	11,77	2750	2,4	2,3
Grt_334	Leucogranite	4496499,11	523645,04	5,24	3,14	11,62	2750	2,2	2,1
Grt_356	Leucogranite	4537025,7	530307,84	7,16	3,77	22,82	2750	3,3	3,3
Grt_357	Leucogranite	4537547,5	532906,56	5,79	3,18	17,01	2750	2,6	2,6
Grt_358	Leucogranite	4537767,71	533060,35	6,19	3,08	17,56	2750	2,7	2,6
Grt_359	Leucogranite	4537761,24	533067,62	6,47	2,82	17,84	2750	2,6	2,6
Grt_360	Leucogranite	4537775,75	533036,96	6,17	2,94	16,56	2750	2,6	2,5
Grt_361	Leucogranite	4537818,45	532968,38	5,46	2,17	15,04	2750	2,2	2,2
Grt_362	Leucogranite	4537806,69	532960,06	6,23	2,37	17,04	2750	2,4	2,4

Grt_363	Leucogranite	4537796,12	532954,68				6,22	2,22	17,25	2750	2,4	2,4
Grt_364	Leucogranite	4537774,16	532915				6,50	2,13	17,94	2750	2,5	2,4
Grt_365	Leucogranite	4537766,54	532921,29				6,47	2,31	18,02	2750	2,5	2,5
Grt_366	Leucogranite	4539015,22	534384,71				5,84	8,06	21,47	2750	4,2	4,2
Grt_367	Leucogranite	4540860,78	537442,67				6,66	6,90	22,33	2750	4,1	4,0
Grt_367_Ge*	Leucogranite	4540860,78	537442,67				4,77	4,44	15,41	2750	2,7	2,7
Grt_368	Leucogranite	4539869,47	537753,72				5,70	9,00	20,22	2750	4,4	4,3
Grt_369	Leucogranite	4372984,25	467241,04				5,34	6,53	10,60	2750	3,0	3,0
Grt_370_Ge*	Leucogranite	4373655,54	466718,45				4,57	2,75	9,88	2750	1,9	1,9
Grt_371	Leucogranite	4372797,16	465217,03				5,52	5,01	11,18	2750	2,7	2,6
Grt_373_Ge*	Leucogranite	4372285,87	462268,36				4,37	4,95	9,87	2750	2,4	2,4
Grt_374	Leucogranite	4370558	461474,08				5,80	6,69	15,16	2750	3,4	3,4
Grt_400	Leucogranite	4544169,51	517419,94				5,37	8,97	20,98	2750	4,4	4,3
Grt_402	Leucogranite	4543301,95	518216,99				5,70	5,27	22,07	2750	3,5	3,5
H313^{c}	Amphibolite			0,27	0,74	0,81	0,26	0,73	0,81	3300	0,3	0,3
H162^{c}	Amphibolite			0,86	0,84	2,14	0,84	0,84	2,13	3300	0,5	0,5
H45^{c}	Amphibolite			0,75	0,63	0,61	0,73	0,63	0,61	3300	0,3	0,3
S306^{c}	Amphibolite			0,39	0,53	1,63	0,38	0,52	1,62	3300	0,3	0,3
MP18^{d}	Amphibolite			0,61	1,99	8,20	0,59	1,97	8,18	3300	1,4	1,4
MP2^{d}	Amphibolite			0,62	1,33	2,96	0,60	1,32	2,95	3300	0,7	0,7
MP3^{d}	Amphibolite			0,69	3,95	4,24	0,67	3,92	4,23	3300	1,7	1,7
ML13^{d}	Amphibolite			0,82	0,95	2,52	0,80	0,94	2,52	3300	0,6	0,6
ML14^{d}	Amphibolite			0,76	1,05	2,20	0,74	1,04	2,19	3300	0,6	0,6
ML47^{d}	Amphibolite			0,62	0,60	0,27	0,60	0,60	0,27	3300	0,3	0,3
ML49^{d}	Amphibolite			0,62	0,54	0,26	0,60	0,53	0,26	3300	0,3	0,3
MP20^{d}	Amphibolite			0,59	0,57	1,53	0,58	0,57	1,52	3300	0,4	0,4
E24B^{d}	Amphibolite			1,08	0,40	1,12	1,05	0,40	1,12	3300	0,3	0,3

MP22[d]	Amphibolite	0,38	1,20	2,39	0,37	1,19	2,39	3300	0,6	0,6
MP4[d]	Amphibolite	1,27	0,45	1,36	1,24	0,45	1,36	3300	0,4	0,4
MP8[d]	Amphibolite	0,74	0,12	0,27	0,72	0,12	0,27	3300	0,1	0,1
MP17[d]	Amphibolite	0,63	1,30	2,97	0,61	1,29	2,96	3300	0,7	0,7
MP15[d]	Amphibolite	0,57	1,80	2,82	0,55	1,78	2,81	3300	0,9	0,9
MP19[d]	Amphibolite	0,92	0,00	0,13	0,90	0,00	0,13	3300	0,1	0,1
MP14[d]	Amphibolite	0,24	0,07	1,41	0,24	0,07	1,41	3300	0,2	0,2
MP16[d]	Amphibolite	0,36	0,35	1,59	0,35	0,35	1,58	3300	0,3	0,3
MP13[d]	Amphibolite	0,27	0,03	0,30	0,26	0,03	0,29	3300	0,1	0,1
MP21[d]	Amphibolite	0,39	0,06	0,28	0,38	0,06	0,28	3300	0,1	0,1
MP5[d]	Amphibolite	0,45	0,00	0,21	0,44	0,00	0,21	3300	0,1	0,1
AA-274[m]	Amphibolite	0,54	0,53	1,83	0,53	0,52	1,83	3300	0,4	0,4
AA-364[m]	Amphibolite	0,71	0,32	1,02	0,69	0,31	1,01	3300	0,3	0,3
AA-367[m]	Amphibolite	0,57	0,21	0,41	0,56	0,21	0,41	3300	0,2	0,2
AA-9B[m]	Amphibolite	0,77	0,32	0,61	0,75	0,31	0,61	3300	0,2	0,2
AA-9A[m]	Amphibolite	1,38	0,32	0,61	1,35	0,31	0,61	3300	0,3	0,3
BCA-1C[m]	Amphibolite	0,78	0,42	1,42	0,76	0,42	1,42	3300	0,3	0,3
BCA-1D[m]	Amphibolite	0,75	0,63	1,22	0,73	0,63	1,22	3300	0,4	0,4
BCA-2B[m]	Amphibolite	0,48	0,42	1,12	0,47	0,42	1,12	3300	0,3	0,3
CA-2[m]	Amphibolite	0,71	0,32	0,41	0,69	0,31	0,41	3300	0,2	0,2
CM-1[m]	Amphibolite	1,52	0,84	3,66	1,48	0,84	3,65	3300	0,7	0,7
CM-2[m]	Amphibolite	0,33	0,21	0,51	0,32	0,21	0,51	3300	0,1	0,1
CM-4[m]	Amphibolite	0,48	0,21	0,41	0,47	0,21	0,41	3300	0,2	0,2
CM-5b[m]	Amphibolite	0,46	0,11	0,51	0,45	0,10	0,51	3300	0,1	0,1
CM-7B[m]	Amphibolite	0,21	0,00	0,10	0,20	0,00	0,10	3300	0,0	0,0

CPR-2^{m}	Amphibolite	0,73	2,32	6,61	0,71	2,30	6,60	3300	1,4	1,4
CPR-12^{m}	Amphibolite	1,63	0,42	0,92	1,59	0,42	0,91	3300	0,4	0,4
CPR-14^{m}	Amphibolite	0,60	0,95	2,85	0,59	0,94	2,84	3300	0,6	0,6
AA-217^{m}	Amphibolite	1,00	0,63	0,41	0,98	0,63	0,41	3300	0,3	0,3
PC-1^{m}	Amphibolite	0,30	0,21	0,31	0,29	0,21	0,30	3300	0,1	0,1
PC-4^{m}	Amphibolite	0,68	0,53	1,32	0,66	0,52	1,32	3300	0,4	0,4
PC-5^{m}	Amphibolite	0,40	0,32	0,71	0,39	0,31	0,71	3300	0,2	0,2

LOWER CRUST (LAYER 3)

Samples label	Rock type	Location		K_{350Ma} (%)	cU_{350Ma} (ppm)	cTh_{350Ma} (ppm)	K_{300Ma} (%)	cU_{300Ma} (ppm)	cTh_{300Ma} (ppm)	ρ (Kg m^{-3})	H_{350Ma} (μW m^{-3})	H_{300Ma} (μW m^{-3})
		N (UTM-WGS84)	E (UTM-WGS 84)									
MN_02*	Eclogite	4536065,5	539214,3	0,11	0,46	0,92	0,11	0,46	0,91	3300	0,2	0,2
PB-03*	Eclogite	4559124,1	513449,5	1,54	2,71	5,64	1,50	2,69	5,62	3300	1,5	1,5
H212^{e}	Eclogite			0,19	0,74	0,41	0,19	0,73	0,41	3300	0,3	0,3
H213^{e}	Eclogite			0,02	0,63	0,41	0,02	0,63	0,41	3300	0,2	0,2
H342^{e}	Eclogite			0,04	0,63	0,31	0,04	0,63	0,30	3300	0,2	0,2
H92^{e}	Eclogite			0,00	0,11	0,10	0,00	0,10	0,10	3300	0,0	0,0
Gran_4	Felsic Granulite	4685191,09	517357,57	2,29	1,18	11,68	2,23	1,18	11,65	2900	1,4	1,4
Gran_5	Felsic Granulite	4685202,25	517352,04	2,40	1,07	15,55	2,34	1,06	15,51	2900	1,7	1,7
SL20^{e}	Felsic Granulite			1,61	0,32	7,15	1,57	0,31	7,14	2900	0,8	0,8
SL21^{e}	Felsic Granulite			1,85	0,53	8,66	1,80	0,52	8,64	2900	1,0	1,0
SL22^{e}	Felsic Granulite			1,40	0,63	16,18	1,37	0,63	16,14	2900	1,5	1,5
Popp-D^{f}	Felsic granulite			4,67	2,32	2,14	4,55	2,30	2,13	2900	1,3	1,3
Popp-L^{f}	Felsic granulite			5,42	3,06	2,85	5,28	3,04	2,84	2900	1,6	1,6

Ost-L[f]	Felsic granulite	3,84	2,43	2,65	3,73	2,41	2,64	2900	1,3	1,2
St[f]	Felsic granulite	4,35	2,85	3,76	4,23	2,83	3,76	2900	1,5	1,5
Du[f]	Felsic granulite	2,87	0,00	0,00	2,79	0,00	0,00	2900	0,3	0,3
Ysp-D[f]	Felsic granulite	4,47	5,49	3,26	4,35	5,45	3,25	2900	2,2	2,2
Ysp-L[f]	Felsic granulite	5,00	3,17	0,00	4,86	3,14	0,00	2900	1,4	1,4
1059[f]	Felsic granulite	2,37	4,01	5,09	2,31	3,98	5,07	2900	1,7	1,7
1062[f]	Felsic granulite	4,08	1,69	3,87	3,97	1,68	3,86	2900	1,2	1,1
1064[f]	Felsic granulite	3,15	1,06	0,00	3,06	1,05	0,00	2900	0,6	0,6
1074[f]	Felsic granulite	4,87	3,17	3,46	4,74	3,14	3,45	2900	1,6	1,6
1076[f]	Felsic granulite	4,96	2,32	2,44	4,83	2,30	2,44	2900	1,3	1,3
1078[f]	Felsic granulite	4,33	2,85	5,70	4,22	2,83	5,68	2900	1,6	1,6
BD160a[g]	Felsic granulite	5,23	0,42	1,02	5,09	0,42	1,01	2900	0,7	0,7
1060[g]	Felsic granulite	3,89	3,17	4,07	3,78	3,14	4,06	2900	1,6	1,6
1061[g]	Felsic granulite	4,01	3,17	8,14	3,90	3,14	8,12	2900	1,9	1,9
1063[g]	Felsic granulite	3,66	3,17	0,00	3,56	3,14	0,00	2900	1,2	1,2
1065[g]	Felsic granulite	4,10	3,17	2,03	3,99	3,14	2,03	2900	1,4	1,4
1066[g]	Felsic granulite	2,19	3,17	2,03	2,13	3,14	2,03	2900	1,2	1,2
1067[g]	Felsic Granulite	1,55	0,00	2,03	1,51	0,00	2,03	2900	0,3	0,3
1068[g]	Felsic Granulite	3,07	4,22	21,37	2,99	4,19	21,31	2900	3,1	3,0
1069[g]	Felsic Granulite	2,15	4,22	0,00	2,10	4,19	0,00	2900	1,4	1,4
1070[g]	Felsic Granulite	3,38	4,22	0,00	3,29	4,19	0,00	2900	1,5	1,5
1071[g]	Felsic Granulite	3,07	3,17	0,00	2,99	3,14	0,00	2900	1,2	1,2
1072[g]	Felsic Granulite	4,61	1,06	0,00	4,49	1,05	0,00	2900	0,8	0,7
1075[g]	Felsic Granulite	4,29	2,11	1,02	4,17	2,10	1,01	2900	1,1	1,1
1077[g]	Felsic Granulite	4,35	2,11	1,02	4,23	2,10	1,01	2900	1,1	1,1

1079[g]	Felsic Granulite			2,34	1,06	0,00	2,27	1,05	0,00	2900	0,5	0,5
1080[g]	Felsic Granulite			4,18	0,00	2,03	4,06	0,00	2,03	2900	0,6	0,6
U-141[l]	Felsic Granulite			2,27	0,00	10,17	2,21	0,00	10,15	2900	1,0	1,0
U-50[l]	Felsic Granulite			4,99	0,00	8,14	4,86	0,00	8,12	2900	1,1	1,1
U-152[l]	Felsic Granulite			4,45	0,88	8,14	4,33	0,87	8,12	2900	1,3	1,3
U-49[l]	Felsic Granulite			3,32	0,00	4,07	3,23	0,00	4,06	2900	0,6	0,6
U-156[l]	Felsic Granulite			2,77	1,11	13,23	2,69	1,10	13,19	2900	1,6	1,6
U-155[l]	Felsic Granulite			2,10	0,32	2,03	2,04	0,31	2,03	2900	0,5	0,4
U-157[l]	Felsic Granulite			2,47	0,30	3,05	2,40	0,29	3,04	2900	0,6	0,5
U-145[l]	Felsic Granulite			2,94	0,41	2,03	2,86	0,41	2,03	2900	0,6	0,6
U-92[l]	Felsic Granulite			3,39	0,00	0,00	3,30	0,00	0,00	2900	0,3	0,3
U-147[l]	Felsic Granulite			4,03	0,00	0,00	3,92	0,00	0,00	2900	0,4	0,4
U-146[l]	Felsic Granulite			5,02	0,13	1,02	4,89	0,13	1,01	2900	0,6	0,6
U-93[l]	Felsic Granulite			4,21	0,00	3,05	4,10	0,00	3,04	2900	0,7	0,6
U-153[l]	Felsic Granulite			1,72	0,31	5,09	1,68	0,30	5,07	2900	0,6	0,6
U-96[l]	Felsic Granulite			3,43	0,00	22,38	3,34	0,00	22,33	2900	2,0	2,0
SL_1_Ge[*]	Mafic Granulite	4685187,57	517359,43	0,91	0,22	0,71	0,88	0,22	0,71	2900	0,2	0,2
SL_2_Ge[*]	Mafic Granulite	4685187,57	517359,43	3,06	0,40	2,44	2,98	0,40	2,44	2900	0,6	0,6
Gran_1	Mafic Granulite	4685148,55	517371,05	2,52	0,71	2,67	2,45	0,70	2,67	2900	0,6	0,6
Gran_2	Mafic Granulite	4685165,72	517362,96	2,55	0,88	3,48	2,48	0,87	3,48	2900	0,8	0,7
Gran_3	Mafic Granulite	4685178,89	517362,73	4,32	0,71	7,48	4,20	0,71	7,46	2900	1,2	1,2
SL35[e]	Mafic granulite			1,50	0,74	10,79	1,46	0,73	10,76	2900	1,2	1,1
Ost-D[f]	Mafic granulite			2,75	0,00	0,00	2,67	0,00	0,00	2900	0,3	0,3
SL18[e]	Mafic Granulite			1,31	0,84	12,01	1,27	0,84	11,98	2900	1,3	1,2
AMP-450[h]	Mafic granulite			0,57	0,74	0,51	0,56	0,73	0,51	2900	0,3	0,3
AMP-463[h]	Mafic granulite			0,18	0,21	0,00	0,18	0,21	0,00	2900	0,1	0,1

AMP-448[h]	Mafic granulite	1,11	0,42	1,02	1,08	0,42	1,01	2900	0,3	0,3
AMPG-472[h]	Mafic granulite	0,28	0,00	2,54	0,27	0,00	2,54	2900	0,2	0,2
AMP-443[h]	Mafic granulite	0,51	0,21	0,61	0,50	0,21	0,61	2900	0,2	0,2
AMP-466[h]	Mafic granulite	0,34	0,42	0,00	0,33	0,42	0,00	2900	0,2	0,1
AMPG-475[h]	Mafic granulite	0,75	0,53	1,53	0,73	0,52	1,52	2900	0,3	0,3
AMPG-481[h]	Mafic granulite	0,21	0,63	1,63	0,20	0,63	1,62	2900	0,3	0,3
U-10[l]	Mafic Granulite	0,72	0,00	2,03	0,70	0,00	2,03	2900	0,2	0,2
U-90[l]	Mafic Granulite	4,07	0,00	6,10	3,96	0,00	6,09	2900	0,9	0,9
U-91[l]	Mafic Granulite	4,54	0,00	0,00	4,42	0,00	0,00	2900	0,5	0,4
U-42[l]	Mafic Granulite	3,88	0,00	19,33	3,78	0,00	19,28	2900	1,8	1,8

REFERENCES

ANSI no. 42, 14 (1999) - *American National Standard for calibration and use of Germanium spectrometers for the measurements of gamma-ray emission rates of radionuclides*.

BALDONCINI M. (2010) – *Applicazione del metodo Non Negative Least Square alla Full Spectrum Analysis nel processo di calibrazione di uno spettrometro di raggi gamma portatile.* Graduate thesis, University of Ferrara.

BANKA D., PHARAOH T.C., WILLIAMSON J.P. & TESZ PROJECT POTENTIAL FIELD CORE GROUP (2002) - *Potential field imaging of Palaezoic orogenic structure in northern and central Europe.* Tectonophysics, **360**, p. 23–45.

BARBEY P., GASQUET D., PIN C. & BOURGEIX A.L. (2008) – *Igneous banding, schlieren and mafic enclaves in calc-alkaline granites: The Budduso pluton (Sardinia).* Lithos, **104**, p. 147-163.

BEA F. (1999) – *Uranium.* In Encyclopedia of Geochemistry, Marshall, C.P. and Fairbridge, R.W. (editors), Kluwer Academic Publishers, London, 712 p.

BECKER H. (1997) - *Sm-Nd garnet ages and cooling history of high-temperature garnet peridotite massifs and high-pressure granulites from lower Austria*. Contributions to Mineralogy and Petrology, **127**, p. 224–236.

BELLOT J.P. & ROIG J.Y. (2007) - *Episodic exhumation of HP rocks inferred from structural data and P-T paths from the southwestern Massif Central (Variscan belt, France)*. Journal of Structural Geology, **29**, p. 1538–1557.

BOUTSIDIS C. & DRINEAS P. (2009) – *Random projections for the nonnegative least-square problem.* Linear Algebra and its Application, **431**, p. 760-771.

BRAGA R., GIACOMINI F., MESSIGA B. & TRIBUZIO R. (2001) - *The Sondalo Gabbroic Complex (Central Alps, Northern Italy): Evidence for Emplacement of Mantle-Derived Melts into Amphibolite-Facies Metapelites*. Physics and Chemistry of the Earth, **26**, no. 4-5, p. 333–342.

BRAGA R. & MASSONNE H.J. (2008) - *Mineralogy of inclusions in zircon from high-pressure crustal rocks from the Ulten Zone, Italian Alps*. Periodico di Mineralogia, **77**, no. 3, p. 43–64.

BRUNETON P. & ORSINI J.-B. (1977) – *Le massif granitique de Buddusò: une seule intrusion de type zoné concentrique*. Comptes Rendus de l'Académie des Sciences Paris, **284**, p. 151-154.

BURG J.-P. & GERYA T.V. (2005) – *The role of viscous heating in Barrovian metamorphism of collisional orogens: thermomechanical models and application to the Lepontine Dome in the Central Alps.* Journal of Metamorphic Geology, **23**, p. 75-95.

CACIOLLI A., BALDONCINI M., BEZZON G.P., BROGGINI C., BUSO G.P., CALLEGARI I., COLONNA T., FIORENTINI G., GUASTALDI E., MANTOVANI F., MASSA G., MENEGAZZO R., MOU L., ROSSI ALVAREZ C., SHYTI M., XHIXHA G. & ZANON A. – *A new FSA approach for in situ γ-ray spectroscopy*. Science of Total Environment, In press.

CAPPELLI B., CARMIGNANI L., CASTORINA F., DI PISA A., OGGIANO G. & PETRINI R. (1992) – *A variscan suture zone in Sardinia: geological, geochemical evidence, Paleozoic Orogenies in Europe (special issue)*. Geodinamica Acta, **5 (1-2)**, p. 101-118.

CARMIGNANI L., BARCA S., OGGIANO G., PERTUSATI P.C. & SALVADORI I. (2001) – *Memorie descrittive della carta geologica d'Italia.* Istituto Poligrafico della Stato, volume LX.

CARMIGNANI L., CAROSI R., DI PISA A., GATTIGLIO M., MUSUMECI G., OGGIANO G. & PERTUSATI P.C. (1994) – *The Hercynian chain in Sardinia (Italy).* Geodinamica Acta, **7**, p. 31-47.

CARMIGNANI L. & OGGIANO G. (1997) – *The variscan basement and the post-collisional evolution. Late Palaezoic continental basins of Sardinia.* The continental Permian International Congress, 15-18 Sept. 1999. Field trip guide-volume, p. 6-13.

CAROSI R. & PALMERI R. (2002) – *Orogen-parallel tectonic transport in the Variscan belt of northeastern Sardinia (Italy): implications for the exhumation of medium-pressure metamorphic rocks.* Geological Magazine, **139 (5)**, p. 497-511.

CASAS-SAINZ A.M. & DE VICENTE G. (2009) – *On the tectonic origin of Iberian topography.* Tectonophysics, **474**, p. 214-235.

CASINI L. (2011) – *A MATLAB-derived software (geothermMOD 1.2) for one-dimensional thermal modeling, and its application to the Corsica-Sardinia batolith.* Computer & Geosciences, in press.

CASINI L., FUNEDDA A. & OGGIANO G. (2010) - *A balanced foreland-hinterland deformation model for the Southern Variscan belt of Sardinia, Italy*. Geological Journal, **45**, p. 634–649.

CHOPIN G.R. (1988) – *Humics and radionuclide migration.* Radiochimica Acta, **44/45**, p. 23-28.

COCHERIE A., ROSSI PH., FANNING, C.**,** GUERROT C. (2005) - *Comparative use of TIMS and SHRIMP for U-Pb zircon dating of A-type granites and mafic tholeiitic layered complexes and dykes from the Corsican Batholith (France)*. Lithos, **82**, p. 185-219

COCHERIE A., ROSSI PH., FOUILLAC A.M. & VIDAL PH. (1994) - *Crust and mantle contributions to granite genesis – An example from the Variscan batholith of Corsica, France, studied by trace-element and Nd-Sr-O-isotope systematic*. Chemical Geology, **115**, p. 173-211.

CONTI L. (1966) *– Studio geopetrografico dell'Arcipelago della Maddalena. Nota II: L'Isola di Caprera.* Periodico di Mineralogia, **35**, p. 603-730.

COOKE R.A., O'BRIEN P.J. & CARSWELL D.A. (2000) - *Garnet zoning and the identification of equilibrium mineral compositions in high-pressure-temperature granulites from the Moldanubian Zone, Austria*. Journal of Metamorphic Geology, **18**, p. 551–569.

COOPER J.R., RANDLE K. & SOKHI R.S. (2003) *– Radioactive Releases in the Environment: Impact and Assessment.* John Wiley & Sons. 473 p.

CORTESOGNO L., DALLAGIOVANNA G., GAGGERO L., SENO S. & VANOSSI M. (1995) - *Nuovi dati sul basamento e sul tegumento carbonifero dell'Unità di Mallare (Brianzonese intermedio-interno, Alpi Liguri)*. Atti Ticinesi di Scienze della Terra, **3**, p. 65-82.

CORTESOGNO L., GAGGERO L., OGGIANO G. & PAQUETTE J.L. (2004) - *Different tectono-thermal evolutionary paths in eclogitic rocks from the axial zone of the Variscan chain in Sardinia (Italy) compared with the Ligurian Alps*. Ofioliti, **29**, p. 125-144.

COSTA S., MALUSKI H. & LARDEAUX J.M. (1993) - *^{40}Ar-^{39}Ar chronology of Variscan tectono-metamorphic events in an exhumed crustal nappe: the Monts du Lyonnais complex (Massif Central, France)*. Chemical Geology, **105**, p. 339–359.

CRUCIANI G., FRANCESCHELLI M., JUNG S., PUXEDDU M. & UTZERI D. (2008) - *Amphibolite-bearing migmatites from the Variscan Belt of NE Sardinia, Italy: Partial melting of mid-Ordovician igneous sources*. Lithos, **105**, p. 208–224.

CUCCURU S. (2009) – *Studio geologico-strutturale dei granitoidi varisici come lapidei ornamentali: problematiche inerenti la caratterizzazione, la coltivazione dei giacimenti e nuovi utilizzi in campo industriale.* University of Sassari. Unpublished PhD Thesis.

DAVIES J.H. & VON BLANCKENBURG F. (1995) - *Slab breakoff: A model of lithosphere detachment and its test in the magmatism and deformation of collisional orogens*. Earth and Planetary Science Letters, **129**, p. 85–102.

DEL MORO A., DI SIMPLICIO P., GHEZZO C., GUASPARRI G. & SABATINI G. (1975) – *Radiometric data and intrusive sequenze in the Sardinian batholith.* Neues Jahrbuch für Mineralogie – Abhandlungen, **126 (1)**, p. 28-44.

DEPINE, G.V., ANDRONICOS, C.L. & PHIPPS-MORGAN J. (2008) - *Near-isothermal conditions in the middle and lower crust induced by melt migration*. Nature, **452,** p. 80–83, doi:10.1038/nature06689.

DÉSESQUELLES P., HA T.M.H., KORICHI A., LE BLANC F. & PETRACHE C.M. – *NNLC: non-negative least chi-square minimization and application to HPGe detectors.* Journal of Physics G: Nuclear and Particle Physics, **36**, 037001, doi: 10.1088/0954-3899/36/3/037001.

DICKSON B.L. & SCOTT K.M. (1997) – *Interpretation of aerial gamma ray surveys-adding the geochemical factors.* AGSO Journal of Australian Geology & Geophysics, **17**, no. 2, p. 187-200.

DI PISA A., GATTIGLIO M. & OGGIANO G. (1992) – *Pre-Hercynian magmatic activity in the Nappe Zone (internal and external) of Sardinia: evidence of two Within Plate basaltic cycles.* In: Contribution to the Geology of Italy with special regard to the Paleozoic basement. A volume dedicated to Tommaso Cocozza. IGCP Project No. 276, Newsletter, **5**, p. 33-44.

DUGUET M., LE BRETON N. & FAURE M. (2007) - *P-T paths reconstruction of a collisional event: The example of the Thiviers-Payzac Unit in the Variscan French Massif Central.* Lithos, **98**, p. 210–232.

ELTER F.M., MUSUMECI G. & PERTUSATI P.C. (1990) – *Late Hercynian shear zone in Sardinia.* Tectonophysics, **176**, p. 387-404.

FAURE M., COCHERIE A., BÉ MÉZÈME E., CHARLES N. & ROSSI, P. (2010) - *Middle Carboniferous crustal melting in the Variscan belt: New insights from U-Th-$Pb_{tot.}$ monazite and U-Pb zircon ages of the Montagne Noire Axial Zone (southern French Massif Central).* Gondwana Research, **18**, p. 653–673.

FERNÁNDEZ-SUÁREZ J., ARENAS R., JEFFRIES T.E., WHITEHOUSE M.J. & VILLASECA C. (2006) - *A U-Pb Study of Zircons from a Lower Crustal Granulite Xenolith of the Spanish Central System: A Record of Iberian Lithospheric Evolution from the Neoproterozoic to the Triassic.* The Journal of Geology, **114**, p. 471–483.

FERRANDINI M., GINSBURG L., FERRANDINI J., ROSSI PH. (2000) – *Présence de Pomelomeryx boulangerii (Artiodactyla, Mammalia) dans l'Oligocène supérieur de la région d'Ajaccio (Corse): étude paléontologique et conséquences.* Comptes Rendus de l'Academie des Sciences Serie IIA Earth and Planetary Sciences, **331**, no. 10, p. 675-681.

FERRÉ E.C. & LEAKE B.E. (2001) – *Geodynamic significance of early orogenic high-K crustal and mantle melts: example of the Corsica Batholith.* Lithos, **59**, p. 47-67.

FINETTI I.R. (2005) - *Deep Seismic Exploration of the Central Mediterranean and Italy, CROP Project*. Elsevier, Amsterdam, 794 p.

FINGER F., GERDES A., JANOUŠEK V., RENÉ M. & RIEGLER G. (2007) - *Resolving the Variscan evolution of the Moldanubian sector of the Bohemian Massif: the significance of the Bavarian and the Moravo-Moldanubian tectonometamorphic phases*. Journal of Geosciences, **52**, p. 9–28.

FRANCESCHELLI M., PUXEDDU M., CRUCIANI G., DINI A. & LOI M. (2005) - *Layered amphibolite sequence in NE Sardinia, Italy: remnant of a pre-Variscan mafic silicic layered intrusion?*. Contributions to Mineralogy and Petrology, **149**, p. 164-180.

GALÁN G. & MARCOS A. (1997) - *Geochemical evolution of high-pressure mafic granulites from the Bacariza formation (Cabo Ortegal complex, NW Spain): an example of a heterogeneous lower crust*. Geologische Rundschau, **86**, p. 539-555.

GALLI A., LE BAYON B., SCHMIDT M.W., BURG J.P., CADDICK M.J. & REUSSER E. (2011) - *Granulites and charnockites of the Gruf complex: Evidence for Permian ultra-high temperature metamorphism in the Central Alps*: Lithos, **124**, p. 17–45.

GATTACCECA J., EISENLOHR P. & ROCHETTE P. (2004) – *Calibration of in situ magnetic susceptibility measurements.* Geophysical Journal International, **158**, p. 42-49.

GÉBELIN A., ROGER F. & BRUNEL M. (2009) - *Syntectonic crustal melting and high-grade metamorphism in a transpressional regime, Variscan Massif Central, France*. Tectonophysics, **477**, p. 229–243.

GHEZZO C. & ORSINI J.-B. (1982) – *Lineamenti strutturali e composizionali del batolite ercinico sardo corso in Sardegna. In "Guida alla geologia del Paleozoico Sardo".* Società Geologica Italiana (Roma), p. 88-102.

GIACOMINI F., BOMPAROLA R.M. & GHEZZO C. (2005) - *Petrology and geochronology of metabasites with eclogite facies relics from NE Sardinia: constraints for the Palaeozoic evolution of Southern Europe*. Lithos, **82**, p. 221–248.

GIACOMINI F., DALLAI L., CARMINATI E., TIEPOLO M. & GHEZZO C. (2008) - *Exhumation of a Variscan orogenic complex: insights into the composite granulitic-amphibolitic metamorphic basement of south-east Corsica (France)*. Journal of Metamorphic Geology, **26**, p. 403–436.

GÓMEZ-PUGNAIRE M.T., AZOR A., FERNÁNDEZ-SOLER J.M. & LÓPEZ SÁNCHEZ-VIZCAÍNO V. (2003) - *The amphibolites from the Ossa-Morena/Central Iberian Variscan suture (Southwestern Iberian Massif): geochemistry and tectonic interpretation.* Lithos, **68**, p. 23-42.

GUILLOT S. & MÉNOT R.P. (1999) - *Nappe stacking and first evidence of Late Variscan extension in the Belledonne Massif (External Crystalline Massifs, French Alps)*. Geodinamica Acta, **12**, p. 97–111.

GUY A., EDEL J.B., SCHULMANN K., TOMEK Č. & LEXA O. (2011) - *A geophysical model of the Variscan orogenic root (Bohemian Massif): Implications for modern collisional orogens*. Lithos, **124**, p. 144–157.

HARRIS R.N., VON HERZEN R.P., MCNUTT M.K., GARVEN G. & JORDAHL K. (2000) - *Submarine hydrogeology of the Hawaiian archipelagic apron, Part 1, Heat flow patterns north of Oahu and Maro reef.* Journal of Geophysical Research, **105**, no. B9, p. 21,353–21,369.

HEATH R.L. (1964) – *Scintillation spectrometry.* Gamma ray spectrum catalogue, 2nd Edition, Volumes 1 and 2: U.S.A.E.C. Research and Development Report IDO-16880-1, Physics T.I.D. – 4500 (31st edition).

INTERNATIONAL ATOMIC ENERGY AGENCY (1989). *Construction and Use of Calibration Facilities for Radiometric Field Equipment, Technical Reports Series No. 309*, IAEA, Vienna.

INTERNATIONAL ATOMIC ENERGY AGENCY (2003) - IAEA-TECDOC-1363: *Guidelines for radioelement mapping using gamma ray spectrometry data*, Vienna.

JANOUŠEK V., FINGER F., ROBERTS M., FRÝDA J., PIN C. & DOLEJŠ D. (2004) - *Deciphering the petrogenesis of deeply buried granites: whole-rock geochemical constraints on the origin of largely undepleted felsic granulites from the Moldanubian Zone of the Bohemian Massif.* Transactions of the Royal Society of Edinburgh: Earth Science, **95**, p. 141-159.

JANOUŠEK V. & HOLUB F.V. (2007) - *The causal link between HP-HT metamorphism and ultrapotassic magmatism in collisional orogens: case study from the Moldanubian Zone of the Bohemian Massif.* Proceedings of the Geologists' Association, **118**, p. 75–86.

JANOUŠEK V., KRENN E., FINGER F., MÍKOVÁ J. & FRÝDA J. (2007) - *Hyperpotassic granulites from the Blanský les Massif (Moldanubian Zone, Bohemian Massif) revisited*. Journal of Geosciences, **52**, p. 73-112.

JAUPART C. & MARESCHAL J.-C. (2004) - *Constraints on Crustal Heat Production from Heat Flow Data*. Treatise on Geochemistry, Vol. 3: The Crust. Edited by R.L. Rudnick. Elsevier Science Publishers. Amsterdam, p. 65-84.

JAUPART C. & MARESCHAL J.C. (2007) - *Heat Flow and Thermal Structure of the Lithosphere*. Treatise on Geophysics, **6**, p. 217–251.

KETCHAM R.A. (1996) - *Distribution of heat-producing elements in the upper and middle crust of southern and western Arizona: evidence from the core complexes*. Journal of Geophysical Research, **101**, p. 13611–13632.

KIRKEGAARD P. & LOVBORG L. (1974) – *Computer modelling of terrestrial gamma-radiation fields.* Riso Report No. 303.

KLEIN T., KIEHM S., SIEBEL W., SHANG C.K., ROHRMÜLLER J., DÖRR W. & ZULAUF G. (2008) - *Age and emplacement of late-Variscan granites of the western Bohemian Massif with main focus on the Hauzenberg granitoids (European Variscides, Germany)*. Lithos, **102**, p. 478–507.

KOTKOVÁ J., KRÖNER A., TODT W. & FIALA J. (1995) - *Zircon dating of North Bohemian granulites, Czech Republic: further evidence for the Lower Carboniferous high-pressure event in the Bohemian Massif.* Geologische Rundschau, **85**, p. 154–161.

KRUHL J.H. & VERNON R.S. (2005) – *Syndeformational emplacement of a tonalitic sheet complex in a late-Variscan thrust regime: fabrics and mechanism of intrusion, Monte Senes, northeastern Sardinia.* The Canadian Mineralogist, **43**, p. 387-407.

LANGMUIR D. & HERMANS J.S. (1980) – *The mobility of thorium in natural waters at low temperatures.* Geochimica et Cosmochimica Acta, **44**, 1753-1766.

LANGONE A., GODARD G., PROSSER G., CAGGIANELLI A., ROTTURA A. & TIEPOLO M. (2010) - *P-T-t path of the Hercynian low-pressure rocks from the Mandatoriccio complex (Sila Massif, Calabria, Italy): new insights for crustal evolution*. Journal of Metamorphic Geology, **28**, p. 137–162.

LAWSON C.L. & HANSON R.J. (1995) – *Solving Least Square Problems.* Philadelphia.

LEDRU P., COURRIOUX G., DALLAIN C., LARDEAUX J.M., MONTEL J.M., VANDERHAEGHE O. & VITEL G. (2001) - *The Velay dome (French Massif Central): melt generation and granite emplacement during orogenic evolution*: Tectonophysics, **342**, p. 207–237.

LEXA O., SCHULMANN K., JANOUŠEK V., ŠTÍPSKÁ P., GUY A. & RACEK M. (2011) - *Heat sources and trigger mechanisms of exhumation of HP granulites in Variscan orogenic root*. Journal of Metamorphic Geology, **29**, p. 79–102.

MACERA P., DI PISA A. & GASPERINI D. (2011) – *Geochemical and Sr-Nd isotopes disequilibria during multi-stage anatexis in a metasedimentary Hercynian crust.* European Journal of Mineralogy, **23**, no. 2, p. 207-222.

MALINVERNO A. & RYAN W.B.F. (1986) – *Extension in the Tyrrhenian Sea and shortening in the Apennines as a result of arc migration driven by sinking of the lithosphere.* Tectonics, **5**, p. 227-245.

MARTÍNEZ CATALÁN J.R. (2011) - *Are the oroclines of the Variscan belt related to late Variscan strike-slip tectonics?*. Terra Nova, **23**, p. 241–247.

MATTE P. (1986) – *La chaîne varisque parmi les chaînes paléozoïque péri atlantiques, modèle d'évolution et position des grands blocs continentaux au Permo-Carbonifère.* Bullettin de la Societe Geologique de France, **8**, p. 9-24.

MEDARIS L.G., BEARD B.L., JOHNSON C.M., VALLEY J.W., SPICUZZA M.J., JELÍNEK E. & MÍSĂR Z. (1995) - *Garnet pyroxenite and eclogite in the Bohemian Massif: geochemical evidence for Variscan recycling of subducted lithosphere*. Geologische Rundschau, **84**, p. 489–505.

MITTLEFEHLDT D.W. (1999) – *Potassium.* In Encyclopedia of Geochemistry, Marshall, C.P. and Fairbridge, R.W. (editors), Kluwer Academic Publishers, London, 712 p.

NAVIDAD M., CASTIÑEIRAS P., CASAS M. J., LIESA M., FERNÁNDEZ SUÁREZ J., BARNOLAS A., CARRERAS J. & GIL-PEÑA I. (2010) – *Geochemical characterization and isotopic age of Caradocian magmatism in the northeastern Iberian Peninsula: Insights into the Late Ordovician evolution of the northern Gondwana margin.* Gondwana Research, **17**, p. 325-337.

OGGIANO G., CASINI L., ROSSI PH. & MAMELI P. (2007) – *Long lived dextral strike-slip tectonics in the southern Variscan Belt: evidence from two syn-kynematic intrusions in north Sardinia.* Geologie de la France (Meeting on Mechanics of Variscan Orogeny: a modern view on orogenic research, Orleans 13-15 September 2007), **2**, p. 141.

OGGIANO G., CHERCHI G.P., AVERSANO A., DI PISA A., ULZEGA A., ORRÙ P. & PINTUS C. (2005) – *Note illustrative della Carta Geologica d'Italia, Foglio 428 Arzachena.*

OGGIANO G., FUNEDDA A., CARMIGNANI L. & PASCI S. (2009) – *The Sardinia Corsica microplate and its role in the Northern Apennine Geodynamics: new insights from the Tertiary intraplate strike-slip tectonics of Sardinia*. Italian Journal of Geosciences, **128 (2)**, p. 1-13.

OREJANA D., VILLASECA C., ARMSTRONG R.A. & JEFFRIES T.E (2011) - *Geochronology and trace element chemistry of zircon and garnet from granulite xenoliths: Constraints on the tectonothermal evolution of the lower crust under central Spain*: Lithos, **124**, p. 103–116.

ORSINI J.-B. & FERNANDEZ A. (1987) - *Signification de la discordance structurale entre fluidalité magmatique et zonalité pétrographique dans les intrusions de granitoïdes: l'exemple de l'intrusion de Budduso*. Comptes Rendus de l'Académie des Sciences Paris, **304**, p. 993–996.

PALOMERAS I., CARBONELL R., AYARZA P., FERNÀNDEZ M., SIMANCAS J.F., MARTÍNEZ POYATOS D., GONZÁLEZ LODEIRO F. & PÉREZ-ESTAÚN A. (2011) - *Geophysical model of the lithosphere across the Variscan Belt of SW-Iberia: Multidisciplinary assessment.* Tectonophysics, **508**, p. 42–51.

PAQUETTE J.-L., MÉNOT R.-P., PIN C. & ORSINI J.-B. (2003) – *Episodic and short-lived granitic pulses in a post-collisional setting: evidence from precise U-Pb zircon dating through a crustal cross-section in Corsica.* Chemical Geology, **198**, p. 1-20.

PARIS F. & ROBARDET M. (1990) – *Early Paleozoic paleobiogeography of the Variscan regions.* Tectonophysics, **177**, p. 193-213.

PEREIRA M.F., APRAIZ A., CHICHORRO M., SILVA J.B. & ARMSTRONG R.A. (2010) - *Exhumation of high-pressure rocks in northern Gondwana during the Early Carboniferous (Coimbra-Cordoba shear zone, SW Iberian Massif): Tectonothermal analysis and U-Th-Pb SHRIMP in-situ zircon geochronology*: Gondwana Research, **17**, p. 440–460.

PERROUD H. & BONHOMMET N. (1981) – *Paleomagnetism of the Ibero-Armorican arc and the Hercynian orogeny in western Europe.* Nature, **292**, p. 445-448.

PIN C., FONSECA P.E., PAQUETTE J.L., CASTRO P. & MATTE P. (2008) - *The ca. 350 Ma Beja Igneous Complex: A record of transcurrent slab break-off in the Southern Iberia Variscan belt?*: Tectonophysics, **461**, p. 356–377.

PIN C. & VIELZEUF, D. (1983) - *Granulites and related rocks in median Europe: a dualistic interpretation*. Tectonophysics, **93**, p. 47–74.

POCHAT S. & VAN DEN DRIESSCHE J. (2011) - *Filling sequence in Late Paleozoic continental basins: A chimera of climate change? A new light shed given by the Graissessac-Lodève basin.* Palaeogeography, Palaeoclimatology, Palaeoecology, **302,** p. 170–186.

POLYAK B.G., FERNÀNDEZ M., KHUTORSKOY M.D., SOTO J.I., BASOV I.A., COMAS M.C., KHAIN V.YE., ALONSO B., AGAPOVA G.V., MAZUROVA I.S., NEGREDO A., TOCHITSKY V.O., DE LA LINDE J., BOGDANOV N.A. & BANDA E. (1996) - *Heat flow in the Alboran Sea, western Mediterranean*. Tectonophysics, **263**, p. 191–218.

RECHE J., MARTINEZ F.J, ARBOLEYA M.L., DIETSCH C. & BRIGGS W.D. (1998) - *Evolution of a kyanite-bearing belt within a HT-LP orogen: the case of NW Variscan Iberia*. Journal of Metamorphic Geology, **16**, p. 379–394.

RICCI C.A. & SABATINI G. (1978) – *Petrogenetic affinity and geodynamic significance of metabasic rocks from Sardinia, Corsica and Provence.* Neues Jahrbuch für Geologie und Paläontologie, Abhandlungen, **1978**, p. 23-38.

ROSSI PH. & COCHERIE A. (1991) – *Genesis of a Variscan batholith. Field, petrological and mineralogical evidence from the Corsica-Sardinia batholiths.* In: Freeman R., Huch M., Mueller St (Eds) The European Geotraverse part 7. Tectonophysics, **195**, p. 319-346.

RUBATTO D., FERRANDO S, COMPAGNONI R. & LOMBARDO B. (2010) - *Carboniferous high-pressure metamorphism of Ordovician protoliths in the Argentera Massif (Italy), Southern European Variscan belt*: Lithos, **116**, p. 65–76.

RUSSELL J.K., DIPPLE G.M. & KOPYLOVA M.G. (2001) - *Heat production and heat flow in the mantle lithosphere, Slave craton, Canada*. Physics of the Earth and Planetary Interiors, **123,** p. 27–44.

SCHULMANN K., LEXA O., ŠTÍPSKÁ P., RACEK M., TAJČMANOVÁ L., KONOPÁSEK J., EDEL J.B., PESCHLER A. & LEHMANN J. (2008) - *Vertical extrusion and horizontal channel flow of orogenic lower crust: key exhumation mechanisms in large hot orogens?*. Journal of Metamorphic Geology, **26**, p. 273–297.

SCOTT K.M. & DICKSON B.L. (1990) – *Radioelements in weathered rocks and soils at the Wagga Tank polymetallic deposit Western NSW.* CSIRO Division of Exploration Geoscience Restricted Report **91R**.

SIEBEL W., RASCHKA H., IRBER W., KREUZER H., LENZ K.L., HÖHNDORF A. & WENDT I. (1997) - *Early Palaeozoic Acid Magmatism in the Saxothuringian Belt: New Insights from a Geochemical and Isotopic Study of Orthogneisses and Metavolcanic Rocks from the Fichtelgebirge, SE Germany*. Journal of Petrology, **38**, no. 2, p. 203-230.

SIMBOLI G. (1962) – *Studio petrografico dei graniti e di alcune loro differenziazioni nella zona di Buddusò (Sardegna).* Acta Geol. Alpina, **8**, p. 337-378.

SKRZYPEK E., ŠTÍPSKÁ P., SCHULMANN K., LEXA O. & LEXOVÁ M. (2011) - *Prograde and retrograde metamorphic fabrics – a key for understanding burial and exhumation in orogens (Bohemian Massif).* Journal of Metamorphic Geology, **29**, p. 451–472.

SLAGSTAD T. (2008) - *Radiogenic heat production of Archean to Permian geological provinces in Norway.* Norwegian Journal of Geology, **88**, p. 149-166.

ŠTÍPSKÁ P., SCHULMANN K. & KRÖNER A. (2004) - Vertical *extrusion and middle crustal spreading of omphacite granulite: a model of syn-convergent exhumation (Bohemian Massif, Czech Republic).* Journal of Metamorphic Geology, **22**, p. 179–198.

STOULOS S., MANOLOPOULOU M. & PAPASTEFANOU C. (2003) - *Assessment of natural radiation exposure and radon exhalation from building materials in Greece*. Journal of Environmental Radioactivity, **69**, p. 225-240.

RADIATION PROTECTION 112 (1999) – *Radiological Protection Principles concerning the Natural Radioactivity of Building Materials*. European Commission, Directorate-General Environment, Nuclear Safety and Civil Protection.

REGIONE AUTONOMA DELLA SARDEGNA (2007) – *Piano Regionale delle Attività Estrattive: riepilogo dei principali dati*. Cagliari, ottobre 2007, 176 p.

RUDNICK R.L. & FOUNTAIN D.M. (1995) - *Nature and composition of the continental crust: a lower crustal perspective*. Reviews in Geophysics, **33**, p. 267-309.

TAKENO N. (2005) – *Atlas of Eh-pH diagrams. Intercomparison of thermodynamic databases.* Geological Survey of Japan. Open File Report No. 419.

TAYLOR S.R. & MCLENNAN S.M. (1995) - *The geochemical evolution of the continental crust*. Reviews in Geophysics, **33***,* p. 241-265.

TSIRAMBIDES A. (1996) – *The greek marbles and other decorative stones.* University Studio Press, Thessaloniki, 310 p.

UNITED NATIONS SCIENTIFIC COMMITTEE ON THE EFFECTS OF ATOMIC RADIATION (1993) – *Sources and effects of ionizing radiation,* 922 p.

VAI G.B. & COCOZZA T. (1986) – *Tentative schematic zonation of the Hercynian chain in Italy*. Bullettin de la Societe Geologique de France, **8**, p. 95-114.

VAVRA G., SCHMID R. & GEBAUER D. (1999) - *Internal morphology, habit and U-Th-Pb microanalysis of amphibolite-to-granulite facies zircons: geochronology of the Ivrea Zone (Southern Alps)*. Contributions to Mineralogy and Petrology, **134**, p. 380–404.

VERDOYA M., PASQUALE V., CHIOZZI P. & KUKKONEN I.T. (1998) – *Radiogenic heat production in the Variscan crust: new determinations and distribution models in Corsica (northwestern Mediterranean)*. Tectonophysics, **291**, p. 63-75.

VIGLIOTTI L. & LANGENHEIM V.E. (1995) – *When did Sardinia stop rotating? New paleomagnetic results.* Terra Nova, **7**, p. 424-435.

VILÀ M., PIN C., LIESA M. & ENRIQUE P. (2007) - *LPHT metamorphism in a late orogenic transpressional setting, Albera Massif, NE Iberia: implications for the geodynamic evolution of the Variscan Pyrenees*. Journal of Metamorphic Geology, **25**, p. 321–347.

VILLASECA C., DOWNES H., PIN C. & BARBERO L. (1999) - *Nature and Composition of the Lower Continental Crust in Central Spain and the Granulite-Granite Linkage: Inferences from Granulitic Xenoliths*. Journal of Petrology, **40**, no. 10, p. 1465-1496.

VOSTEEN H.D., RATH V., CLAUSER C. & LAMMERER B. (2003) - *The thermal regime of the Eastern Alps from inversion analyses along the TRANSALP profile*. Physics and Chemistry of the Earth, **28**, p. 393-405.

WEDEPOHL K.H. (1991) - *Chemical-Composition and Fractionation of the Continental-Crust.* Geologische Rundschau, **80(2)**, p. 207-223.

WHITTINGTON A.G., HOFMEISTER A.M. & NABELEK P.I. (2009) - *Temperature-dependent thermal diffusivity of the Earth's crust and implications for magmatism*. Nature, **458**, p. 319-321, doi: 10.1038/nature07818.

ZORPI M.J., COULON C. & ORSINI J.-B. (1991) – *Hybridization between felsic and mafic magmas in calc-alkaline granitoids- a case study in northern Sardinia.* Chemical Geology, **92**, p. 45-86.